Dynamos exist. One can buy them in shops. What, one may ask, is all the fuss about?

P.H. Roberts and A. M. Soward in Annu. Rev. Fluid Mech. 1992. 24 : 459-512

# Planetary magnetic fields in the solar system: A numerical study of dynamo models

by

## Natalia Gómez Pérez

A thesis submitted to the Faculty of Graduate Studies and Research in partial fulfillment of the requirements for the degree of Doctor in Philosophy

**Department of Physics**

Edmonton, Alberta

Fall 2007

Library and
Archives Canada

Bibliothèque et
Archives Canada

Published Heritage
Branch

Direction du
Patrimoine de l'édition

395 Wellington Street
Ottawa ON K1A 0N4
Canada

395, rue Wellington
Ottawa ON K1A 0N4
Canada

NOTICE:
The author has granted a non-exclusive license allowing Library and Archives Canada to reproduce, publish, archive, preserve, conserve, communicate to the public by telecommunication or on the Internet, loan, distribute and sell theses worldwide, for commercial or non-commercial purposes, in microform, paper, electronic and/or any other formats.

AVIS:
L'auteur a accordé une licence non exclusive permettant à la Bibliothèque et Archives Canada de reproduire, publier, archiver, sauvegarder, conserver, transmettre au public par télécommunication ou par l'Internet, prêter, distribuer et vendre des thèses partout dans le monde, à des fins commerciales ou autres, sur support microforme, papier, électronique et/ou autres formats.

The author retains copyright ownership and moral rights in this thesis. Neither the thesis nor substantial extracts from it may be printed or otherwise reproduced without the author's permission.

L'auteur conserve la propriété du droit d'auteur et des droits moraux qui protège cette thèse. Ni la thèse ni des extraits substantiels de celle-ci ne doivent être imprimés ou autrement reproduits sans son autorisation.

---

In compliance with the Canadian Privacy Act some supporting forms may have been removed from this thesis.

Conformément à la loi canadienne sur la protection de la vie privée, quelques formulaires secondaires ont été enlevés de cette thèse.

While these forms may be included in the document page count, their removal does not represent any loss of content from the thesis.

Bien que ces formulaires aient inclus dans la pagination, il n'y aura aucun contenu manquant.

# Canada

# Abstract

In this dissertation numerical models of self-sustained convective dynamos are studied and developed, with application to solar system planetary dynamos. The three main works are: Chapter 2, model of different stages of terrestrial planet core growth; Chapter 3, model of magnetic fields of the ice giants; Chapters 4 and 5, development of the legacy dynamo code to include radially variable conductivity, and application of resulting models to the gas giants.

Aging terrestrial planets have growing inner cores. We show that core size can determine the character of dynamo generated magnetic fields. Even though they depend on initial conditions and scaling parameters, it is possible to use field geometries and magnitudes as diagnostic of internal planetary structure. The ratio between inner and outer core radii, $\chi$, yields strong magnetic fields for intermediate values ($0.25 < \chi < 0.45$), and weaker fields otherwise. High magnetic field intensity patches are found near latitudes $\pm\arccos(\chi)$ where the inner core tangent cylinder intersects the outer boundary. Boundary conditions and internal force balances are responsible for dominant harmonic components of external magnetic fields. The peculiar characteristics of ice giants' magnetic fields can be explained by internal force balances. Uranus and Neptune have deep electrolytic liquid interiors of ice-like composition, with electrical conductivity about two orders of magnitude lower than molten iron. Low electrical conductivity models yield numerical dynamos dominated by kinetic energies. We show the simulated flows are quasi-geostrophic and result in non-dipolar, highly transient, and non-axisymmetric magnetic fields, comparable to magnetic fields of the ice giants.

Modifications of the numerical code, better representing the gas giants' interiors, are introduced and tested. Radially variable electrical conductivity (expected for the gas giants) is implemented into numerical algorithms to solve the magnetohydrodynamic governing equations. We show that variable conductivity changes dynamo model flows and magnetic fields significantly. Redefinition of non-dimensional parameters: $Ra^*$, $E^*$, and $\chi^*$ is introduced, better characterizing the new models. Tests presented here yield largely axisymmetric and dipolar fields, applicable to characteristics of Jupiter and Saturn. Future work however, should use a wider range of non-dimensional parameters in order to find force balances expected for the gas giants.

*To*

*Marlen, Rigoberto y Marcela. Sin quienes este trayecto*

*hubiera sido imposible.*

# Acknowledgements

# Table of Contents

TABLE OF CONTENTS

TABLE OF CONTENTS

# List of Tables

# List of Figures

# Chapter 1

# Introduction

Humanity has studied the stars and planets for centuries. Many cultures have related the stars to myths and gods. For celestial bodies, length scales are not comparable with human every day life, but the effects of stellar and planetary internal dynamics affect us, from the reading of a compass to the magnetosphere shielding the Earth from high energy solar winds. The ancient Greeks recognized differences in motion between fixed stars and the wanderers, i.e. planets wandering through the sky amongst the stars. The planet Earth was known (or better re-discovered) to be spherical in the XV century. The second physical property attributed to the planet as a whole, early in the XVII century, was its intrinsic magnetic field (Gilbert (1600)).

This dissertation will focus on planetary magnetic fields and particularly on dynamo models. For strong planetary magnetic fields, the planet's internal dynamics are responsible for the magnetic field generation. It is interesting how planets with different composition and structure, e.g. Earth and Jupiter, have intrinsic magnetic fields from similar origins. We will present an overview of dynamo generated magnetic fields in planetary environments for terrestrial and giant planets. As a brief introduction to the celestial bodies studied in this dissertation, in section 1.1 we include a historical summary for some planets in the solar system, including a summary of current knowledge of their magnetic fields, and how these fields were discovered. Particular characteristics of planetary environments will be presented in detail in the introduction for each chapter referring to the various respective models. In section 1.2, a brief description of the dynamo model is presented. Finally, in section 1.3 we present a brief review of numerical models for the dynamo problem.

## 1.1 Solar system planets

### 1.1.1 Mercury

Named after the Roman god, Mercury is the closest planet to the sun, and also has the smallest radius. Its short orbital period likely led to its association with Hermes, the fast messenger for the gods to communicate with humans in Greek mythology. Even though the existence of

this planet was discovered early in history, detailed measurements of gravitational and magnetic fields were not possible until the arrival of the spacecraft Mariner 10 in the vicinity of the planet. In 1974 and 1975, Mariner 10 had three encounters with Mercury (Ness et al. (1976)). Using measurements from gravitational moments, the non-compressed density of the interior was found to be relatively high when compared with that of the moon and the Earth. With a mean radius of $0.38R_{earth}$, Mercury has an iron core that extends up to 70% of the planetary radius (Stevenson (1987)). There is evidence for a fluid core inside Mercury (Margot et al. (2007)). It is believed, as is true for the Earth, that Mercury has a solid inner core, but if so, its size is unknown. In the case of a pure iron fluid core composition, the inner core is expected to be large (due to rapid cooling). In contrast, for a fluid composed of a combination of iron with lighter elements (sulphur for example), the inner core growth rate diminishes notably, allowing for the possibility that Mercury could have a small inner core (Labrosse et al. (2001)).

The source of the magnetic field measured by Mariner 10 has been a subject of discussion in the literature. The relatively weak field does not seem to depend on the inter-planetary magnetic field, since both spacecraft approaches (when the Hermean field was measured) showed the similar magnetic field geometry, even though the solar conditions were significantly different. Thanks to these observations, the possibility of the field being induced by an external source--as is the case with Europa and Callisto, Khurana et al. (1998)--is not valid for Mercury, Ness et al. (1976).

Three possibilities remain for explaining the origin of the magnetic field in Mercury. First, dynamo action may exist inside the planet. The small size of Mercury yields a fast inner core cooling rate, and possibly, a relatively short time for the liquid core to solidify. The presence of light elements in the fluid becomes necessary to account for a molten core in Mercury to the present. The abundance of light elements in the fluid is difficult to estimate. Consequently, the size of the inner core is also unknown. If the field of Mercury is generated by dynamo action, the size of the inner core is crucial, since a solid core is not able to sustain a significant magnetic field. Second, the possibility of remanent magnetism of the Hermean crust has been argued. Aharonson et al. (2004) calculated the crustal remanent magnetization for a non-uniform thickness spherical shell, and showed that it is possible for a spherical shell with no internal magnetic field to be magnetized by an imposed external magnetic field. Runcorn's theorem states the impossibility of remanent magnetization in a spherical shell by an external field. This theorem is only valid for a homogeneous perfectly spherical shell. That is clearly not the case in Mercury's crust. Thus, the possibility of crustal remanent magnetization cannot ruled out as the reason for Mariner's 10 measurements. Last, a thermo-electric dynamo has also been proposed by Stevenson (1987). The magnetic field in this case would be generated in a thin layer of a mixture of sulphur and iron located at the top of the Hermean fluid core. The thermal dynamics of the flow, driven by the topography of the core-mantle interface, would generate an effective electromotive force producing a toroidal magnetic field. The poloidal component of the field would be generated by the convection of the flow though the $\alpha$ effect. The magnitude of the resultant field would be small, in agreement with spacecraft measurements, and the geometry would be quite different from a dynamo generated magnetic field: this dynamo would not have any symmetry preference for the axis of rotation (Stevenson (1987)).

## 1.1.2 Earth

The best known dynamo in the solar system is that of the earth. Direct observations of the Earth's magnetic field date back to the sixth century B.C. The development of the compass as a navigation tool drew attention to the magnetic pole wandering, as opposed to it being stationary with respect to the fixed stars. Gilbert (1600) proposed the existence of an internal magnet in the Earth that made the compass point north. The change in declination as a function of latitude became evident for people navigating the seas with the help of magnetic needles. The first geomagnetic chart of the globe was drawn in the XVIII century. Later, J. C. Friedrich Gauss presented the coefficients of the spherical harmonic expansion in his *Allgemenie Theorie des Erdmagnitismus* in 1838.

In the past century, paleomagnetism revolutionized what was known of Earth's dynamics. It helped to prove the plate tectonic theory and showed evidence of historical changes in the Earth's magnetic field over geological time scales. These changes in magnetic fields involved polarity reversals; a phenomenon in which the north-south magnetic poles change hemispheres in a relatively short period of time. Reversals seem to occur with no distinguishable frequency, but with a mean occurrence period of about 0.5 Ma, e.g. Merrill et al. (1998).

Seismic measurements reveal the presence of an iron core stratified into solid and liquid parts at the interior of the Earth (Dziewonski & Anderson (1981)). Combining seismological models of the interior with equations of state for silicates (mantle) and iron (core), temperature and pressure profiles may also be inferred. A detailed knowledge of the thermal profiles of mantle and core is important for dynamo studies because convection (thermal and compositional) is the driving force of the dynamo. Despite great uncertainties, we know that the crystallization of the inner core has supported the dynamo for approximately 1000Ma (Labrosse et al. (2001)). Estimates of the inner core age are rough since they depend sensitively on composition of the fluid core alloy, which is not well constrained.

Sir J. Larmor proposed in 1919 that magnetic fields in celestial bodies may be generated by an internal dynamo. To study the possibility of self-excited dynamos, T. G. Cowling analysed two-dimensional stationary electromagnetic fields. Cowling showed that stationary magnetic fields cannot be supported by axisymmetric flows. Fluid convection within planetary cores result in three-dimensional flows. Rapidly rotating systems help to constrain flows to almost two-dimensional planes perpendicular to the rotation axis, such geostrophic flows follow the Proudman-Taylor constraint. Nevertheless, a quasi-geostrophic flow allows weak motion in the direction of the axis of rotation, making the flow not completely planar.

Thus rapidly rotating spherical shells are able to sustain magnetic fields. A convenient mathematical decomposition of toroidal and poloidal contributions of the magnetic field was presented by E. Bullard and H. Gellman in 1954 (Gibson et al. (1967)). They studied kinematic dynamos (where the magnetic field may be calculated for a given flow; the imposed flow may or may not allow the magnetic field to be sustained). Elsasser (1956) examined extensively the hydromagnetic dynamo theory (or magnetohydrodynamic dynamos). He explained magnetic field amplification mechanisms such as the $\omega$-effect and the $\alpha$-effect. These mechanisms explain the amplification of

magnetic field by means of field line stretching due to the flow; generation of poloidal field lines from toroidal field lines and vice versa.

Only in the very recent past could this theory be confirmed numerically as a magnetic field generation source. The full set of equations describing dynamo models are not simple, and analytic solutions of self sustained dynamos have not been found. Numerical models solving the complete set of equations have been developed in the past 25 years and are evolving rapidly with the help of the rapid advancement in computational capabilities. For more information on dynamo models and its numerical solutions please refer to sections 1.2 and 1.3 in this chapter.

The physical properties of the Earth's interior are more or less constrained. Indirect methods give us information for expected values of the physical system parameters. As a reference, we include table 1.1 with physical parameters known or estimated for the Earth's interior.

Table 1.1: Physical parameters of the Earth's core. Estimated and known values for a liquid iron core. Some of the estimations included in this table have great uncertainties. We include symbols with the subscript $t$ at the bottom; they estimate the increased diffusivities due for a turbulent flow. Values in this table are taken from Jones (2007).

| | Value | Symbol |
|---|---|---|
| Radius of the outer core | $3.48 \times 10^6$m | $r_o$ |
| Radius of the inner core | $1.22 \times 10^6$m | $r_i$ |
| Temperature drop from the CMB to the ICB | $\sim 1.3 \times 10^3$K | $\Delta T$ |
| Outer core mean density | 11340kg/m$^3$ | $\rho$ |
| Gravity at $r_o$ | 7.8m/s$^2$ | $g_o$ |
| Angular velocity | $7.29 \times 10^{-5}$s$^{-1}$ | $|\Omega|$ |
| Thermal expansion coefficient | $1.5 \times 10^{-5}$K$^{-1}$ | $\alpha$ |
| Magnetic diffusivity | $\sim 2\,\text{m}^2/\text{s}$ | $\lambda$ |
| Thermal diffusivity | $\sim 5 \times 10^{-6}\text{m}^2/\text{s}$ | $\kappa$ |
| Kinematic viscosity | $\sim 5 \times 10^{-7}\text{m}^2/\text{s}$ | $\nu$ |
| Turbulent thermal diffusivity | $\sim 2\,\text{m}^2/\text{s}$ | $\kappa_t$ |
| Turbulent kinematic viscosity | $\sim 2\,\text{m}^2/\text{s}$ | $\nu_t$ |

### 1.1.3 Jupiter and Saturn

Also called the gas giants, Jupiter and Saturn are the largest planets in the solar system with radii of $11.2R_{earth}$ and $9.4R_{earth}$ respectively. Named after the god of lightening and thunder, Jupiter and his father Saturn are two of the most powerful deities in Roman mythology (along with their Greek counterparts, Zeus and Cronus). These wanderers were discovered very early in history along with Mercury, Venus, and Mars.

A magnetic field attributed to Jupiter was not found until the XX century with earth-based measurements of radio emissions, Barrow (1960). These observations were confirmed by direct magnetic field measurements by spacecraft missions visiting the gas giants. Pioneer 10 and 11 verified the presence of a magnetosphere around Jupiter; they found, at that time, a strong non-dipolar field component (Acuña & Ness (1975)). The influence of Io and Ganymede (causing

the non-dipolar geometry) on the Jovian magnetosphere was measured by Voyager I and II spacecrafts (Ness et al. (1979)).

The field of Saturn was discovered by Pioneer 11 and was also measured by the Voyager missions, Acuña & Ness (1980), Ness et al. (1981, 1982). Later, spectral decompositions of the radial magnetic fields were estimated using Pioneer's and Voyager's data, see Connerney et al. (1982, 1998). The magnetic field of Saturn has been found to be particularly dipolar and aligned with the rotation axis (i.e. axisymmetric). Current missions are examining Saturn and its moons. The Cassini-Huygens spacecraft reached Saturn in 2004. The European Space Agency's Huygens Probe acquired four hours of data from Titan's atmosphere and surface on its descent, Lebreton et al. (2005). The Cassini orbiter is expected to take data until at least 2008.

### 1.1.4 Uranus and Neptune

Uranus and Neptune are the outermost planets in the solar system. With radii of $4R_{earth}$ and $3.9R_{earth}$ for Uranus and Neptune, respectively, these planets are called the ice giants. They are the only classical planets discovered in modern history (1781 and 1846 for Uranus and Neptune, respectively). The name of Uranus came from the chronological series of the planets given by the Greeks: Mars son of Jupiter, son of Saturn, all descendants of Uranus (the sky). Neptune was discovered thanks to its gravitational effects on the motion of Uranus. The name chosen for this planet relates it to the god of the sea. The magnetic fields of Uranus and Neptune were not discovered until Voyager II reached them in 1986 and 1989, respectively (Ness et al. (1986, 1989)). Their magnetic fields have unusual geometries in which the dipolar components are relatively weak with respect to higher multipolar components. After the first encounter of Voyager with Uranus, scientists thought it was possible that this planet was encountered while undergoing a magnetic pole reversal. When Neptune was found to have similar characteristics, the idea was discarded. The probability of both ice giants experiencing pole reversals from stable dipolar Earth-like fields is low. Since both planets have high multipolar fields, there might be intrinsic characteristics of field generation leading to higher probabilities of a non-dipolar, and non-axisymmetric magnetic fields and/or a higher probabilities of polarity reversals.

Another surprising feature is the axis of rotation of Uranus. All other solar system planets have an axis of rotation almost perpendicular to the ecliptic. In contrast, Uranus' rotation axis is 97.9° with respect to its orbital axis. This may have been caused by a strong impact with an asteroid. Voyager also found an important difference in the energy emission of ice giants. Uranus' and Neptune's heat flows are lower than what would be predicted by homogeneous cooling. This may significantly affect the internal dynamics of the planets, see Stevenson (1982).

## 1.2 The dynamo model

The derivation of the equations describing the dynamo problem are included in this dissertation in appendix A. The system that these equations describe consists of an electrically conductive fluid, bounded by two spherical shells of internal and external radii $r_i$ and $r_o$, respectively (see

figure 1.1). We take the inner sphere to be electrically conductive and solid, as is appropriate
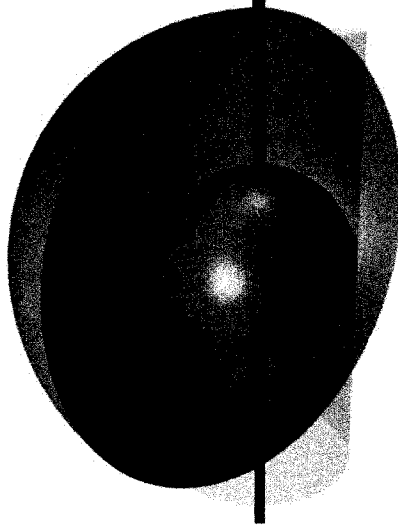


Figure 1.1: Geometry used for dynamo models. Inner core of radius $r = r_i$ in red, and outer core boundary, $r = r_o$, in purple. The tangent cylinder is marked here with a transparent green surface, and the rotation axis , $\hat{z}$, is marked with a black line.

for a terrestrial planet's interior with a solid inner core. The radius ratio is defined as $\chi = r_i/r_o$. The system rotates with an angular velocity $\Omega$, with the axis of rotation parallel to the unitary vector $\hat{z}$, marked with a black line in figure 1.1. For future reference, we define the *tangent cylinder* as an imaginary surface in the outer core. Its axis of symmetry is parallel the $z$-axis, and the cylinder is tangent to the inner core at the equatorial plane (green transparent surface in figure 1.1).

The non-dimensional equations are derived using scaled quantities. Temperature is scaled by the temperature difference between the inner and outer shells, $\Delta T$; distance by the shell gap width, $D = r_o - r_i$; time by the viscous diffusion time, $\tau_\nu = D^2 \nu^{-1}$, where $\nu$ is the kinematic viscosity; velocity by $\nu D^{-1}$; pressure by $\rho \nu \Omega$; and magnetic induction by $\sqrt{\rho\mu\lambda\Omega}$, where $\rho$ is the density, $\mu$ the magnetic permeability and $\lambda$ is the magnetic diffusivity of the fluid. The non-dimensional equations describing velocity, magnetic field induction and temperature fields, in the rotating frame of reference, and under the MHD and Boussinesq approximations (see appendix A) are:

$$E\left(\frac{\partial \mathbf{u}}{\partial t} + (\mathbf{u} \cdot \nabla)\mathbf{u} - \nabla^2 \mathbf{u}\right) + 2\hat{z} \times \mathbf{u}$$

$$= -\nabla P + \frac{R_a E}{P_r}\frac{g}{g_o}\hat{r}T + \frac{1}{P_m}(\nabla \times \mathbf{B}) \times \mathbf{B}, \qquad (1.1)$$

$$\nabla \cdot \mathbf{u} = 0, \qquad \nabla \cdot \mathbf{B} = 0, \qquad (1.2)$$

$$\frac{\partial T}{\partial t} + \mathbf{u} \cdot \nabla T = \frac{1}{P_r}\nabla^2 T, \qquad (1.3)$$

$$\frac{\partial \mathbf{B}}{\partial t} \;=\; \nabla \times (\mathbf{u} \times \mathbf{B}) + \frac{1}{P_m}\nabla^2 \mathbf{B}, \tag{1.4}$$

where $\mathbf{u}$ and $\mathbf{B}$ are the velocity and magnetic induction vectors, respectively; $t$ is the time; $T$ and $P$ are the temperature and pressure scalars, respectively; $g$ is the radially dependent gravity, and $g_o$ is the gravity at the outer boundary; and $\hat{\mathbf{r}}$ is the radial unit vector.

Equations 1.1 to 1.4 are expressed in terms of the following non-dimensional parameters: The Rayleigh number,

$$R_a = \frac{\alpha g_o \,\Delta T \, D^3}{\kappa \nu}, \tag{1.5}$$

where $\alpha$ is the thermal expansion coefficient and $\kappa$ is the thermal diffusivity. $R_a$ is associated with the thermal balance within the fluid. There is a critical value, $R_{a_c}$, for which if $R_a < R_{a_c}$ heat is exclusively transfer by conduction while if $R_a > R_{a_c}$ there is convection and conduction as heat transfer mechanisms. The Ekman number,

$$E = \frac{\nu}{\Omega D^2}, \tag{1.6}$$

which is the ratio between viscous and coriolis forces in the system. The Prandtl number,

$$P_r = \frac{\nu}{\kappa}, \tag{1.7}$$

which is the ratio between the viscous and the thermal diffusivites. And the magnetic Prandtl number,

$$P_m = \frac{\nu}{\lambda}, \tag{1.8}$$

which is the ration between the viscous and the magnetic diffusivities.

Using values from table 1.1, values of the non-dimensional numbers expected for the interior of the Earth are calculated and presented in table 1.2. It is useful also to introduce the *magnetic diffusion time* as $\tau_\lambda = D^2 \lambda^{-1}$. Using values in table 1.1, $\tau_\lambda \sim 100$ ka. Please note that $\tau_\lambda = P_m \tau_\nu$.

## 1.3   Three-dimensional self-sustained numerical dynamos

Stellar dynamos are based on the same set of equations presented in sections A.1, A.2, and A.3. Different approximations are suitable for different environments. The interior of a star, for example, has density that varies strongly with radius; the Boussinesq approximation may not be

Table 1.2: A rough estimate of non-dimensional numbers for the Earth's core. As in table 1.1, the subscript $t$ indicates estimations for turbulent flows.

| Non-dimensional number | Estimated value | Symbol |
|---|---|---|
| Rayleigh | $\sim 10^{30}$ | $R_a$ |
| Ekman | $\sim 5 \times 10^{-15}$ | $E$ |
| Prandtl | $\sim 0.1$ | $P_r$ |
| Magnetic Prandtl | $\sim 2.5 \times 10^{-7}$ | $P_m$ |
| Turbulent Ekman | $\sim 5 \times 10^{-9}$ | $E_t$ |

valid. Furthermore, stellar deep interiors are subjected to very high pressures and, in some cases, it is possible that the MHD approximation is not valid either (see discussion on Jupiter's interior in page 101). Kageyama et al. (1995) cite the first three-dimensional non-linear MHD numerical simulation as developed in the 1970's in a fusion plasma context. Gilman & Miller (1981) applied, for the first time, MHD numerical simulations to celestial bodies. They presented solar dynamo models using the Boussinesq approximation; they used very high viscosities ($E \sim 10^2$). With solar dynamo models, spherical three-dimensional self-sustained dynamo simulations were first attained. Divergence of the solution near the poles restricted the simulations to equatorial zones. Glatzmaier (1984, 1985a,b) later developed anelastic solar dynamo models (the anelastic approximations is explain in detail in appendix A). He applied to the dynamo equations the spectral decomposition by poloidal and toroidal potentials proposed in Chandrasekhar (1961). With this approach, the problem with divergent solutions near the poles was sufficiently addressed. The numerical implementation using the spectral algorithm yielded, for the first time, stable solutions over a whole sphere, except for the singularities at the poles.

For fully compressible fluids (i.e. neither Boussinesq or anelastic), Kageyama et al. (1993) solved non-magnetic convection models, but still using relatively high viscosity fluids ($E \sim 10^{-1}$). Later, they developed a finite-difference full MHD dynamo model. The goal of these simulations was a better understanding of the MHD dynamo solutions, rather than a direct application to the stars or planets, Kageyama et al. (1995).

Computational hardware advancements and the accurate spectral techniques allowed for geodynamo simulations continues to evolve rapidly. With the use of hyperdiffusivities (which are used for damping high harmonic order energy contribution) numerical solutions were found to reproduce characteristic features of the magnetic field of the Earth (e.g. Glatzmaier & Roberts (1995), Kuang & Bloxham (1997)). Even though the numerical solutions were stable thanks to the hyperdiffusivities, the physical effect of this artificial damping may be of concern when comparing numerical solutions to actual physical systems. Nevertheless, the promising results of these original numerical simulations, dipolar and non-periodically reversing self sustained dynamos (e.g. Glatzmaier et al. (1999)) encouraged various groups to use spectral methods to solve the dynamo problem numerically.

For example, Glatzmaier's models were the basis for Christensen et al. (1998) to continue the development of three-dimensional self-sustained numerical dynamos, as those included in this dissertation. This code, featuring the Boussinesq approximation, and using spectral methods,

has also been modified and improved further in the past ten years. Wicht (2002) added an electrically conductive inner core and studied the coupling between inner and outer cores. The numerical code we use throughout this study has, as a base, a modified version of Wicht's MagIC 2.0. We present here a further development of this code, and it is explain in detail in chapter 4.

The proliferation of numerical models for geodynamo simulations yielded the creation of a benchmark, presented in Christensen et al. (2001). That paper compared results from six different groups; all of them using spectral methods for the solution over spherical surfaces. They found that fully spectral methods (i.e. including a spectral radial solution) have higher numerical accuracy than those applying finite-difference methods for the radial component. More complicated solutions (with high energy for higher orders and degree components) may be more suitable for the finite-difference methods, where the parallelization of the code is more efficient.

The study of the geodynamo has not been restricted to spectral methods. For example, using a tri-lineal hexahedral grid, a finite element approach has been successfully used to model thermal convection between spherical shells, Matsui & Okuda (2002). They found that this approach requires a high density grid in the radial direction, in order for results to be comparable with those using spectral methods. As mentioned above, it is possible that spectral methods are more suitable for low $R_a$ and high $E$ models, due to the sharp decreases in energy spectra with increasing spherical degree, and that finite element or finite difference approaches become more suitable for runs with high spherical degree and order contributions. Self-sustained dynamo models have been developed as well using interesting grid configurations such as the "Yin-Yang grid" presented by Kageyama & Sato (2004). They divided the space into two identical grids that overlap over a small area of the space, but covering the whole spherical area. Their grids allow for a finite element code that avoids the numerical complications in regions close to the poles ($\theta = 0, \pi$) that Gilman & Miller (1981) found earlier. One of the great advantages of finite element or finite difference methods is not only the parallelization (and thus speed) of the code, but also that they are more suitable for including mechanically compressible fluids (which is not suitable for spectral methods). Some other interesting studies are, for example, those of Matsui & Buffett (2005). The influence of small scale eddies in large scale flow was studied using a sub-grid scale model. The effect of small scale turbulence on the overall macroscopic system has been argued to increase the kinematic viscosity. The extent to which small scale turbulence affects flows is important for large scale simulations, since it may have macroscopic effects in modifying physical properties of the fluid, i.e. turbulent kinematic viscosity versus fluid kinematic viscosity (see table 1.1).

In this dissertation we include models and results from numerical simulations to help understand the interior dynamics of planetary bodies. In chapter 2, we present a set of ninety five simulations with boundary conditions that make them comparable to terrestrial planets. We find the Rayleigh number for the onset of dynamo action and how it varies with radius ratio, $\chi$, and variations in the initial conditions. Chapter 3 presents a set of simulations with strong zonal flows. We find that our models, originally motivated by the ice giants' interiors, result in highly non-dipolar fields. The magnitude of the field generated by these models is relatively small, in agreement with spacecraft measurements from the ice giants. We then propose a possible mech-

anism for field generation in the ice giants. We also introduce modifications on the numerical model, featuring variable electrical conductivities. We present the new model and preliminary tests in chapter 4. We use our new implementation to study variable electrical conductivity models. In chapter 5 we present results of low $E$ and stress free velocity boundary condition simulations. We show how variations in the electrical conductivity profiles may affect thermal and magnetic fields. For the parameters studied, the velocity field is not changed significantly by the new implementation when compared to the homogeneous electrical conductivity runs. We find that, with the parameters tested for the variable conductivity runs, the system is dominated by the kinetic energy. Our runs yield dynamos that are axisymmetric and dipolar, but where high harmonic degree and order contributions to magnetic fields are significant. Finally, we propose to explore different thermal boundary conditions to find simulations with dominantly magnetic energies (which is what we expect for the gas giants based on the results presented in this dissertation). The variable electrical conductivity in planetary dynamos changes significantly the dynamics affecting resultant magnetic fields. It is important to include this approximation in modelling the gas giants.

# Chapter 2

# Onset of dynamo action in spherical shell geometry

## 2.1 Introduction

From the enigmatic Hermean magnetic field (Ness et al. (1976)) to the highly non-dipolar dynamo in Neptune (Connerney et al. (1991b)), the solar system presents a variety of dynamos to explore. Dynamos in terrestrial planets are believed to behave similarly to Earth's. Convective motion by the fluid iron core is the origin of the intrinsic planetary magnetic field. The convection is due to cooling and solidification of the inner core, and an efficient heat transfer though the mantle. The result is a temperature difference between the core-mantle boundary (CMB) and the inner-outer core boundary (ICB). This cooling causes the growth of the inner core due to crystallization. The crystallization of the inner core also causes a separation of light elements in the fluid core which, by buoyancy, rise to the CMB. This process is called compositional convection. The inner core will continue to grow until complete solidification occurs. Studying the dependence of dynamo action on the size of the inner core (or the shell thickness) will help our understanding of the evolution of terrestrial planets. In this chapter, we identify particular characteristics of the magnetic field generated by dynamo action for various shell thickness.

The history of the evolution of the Earth's core is not well determined. Its rate of growth is not well constrained and depends on the metallic core content of radioactive elements, see Labrosse et al. (2001). In addition, the thermal boundary conditions may vary from the present cooling mechanism (e.g. plate tectonics may cease), and this would change dramatically the underlying fluid core dynamics.

Moreover, one can imagine that other terrestrial planets are at different stages of inner core growth. Mars, for example, has no magnetic field from dynamo action, but has a strongly magnetized crust, see Acuña et al. (1998). It is reasonable to infer an extinct dynamo; the extinction likely due to either a change in the thermal dynamics of the planet (conduction rather than convection), or inner core size. In the former case, the core could have grown to the point

where the convective motion of the fluid core was too constrained to sustain dynamo action.

To catalogue a planetary magnetic field as internally generated by dynamo action, the planet should present a magnetosphere that is independent of the background field. Mercury has a magnetic field that may be strongly affected by the solar wind, but it has been found to be independent of the solar wind, see Ness et al. (1976), Grosser et al. (2004). The uncompressed density of the planet is high when compared to all other terrestrial planets. This is due to a large iron core that occupies about 70% of the total planetary radius. The growth an inner core in terrestrial planets depends sensitively on composition. Nucleation may be inhibited given the presence of light elements in the fluid core such as sulphur. One of the great unknowns in the case of Mercury is the presence and size of a solid inner core (Spohn et al. (2001)). This outstanding question may be solved by indirect methods. The size of the inner core restricts the flow which gives rise to a characteristic magnetic field. We will show that the magnetic field can be used as a diagnostic to determine the size of the inner core.

Numerical models have been used to understand chaotic systems such as the one described by the Navier-Stokes equations. The critical Rayleigh number, $R_{a_c}$, defines a critical value for which the heat flow is due exclusively to thermal conduction, for $R_a < R_{a_c}$, or a combination of thermal conduction and convection for $R_a > R_{a_c}$. In the case of rotating spherical shells, the critical Rayleigh number for convection depends on the geometry of the shell, and the physical properties of the fluid. The value of the Ekman number, $E$, plays a significant role since the Coriolis forces could facilitate convection, thus the value of $R_{a_c}$ depends on $E$. Al-Shamali et al. (2004) present a systematic study of parameters for the onset of convection in spherical shells at various shell thicknesses. They analysed the effect of the shell geometry on the critical Rayleigh number for convection, $R_{a_c}$, as well as investigated the influence of $E$. They found the relation:

$$R_{a_c} E^{1.16} = \frac{0.21}{\chi^2} + 22.3\sqrt{\frac{1-\chi}{1+\chi}}, \tag{2.1}$$

where $\chi = r_i/r_o$ is the ratio between the inner and outer core radii.

They also discussed the flow patterns for different geometries for Rayleigh numbers just above $R_{a_c}$. Hot plumes are formed at the inner-outer core boundary, and are found regularly spaced with a characteristic azimuthal wave-number $m_c$. For their study $m_c$ depends on $E$ and $\chi$. For a given $E$, $m_c \propto r_i$, that is, for thinner shells (high $\chi$) there are more plumes than for thicker shells (low $\chi$).

$R_a$ for the onset of dynamo action ($R_{a_d}$) have been previously studied for Earth's geometry. Grote et al. (2000) studied the effect of the magnetic Prandtl number, $P_m$, for various Rayleigh numbers, $R_a$. They found quadrupolar solutions for low $R_a$ (just above $R_{a_d}$) and low $P_m$. For higher values of $P_m$ and low $R_a$ their simulations result in dipolar and stable dynamos, becoming chaotic for increasing $R_a$. The temporal behaviour of the resultant field is highly dependent on the fluid properties (time variable versus stationary).

Heimpel et al. (2005a), presented a study on the onset of dynamo action as a function of radius ratio $\chi$. Their results showed that the inner core size characterizes the geometry of the field. They also found that the magnitude of the radial magnetic field at the outer boundary is affected

by the value of $\chi$. In this chapter, we include the results presented by Heimpel et al. (2005a). To further explore the generation of dynamo action, we study the influence of $E$, and $\chi$ on $R_{a_d}$, the Rayleigh number for the onset of dynamo. Rather than a theoretical approach taken by Jones et al. (2001) for finding $R_{a_c}$, we use a numerical approach similar to Al-Shamali et al. (2004). We studied a specific set of parameters, varying the radius ratio for two different $E$. Using as a base curve the actual values for onset of convection found by Al-Shamali et al. (2004), $R_a$ was increased until a self-sustained dynamo was found. In section 2.2 we describe the methodology used for our study. In section 2.3 we present the results from 95 different simulations that we include in this study. Lastly, in section 2.4 the discussion of how the external magnetic field is a diagnostic of the internal geometry as well as the conclusions of this study are included.

## 2.2   Numerical Model and Methodology

As described in section 1.2, we use a model based on magnetohydrodynamics (equations 1.1-1.4). We study numerical simulations for various $R_a$ and $\chi$ using two different Ekman numbers and two variants in initial conditions.

Since the numerical code yields a discrete solution, a grid needs to be defined for the simulations. It is necessary to change the resolution for varying parameters. Higher $R_a$ and lower $E$ require higher grid resolutions. The same is true for thinner shells. We choose the radial resolution based on the convergence of the numerical solution and the thickness of the Ekman boundary layer, $D\sqrt{E}$. The Ekman boundary should contain at least 4 radial levels of the defined grid. The latitudinal grid is chosen so that the cells at the equator in the middle of the fluid domain are almost square. The distribution of the latitudinal grid follows the location of the zeros of the Legendre polynomial of degree, $l_{max}$, and the distribution is found for a specific grid using the Gauss quadrature. The longitudinal grid is regularly spaced in angle and it is always chosen to have similar angular resolutions (but with a different distribution) as the latitudinal direction (figure 2.1).

For all the runs, we choose non-slip boundary conditions for the velocity, and the boundaries are kept at a constant temperature. The outer boundary is chosen to be electrically insulating and the inner boundary is electrically conductive.

All the simulations feature an electrically conductive inner sphere with a magnetic diffusivity being the same as for the fluid envelope. We also used a magnetic Prandtl number $P_m = 5.0$, and a Prandtl number of $P_r = 1.0$. Two sets of simulations with Ekman numbers $E = 1 \times 10^{-3}$ and $E = 3 \times 10^{-4}$ are presented in this chapter. The Rayleigh number is changed within a small range just above the critical Rayleigh number for convection, between 1.5 and 10 times $R_{a_c}$. The radius ratio, $\chi$, varies between 0.15 and 0.85.

The initial conditions are chosen to be the same for all the runs: the velocity field is initialized to zero, relative to the rotating frame; a random temperature perturbation is added to the reference state (the perturbation has a maximum amplitude of $T_{ini}$ over the central shell, $r = (r_o + r_i)/2$); the poloidal magnetic field is initialized with $l = 1$ and $m = 0$, and amplitude $B_{ini}$ at $r_i$; the toroidal component is defined with $l = 2$ and $m = 0$ and a maximum amplitude $B_{ini}$ at
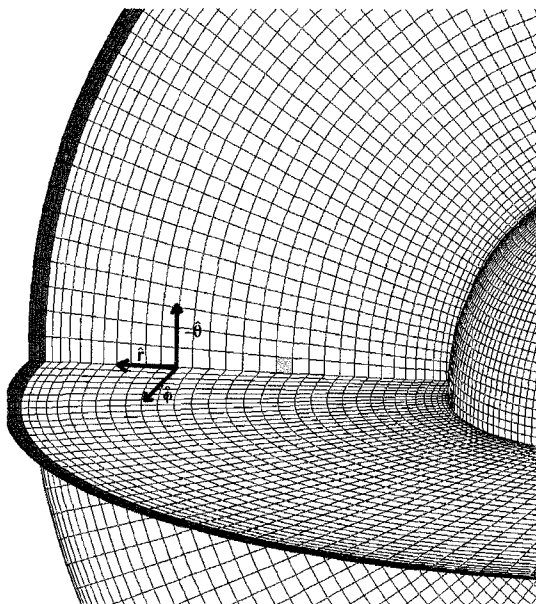
Figure 2.1: Grid used for a low resolution run. This simulation uses 41 radial levels with a Chebyshev distribution, 160 levels in latitude using a Gauss quadrature rule for the $\theta$ distribution, and $160 \times 2 = 320$ levels in azimuth, regularly distributed. The grey zone highlights the cells in the Ekman layer at the outer boundary for $E = 10^{-3}$. The blue cell is roughly midway through the fluid core, $r = (r_o + r_i)/2$, and the $\theta$ distribution is chosen for this cell to be square (some distortion is caused by the perspective).

$r_o/2$; and the radial component is initialized such that $\partial_r J_r = 0$, where $J_r$ is the radial electrical current. For the simulations presented here, the low amplitude initial condition (LAIC) case is defined by values for $B_{ini} = 0.5$ and $T_{ini} = 0.05$. The cases of high amplitude initial condition (HAIC) are defined by $B_{ini} = 5.0$ and $T_{ini} = 0.10$.

Figures 2.2-2.5 show a simulation with $\chi = 0.35$ $R_a = 1.12 \times 10^5 = 2R_{a_c}$, $E = 10^{-3}$, $P_r = 1$, and $P_m = 5$, at its fifth time step. The effect of the temperature perturbation has affected the velocity field and modifies the resultant magnetic field to some extent (see figure 2.5).
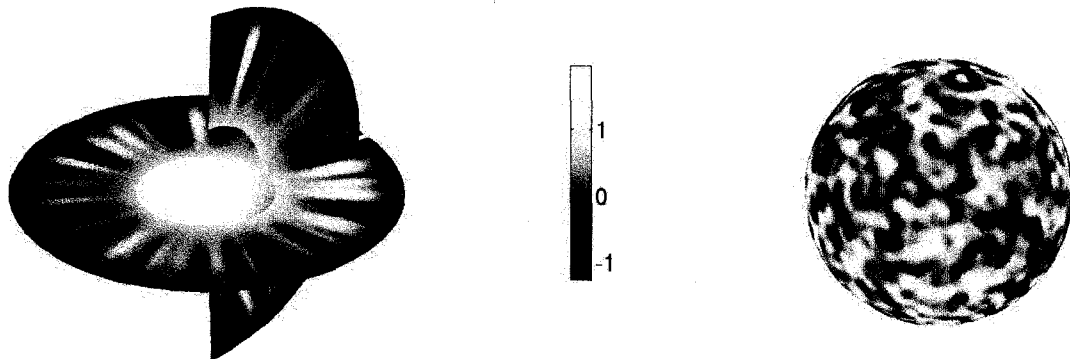


Figure 2.2: Normalized temperature inside the simulated fluid. On the left side, an azimuthal and longitudinal cut from an example run where $\chi = 0.35$. On the right, the same snapshot but on a spherical shell at $r = (r_i + r_o)/2$.
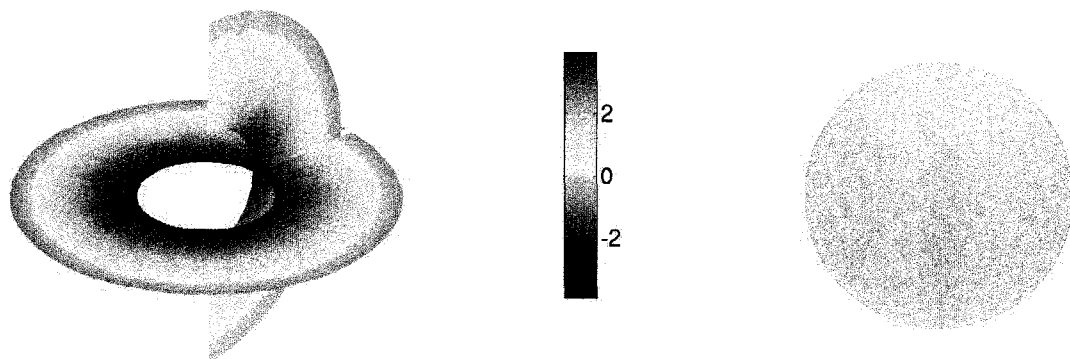


Figure 2.3: Magnetic field in the direction of $\theta$, $B_\theta$. This is the same snapshot as presented in figure 2.2 and the same azimuthal, longitudinal and spherical cuts.

We did not use any hyperdiffusivities in our models. Hyperdiffusion refers to a damping mechanism used in spectral domain to guarantee the stability of the numerical solution by controlling the energy stored in higher order harmonics. The convergence for all our runs is obtained using a small enough time step and high enough resolutions so that hyperdiffusivities are not necessary. We discard its use in order to avoid numerical artifacts in the solution, even though avoiding them is computationally more expensive.
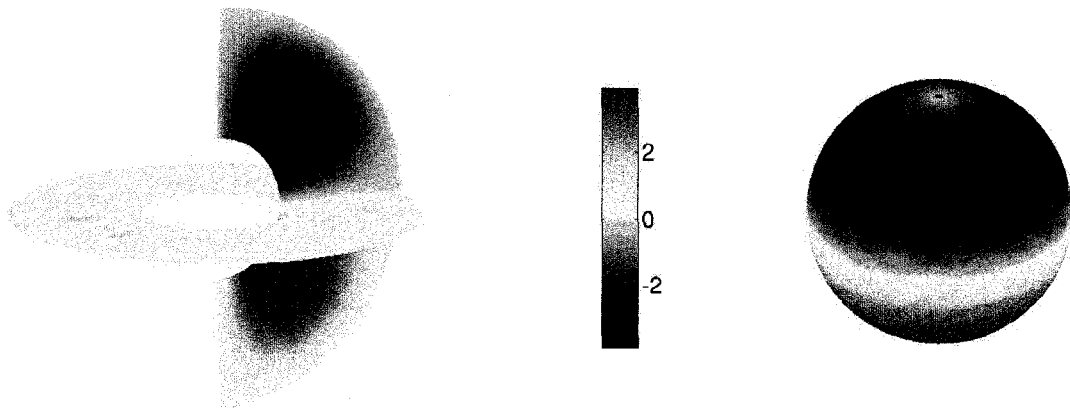
Figure 2.4: Magnetic field in the direction of $\varphi$, $B_\varphi$, using the same conditions as in the previous figures (Fig 2.2 and 2.3). The northern hemisphere has a retrograde direction for the magnetic field while the southern hemisphere is initialized with a prograde magnetic field vector.
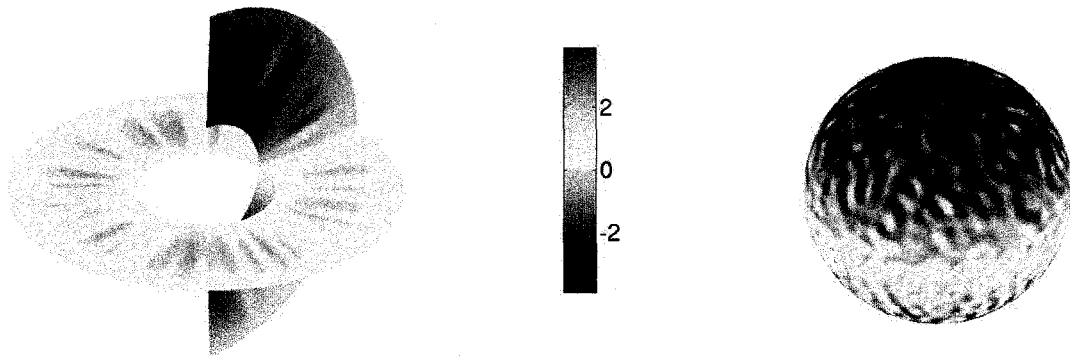


Figure 2.5: Radial component of the seed magnetic field. This is a snapshot of the 5th time step, and the temperature has modified the velocity and the radial magnetic field already. The field points inward on the southern hemisphere and outwards in the northern, decaying in magnitude at the equator.

As stated previously, we use, as a base, numerical results from the Al-Shamali et al. (2004) for the onset of convection in rotating shells. $Ra$ is increased above the critical Rayleigh number for convection, $Ra_c$. This is done systematically until a self sustained dynamo is found (where the magnetic field is sustained by the fluid motion). The definition for sustained or failed dynamos is simple: the cases where the magnetic field energy decreases exponentially three orders of magnitude or more from its initial value is a failed dynamo. If it has a constant average energy for at least $\tau_\lambda$, the magnetic diffusion time (see page 7), it is a self-sustained dynamo. The time series of the total kinetic and magnetic energy stored in the fluid is calculated and presented for different values of $R_a$ in figure 2.6 to illustrate the definition of failed and sustained dynamos.
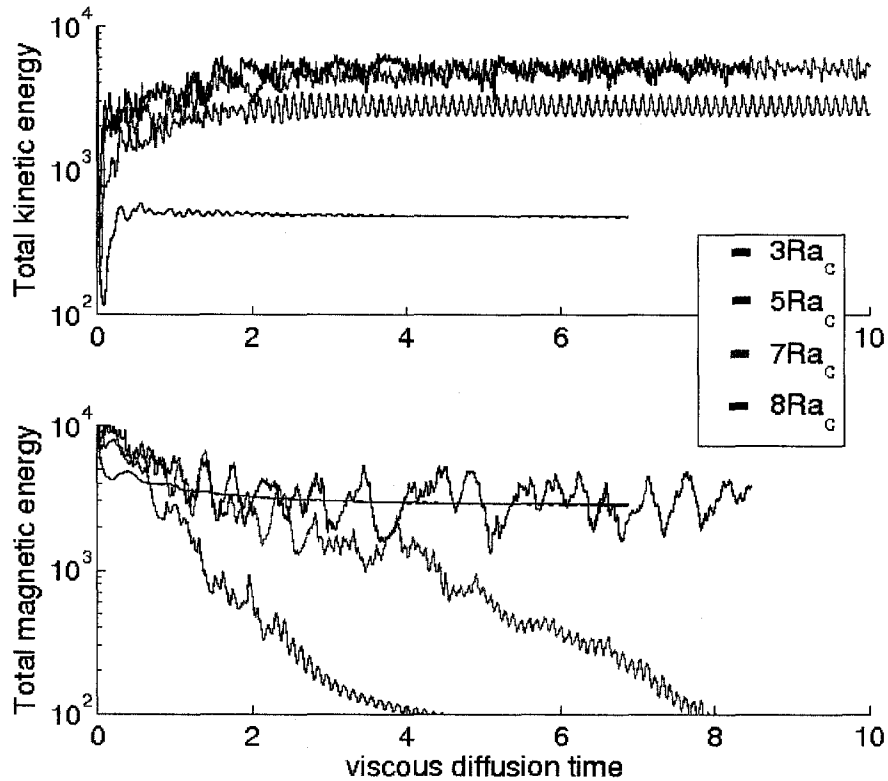


Figure 2.6: Time series of kinetic (top) and magnetic (bottom) energies on the fluid core. Four runs with the same radius ratio ($\chi = 0.15$) are presented here for varying $R_a$. Green, blue, purple, and black curves correspond to $3Ra_c$, $5Ra_c$, $7Ra_c$, and $8Ra_c$, respectively. The simulations here represent four of the points in Fig 2.7(b); two failed and two sustained dynamos.

For all four time series shown in figure 2.6, the radius ratio is set to $\chi = 0.15$. In general, the critical Rayleigh number for dynamo action, $Ra_d$, is the lowest $R_a$ for which the dynamo is sustained. As it has been shown here, in some cases this is not a critical value as it is for convection since there are failed dynamos with a $R_a > R_{a_d}$ for a given $E$ and $\chi$ (figure 2.6).

## 2.3 Results

Summarizing the results, figure 2.7 presents all failed (open symbols) and sustained (solid symbols) dynamos found in this study. The curve for the onset of convection is included in a coloured solid line and the grey lines above it represent integer multiples of the $R_{a_c}$ line.



(a)

(b)

(c)
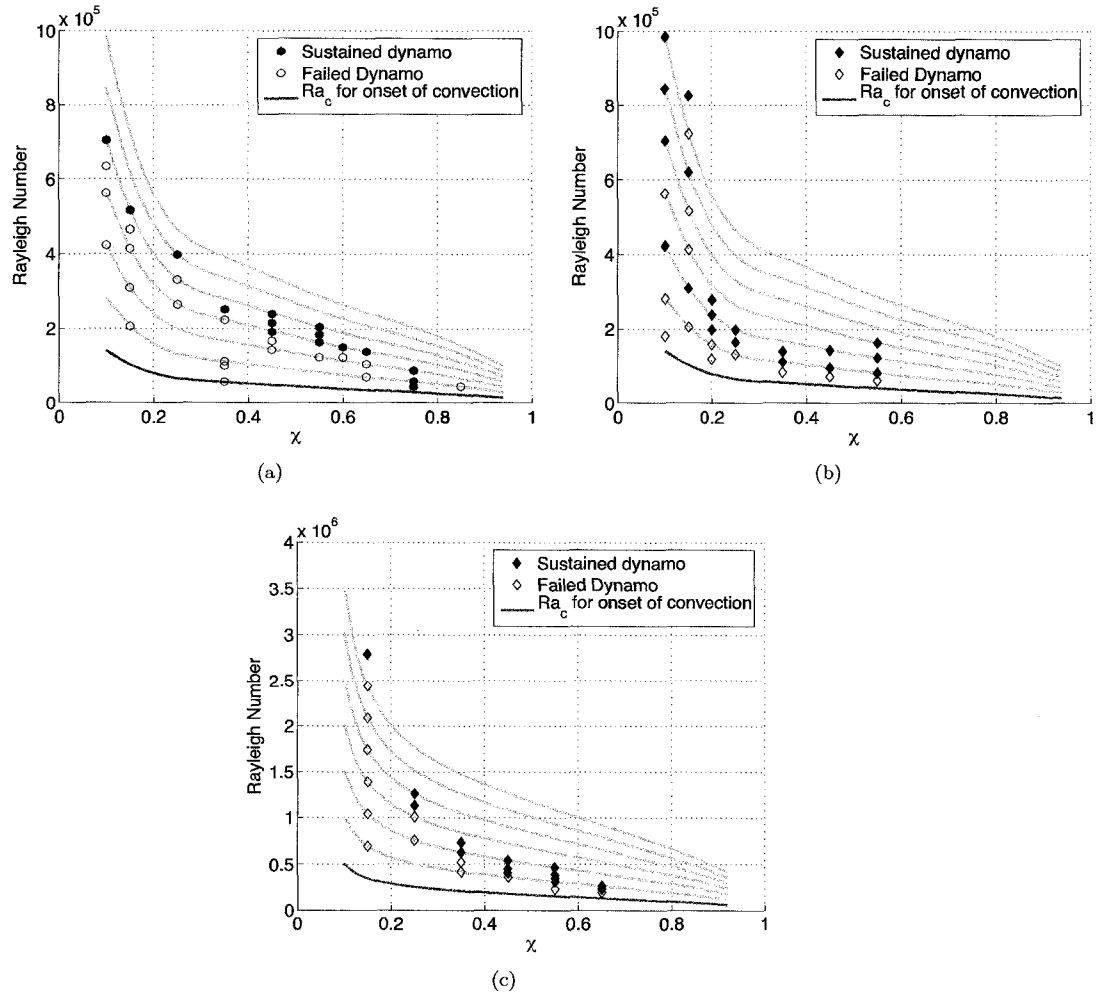
Figure 2.7: For different amplitudes of the initial seed magnetic field and temperature, the onset of dynamo for $E = 10^{-3}$ was found as a function of the radius ratio, $\chi$ for (a) low field, and (b) high field initial conditions. On the bottom, (c), results for Ekman number $E = 3 \times 10^{-4}$, and the high field initial conditions amplitude.

The Rayleigh number for the onset of dynamo action, $R_{a_d}$, decreases with increasing $\chi$. A change in regime is found for high $\chi$ for LAIC where the widest radius ratio was explored. Before $\chi = 0.65$ the curve found for $R_{a_d}$ seem very smooth varying between 5 and 3 times $R_{a_c}$ curve. This trend is broken for $\chi = 0.75$. A more careful and complete analysis of high $\chi$ values is

needed if one wants to determine when the fluid stops supporting a field. We know that $R_{a_d}$ will depend on parameters like $E$ and $P_m$ due to the effects of the magnetic and viscous diffusivities in the dynamics of the system.

For all three graphs there is a steep increase of $R_{a_d}/R_{a_c}$ for thick shells, with the sharpest increase for the lowest $E$. There is not an abrupt transition between thin and thick shell dynamos indicated by the behaviour of $R_{a_d}$. The three cases presented here, have a smooth curve for $R_{a_d}$ if we do not take into account the very thin shell range ($\chi \geq 0.65$).

We include the total magnetic and kinetic energy densities for the dynamos with the lowest $R_a$, $R_{a_d}$, found for all simulations. The error bars represent the standard deviation of the time series. The average was taken for the stable part of the time series. They were chosen individually for every time series. For the green data set (HAIC $E = 10^{-3}$) in figure 2.8 the average is always dominated by the magnetic energy. Both energy densities show linear form with increasing $\chi$ in the semi-logarithmic plot used, and both lines are almost parallel. The same is true for intermediate values of $\chi$ in the blue data set (LAIC $E = 10^{-3}$). The linear trend is not so evident for the orange data set (HAIC $E = 3 \times 10^{-4}$), there is a change in behaviour around $\chi = 0.35$. For thin shells the kinetic energy decreases with $\chi$ while for thick shells it increases with $\chi$.
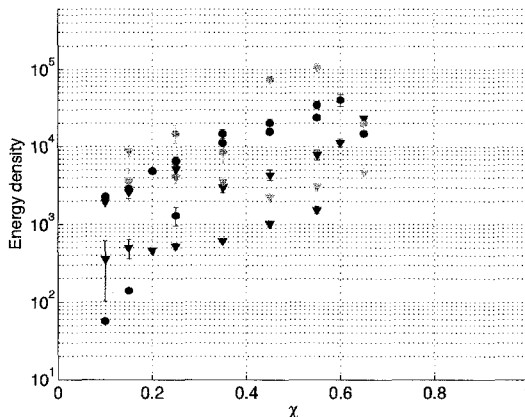


Figure 2.8: Time averaged energy densities as a function of $\chi$ for the first (lowest $R_a$) dynamo found. In the graph, triangles ($\nabla$) show kinetic and circles ($\circ$) magnetic energy densities. The colours refer to the three data sets in figure 2.7: Blue is LAIC with $E = 10^{-3}$, green is HAIC with $E = 10^{-3}$, and orange is HAIC with $E = 3 \times 10^{-4}$.

Since the linear trend in the kinetic and magnetic time average seem to have the same slope, we calculate the ratio between magnetic and kinetic time series and use the standard deviation of the series as the error bars presented in figure 2.9. In this graph, a noticeable transition between thin shell and thick shell geometries is seen. For thick shells the energy ratio increases with $\chi$, thin or intermediate thickness shells present almost a flat profile for this ratio. There are a couple of points where $\chi \geq 0.6$, for which this ratio is reduced again. The maximum ratio is found for intermediate shell thickness.
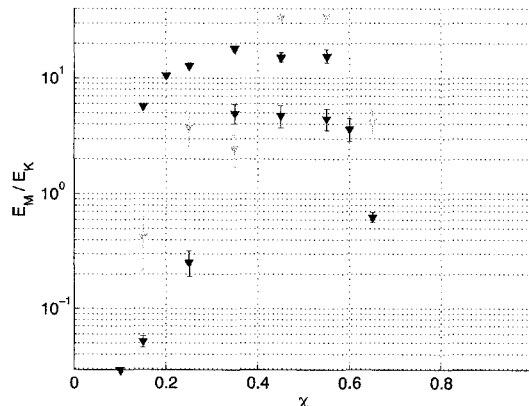
Figure 2.9: Time averaged of the ratio between the total magnetic over total kinetic energies. The colours as in figure 2.8 represent the lowest $R_a$ found for the three data sets.

The CMB radial component of the magnetic field is of particular interest in dynamo simulations, since it is the only component one can detect away from the dynamo region (see appendix B). We present in figure 2.10 the dipolar component over the total energy at CMB. There is subtle change in the curve between thin and thick shells for each set. The different results for the CMB component result partly from the initial conditions used. For the same $E = 10^{-3}$ both sets, LAIC and HAIC (blue and green respectively), result in significantly different dipolar components at CMB. In the HAIC case a highly dipolar field is produced that dominates over other degrees of the field with between 60% and 80% of the total CMB radial field. In contrast, for the LAIC case, the dipolar component does not exceed 50%, reaching less than 10% for high values of $\chi$.

We found a weak correlation between the dipolar component at the CMB and the ratio of magnetic and kinetic energy densities (see figure 2.9 and 2.10). Where the magnetic energy is an order of magnitude larger than the kinetic energy, the resultant field is dominantly dipolar. The cases where the dipolar component of the field is particularly weak are found when the ratio between magnetic and kinetic energy densities is less than one (i.e. weak dynamos).

The percentage of the dipolar component in the radial magnetic field at the CMB is useful, but insufficient for a complete understanding of the measurable field. We include in figure 2.11 the ratio between the quadrupolar ($a_q$) and dipolar ($a_d$) components that is defined as $r_{qd}$. As well, the octupolar ($a_d$) to dipolar components ratio is defined as $r_{od}$. This figure shows the general trend of the most significant harmonics. For all simulations the field is dominantly dipolar, and the ratios in figure 2.11 are always lower than one. The least dipolar set, the blue circles, have higher quadrupolar and octupolar components. This is not unexpected since the LAIC resulted in a higher values of $R_{a_d}$, and it has been widely reported in the literature that the relative magnitude of higher harmonic components of the magnetic field increases with increasing $R_a$, (e.g. Kutzner & Christensen (2002), Grote et al. (2000)). Similarly, the dynamos that were sustained with a lower value of $R_a$ are found to be more dipolar, see HAIC and $E = 10^{-3}$ in
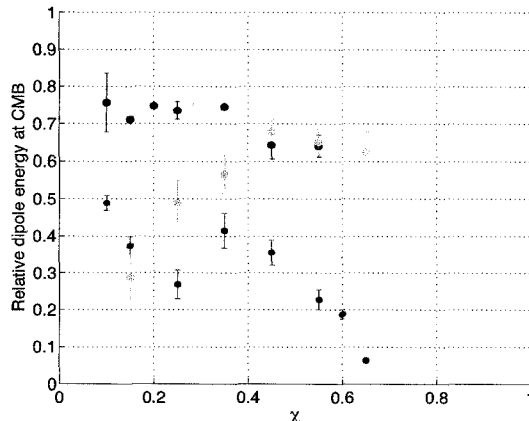
Figure 2.10: Plot of the time averaged, relative dipolar energy at the CMB versus $\chi$. Colours still follow the same code as in previous figures: Blue is LAIC with $E = 10^{-3}$, green is HAIC with $E = 10^{-3}$, and orange is HAIC with $E = 3 \times 10^{-4}$. For HAIC, higher values of $\chi$ result in the same percentage of dipole at CMB, just above 60%. For all three cases one can see the difference in behaviour between thin and thick shells, changing for $\chi \sim 0.4$.

green. For the orange data set, HAIC and $E = 3 \times 10^{-4}$, extreme (low and high) values of $\chi$ required a higher supercritical $R_a$, and thus the there is a more dominant quadrupole and octupole components. For intermediate values of $\chi$, the dominance of the higher degrees in the magnetic field geometry is diminished.

## 2.4 Discussion and Conclusions

### 2.4.1 Constant outer core radius versus constant shell thickness

Planetary solid iron cores in terrestrial planets are expected to grow while they crystallize and cool with time. The outer core is constant for all models and the shell thickness changes with time. It is useful then, to present our results with units other than what is merely convenient for the numerical model. We redefine $R_a$ based on the core size, $r_o$, instead of the shell thickness $D$. For increasing $\chi$, the thickness of the shell diminishes and the core radius, $r_o$, remains constant. A new *planetary Rayleigh number* may be defined based on $D = r_o(1 - \chi)$,

$$R_a^{pl} = R_a \left(\frac{r_o}{D}\right)^3 = \frac{R_a}{(1 - \chi)^3}. \tag{2.2}$$

In figure 2.12, we present $R_a^{pl}$ for onset of dynamo as function of $\chi$ for the three data sets. For the case with $E = 3 \times 10^{-4}$ (figure 2.12(c)), $R_{a_d}^{pl}$ has a minimum value around $\chi = 0.35$. For the other 2 data sets, $R_{a_d}^{pl}$ increases with $\chi$ without showing a significant increase for lower $\chi$, as it is clearly found for the first mentioned data set. The decrease in the Ekman number requires a significantly higher supercritical $R_a^{pl}$ for low values of $\chi$, this means that thick shell dynamos
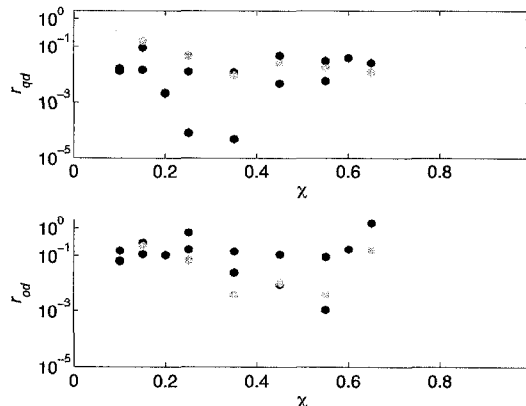
Figure 2.11: From the time averaged poloidal energy at CMB, the dipolar $(a_d)$, quadrupolar $(a_q)$ and octupolar $(a_o)$ components are taken, and ratios $r_{qd} = a_q/a_d$ and $r_{od} = a_o/a_d$ are calculated. In this figure, these ratios are plotted as a function of $\chi$; the plot uses the same colour code previously described, e.g. figure 2.10.

become more energetically expensive, in terms of $R_{a_c}$, for lower $E$.

## 2.4.2  Shell thickness

We find distinctive characteristics in the magnetic field at the CMB for varying $\chi$. The characteristic flows for different shell thicknesses result in signature radial fields that depend on $\chi$. Similar to non-magnetic convection (Al-Shamali et al. (2004), Jones et al. (2001)), the flow pattern in the dynamo region depends strongly on the radius ratio. In the cases where $R_{a_d}$ is not highly supercritical (below $\sim 4R_{a_c}$), the convection is quasi-stationary and an azimuthal periodicity is found (see figure 2.13). Hot plumes rise from the ICB and are tilted in the retrograde direction. The tilt is a direct result of conservation of angular momentum on the Taylor column and it is caused by the shape of the top and bottom boundary of the column (see Busse (2002)). For higher $R_a$, which is required for LAIC dynamos, the convection becomes non-stationary. It is important to note that for very low values of $\chi$, given that the number of plumes is proportional to $\chi$, we find the magnetic field being supported by a single plume. These geometries develop a dynamo where the magnetic field is azimuthally localized (as a result of the azimuthally localized flow). The thermal plumes define the shape of the velocity field. Axial vorticity, $\omega_z = (\nabla \times \mathbf{u}) \cdot \hat{\mathbf{z}}$, creates column pairs with cyclonic and anti-cyclonic directions. They are organized around the rising thermal plumes (see figure 2.15). These columns are quasi-geostrophic, the variation on the velocity field as a function of $z$ is small when compared with the azimuthal direction. The behaviour of the flow may be separated into two major zones defined by the tangent cylinder (see figure 1.1 for an illustration of the tangent cylinder). Outside the tangent cylinder, the convection develops columnar structures for the velocity field, where the columns are parallel to the axis of rotation. Depending on $R_a$, few plumes rise inside the tangent cylinder from the ICB axially towards the CMB.
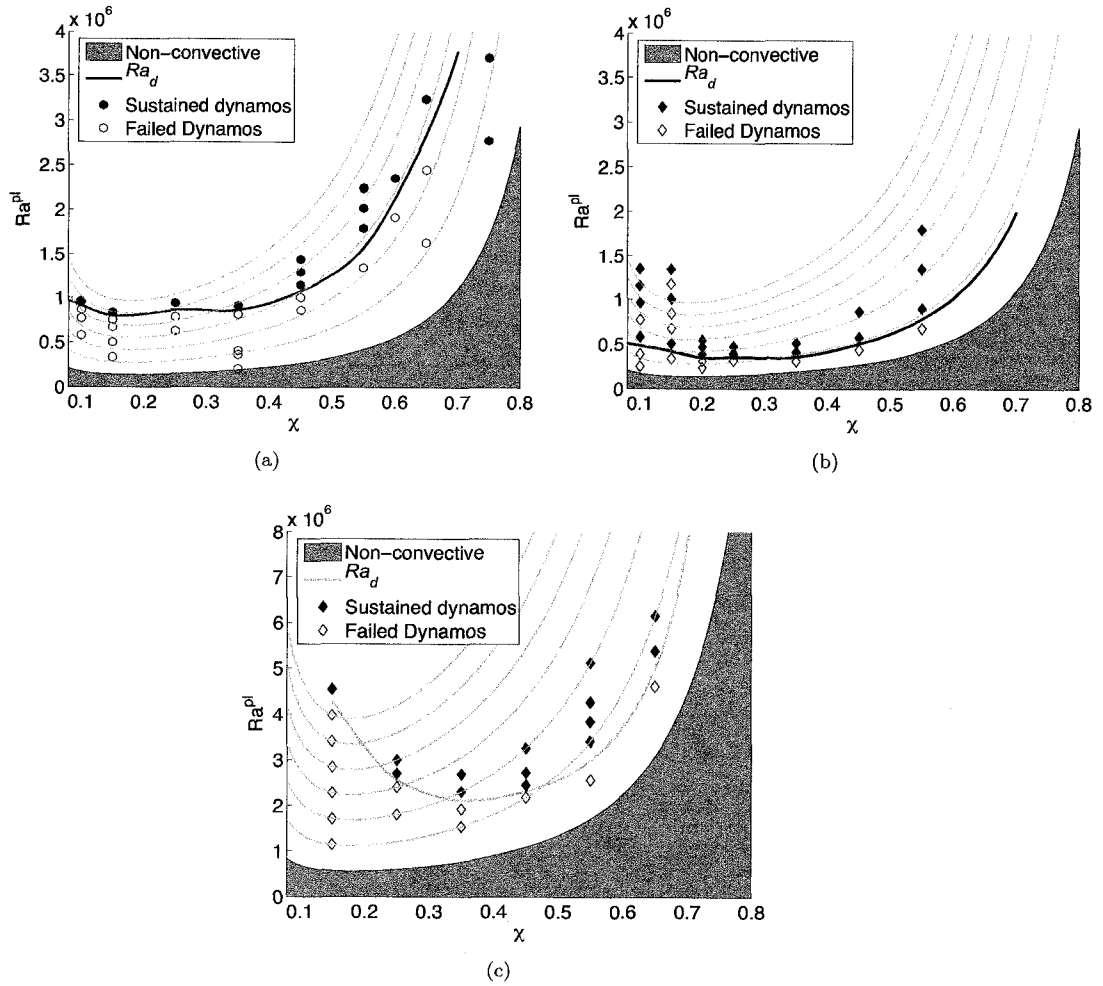
Figure 2.12: Similar to figure 2.7 but plotting $Ra^{pl}$ instead of the Rayleigh number. On the top, both sets with $E = 10^{-3}$ using (a) LAIC, and (b) HAIC. On the bottom, (c), results for $E = 3 \times 10^{-4}$ and HAIC. We include in this graph a rough interpolation for $R^{pl}_{a_d}$ using colours from previous graphs to identify each data set.
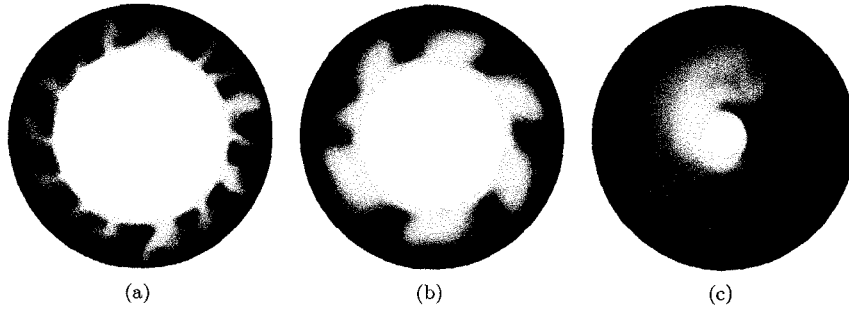
Figure 2.13: An equatorial cut of the temperature seen from the north pole. For the left panel (a), $\chi = 0.65$ using LAIC, $R_a = 4R_{a_c}$ and $E = 10^{-3}$. In the central panel, (b), $\chi = 0.55$ with HAIC, $R_a = 2R_{a_c}$, and $E = 10^{-3}$. And finally for the right hand side, (c), $\chi = 0.15$ with HAIC, $R_a = 9R_{a_c}$, and $E = 3 \times 10^{-4}$.
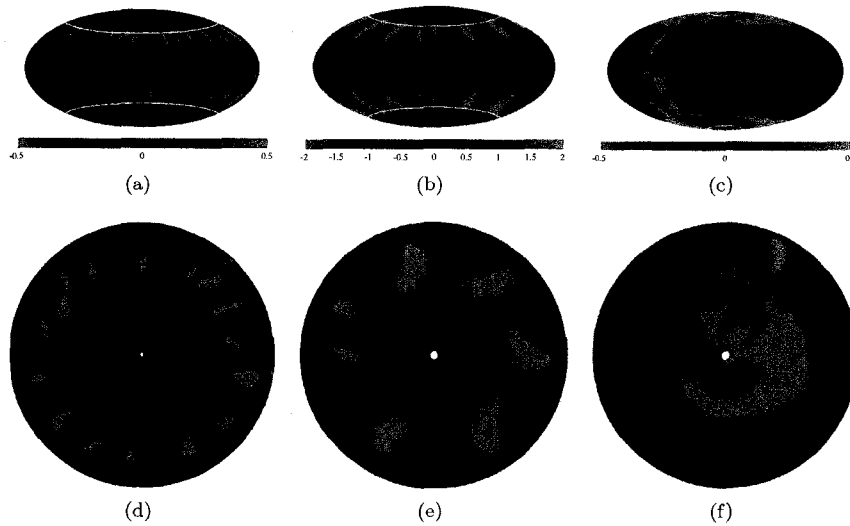


Figure 2.14: On top, the magnetic field is shown at the outer boundary using a Hammer projection. The tangent cylinder at this outer boundary is marked with a white line. On the bottom, a polar view of the radial component of the magnetic field at the CMB, the outer most boundary. The same scale is used for each model and the colour bar is valid for each column. Panels left, center and right, show the results for three $\chi$ values for different simulation parameters (same as used in figure 2.13)

(a)                          (b)                          (c)
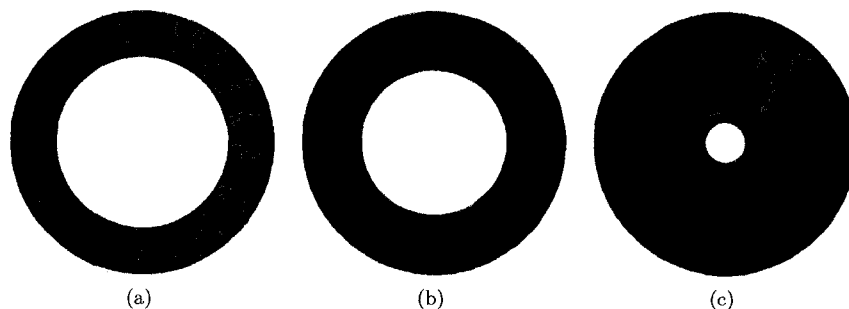
Figure 2.15: Graphs of vorticity in the direction of the axis of rotation, $\omega_z$. With a view from the north pole, an equatorial slice shows the cyclonic (red) and anticyclonic (blue) vortices. The three panels show the results from the simulations used in figure 2.13 and 2.14

The pair of cyclonic and anti-cyclonic columns collect and carry the magnetic field lines with them. The position of maximum magnitude patches of the radial magnetic field at the surface is correlated with the thermal plumes at the equatorial plane and the vorticity columns. The magnetic field maximum patches are found at a higher $\varphi$ angle (retrograde direction) with respect to the equatorial thermal plumes. The vorticity columns are tilted in the retrograde direction in the same fashion as the thermal plumes. At the CMB these columns are spread over a wider area than they are at the equator, and the magnetic field lines are pushed outward when the column reaches the CMB (where the flow is redirected in direction to the equator). The radial magnetic field lines on the CMB drift with respect to the thermal plumes since they are produced by the change in direction of the flow.

In addition to the surface structure of the radial magnetic field, the magnitude of the field is a diagnostic for the internal dynamo. The magnetic field of Mercury, for example, has an average magnetic field three orders of magnitude lower than those of Saturn or Jupiter and also significantly lower than the Earth's field (Stevenson (2003)). We present here the Elsasser numbers calculated for $R_{a_d}^{pl}$ (table 2.1). The Elsasser number is defined as the ratio between the Lorentz and the Coriolis forces in the system and may be expressed as:

$$\Lambda = \frac{\langle B^2 \rangle}{\rho \mu_o \lambda \Omega}, \tag{2.3}$$

which is equivalent to

$$\Lambda = \frac{E\, P_m\, [E_m]}{1 - \chi}, \tag{2.4} \qquad \Lambda_{r_o} = E\, P_m\, [E_{r_o}] \frac{1 - \chi^3}{3(1 - \chi)}, \tag{2.5}$$

where $[E_m]$ is the time averaged magnetic energy of the whole fluid core, and $[E_{r_o}]$ is the time averaged magnetic poloidal energy at the CMB ($r = r_o$). The energy series obtained from MagIC (see for example figure 2.6) scale with the kinetic energy; we convert it here to the equivalent

Table 2.1: Elsasser number for the lowest $R_a$ dynamo for various shell thicknesses. Three data sets are organized by the value of $E$ as well as the initial field amplitude. $\Lambda$ is the Elsasser number calculated with $[B^2]_{rms}$ over the fluid core. $\Lambda_{r_o}$ is averaged only over the outer boundary.

| $E$ | Initial condition | $\chi$ | $R_a/R_{a_c}$ | $\Lambda$ | $\Lambda_{r_o}$ |
|---|---|---|---|---|---|
| $10^{-3}$ | LAIC | 0.10 | 5.0 | 0.27 ± 0.03 | 0.0013 ±0.0001 |
| | | 0.15 | 5.0 | 0.71 ± 0.10 | 0.0042 ±0.0003 |
| | | 0.25 | 6.0 | 4.80 ± 2.50 | 0.0538 ±0.0216 |
| | | 0.35 | 4.5 | 57.99 ±38.80 | 1.4781 ±0.8875 |
| | | 0.45 | 4.0 | 124.62±24.91 | 3.3420 ±0.5611 |
| | | 0.55 | 4.0 | 276.55±47.53 | 7.8840 ±1.4196 |
| | | 0.60 | 4.0 | 371.14±88.23 | 10.2984±2.2262 |
| | | 0.65 | 4.0 | 91.15 ±74.59 | 1.7151 ±1.1336 |
| $10^{-3}$ | HAIC | 0.10 | 3.0 | 10.34 ± 4.11 | 0.2174 ±0.1962 |
| | | 0.15 | 3.0 | 14.89 ± 1.42 | 0.1423 ±0.0510 |
| | | 0.20 | 2.5 | 22.41 ± 0.82 | 0.7092 ±0.0196 |
| | | 0.25 | 2.5 | 32.52 ± 5.81 | 1.3345 ±0.1405 |
| | | 0.35 | 2.0 | 57.63 ± 8.95 | 3.1403 ±0.4778 |
| | | 0.45 | 2.0 | 100.30± 6.35 | 5.9697 ±0.3746 |
| | | 0.55 | 2.0 | 191.71±16.73 | 14.3389±1.1384 |
| $3 \times 10^{-4}$ | HAIC | 0.15 | 8.0 | 4.86 ± 2.65 | 0.0226 ±0.0124 |
| | | 0.25 | 4.5 | 19.57 ± 5.92 | 0.1584 ±0.0489 |
| | | 0.35 | 3.0 | 14.59 ± 5.54 | 0.1590 ±0.0607 |
| | | 0.45 | 2.2 | 9.73 ± 5.95 | 0.2789 ±0.0853 |
| | | 0.55 | 2.0 | 13.33 ± 0.26 | 0.8060 ±0.0028 |
| | | 0.65 | 1.8 | 61.15 ± 5.09 | 4.2944 ±0.4847 |

Elsasser number. The factor on the right hand side of equation 2.5 appears from the normalization of the energy integral. In the case of the surface magnetic field the energy is normalized by the area of the surface $r = r_o$ and in the case of the whole fluid core the energy is normalized by the volume.

We find a maximum Elsasser number at the outer boundary, $\Lambda_{r_o}$, for intermediate shell thickness. The single plume dynamos develop a strong magnetic field at the interior, but only a small percentage of that magnetic energy reaches the outer boundary. Most of the magnetic energy is in the toroidal component, thus, it cannot be seen from the surface. For thin shells, $\Lambda_{r_o}$ is found to be small too but in this case the magnetic field over the fluid core is significantly smaller than for lower $\chi$. The intermediate shell thickness presents the highest $\Lambda$ and $\Lambda_{r_o}$. For $\chi \sim 0.35$ the dynamo sustained by the system requires a lower $R_a^{pl}$, (particularly for low $E$ ) and generated the strongest dynamo. The shell thickness may strengthen or weaken the magnitude of the magnetic field of the dynamo and it is optimal for shell geometries with $\chi$ between 0.25 and 0.45.

## 2.4.3   Planetary magnetic fields

Limitations in the numerical simulations force us to use a range of parameters different from what is expected for planetary interiors. The values chosen for our simulations for $E$ and $R_a$

are orders of magnitude different from what is expected for the Earth, see table 1.2. Based on a low viscosity of liquid iron and the known rotation rate, the estimated Ekman number for Earth is $E \sim 10^{-15}$ (de Wijs et al. (1998)). The critical Rayleigh number for convection, which scales as $E^{-4/3}$, results in $Ra_c \sim 10^{16}$. Fully three dimensional numerical simulations are restricted by grid resolution and it is not possible to reach such parameter range. However, an asymptotic regime has been found for which the dynamics of the fluid are not affected by viscosity even though the actual value of $E$ is greater than expected for Earth (Christensen & Aubert (2006)). After reaching this regime, the decrease in $E$ may not affect the dynamics of the system. Fully three dimensional numerical models have reached this regime and simulations where the effect of viscosity is negligible may be found in the literature, e.g. Olson & Christensen (2006). Our models are not in this asymptotic regime, nevertheless, a first order approximation of the dynamics of planetary interiors may be described by our high viscosity models. Models outside the asymptotic regime have been found to reproduce first order dynamics comparable with the behaviour of Earth's dynamo (e.g. Glatzmaier & Roberts (1995), Glatzmaier et al. (1999)).

In this chapter, we have described how two main diagnostic characteristics in the radial magnetic field at the boundaries depend on the radius ratio $\chi$. The latitude of the magnetic field patches of high intensity increases for lower $\chi$. Even though all fields found are dominantly dipolar, the variations in the spatial disposition of magnetic field at the CMB can clearly reveal the internal geometry that bounds the fluid core in which the magnetic field is generated. Based on this, if the mantle is thin enough (diffusion of magnetic field through isolating materials decreases the observable resolution) and the resolution of the measurements allow for these relatively high harmonic degree features to be determined, it is possible to find the thickness of the fluid dynamo layer inside a planet using the geometry of its magnetic field at the surface.

The ratio of the full volume $\Lambda$ with the outer surface $\Lambda_{r_o}$ decreases with increasing $\chi$. For low $R_a$, thin shell geometries are more successful at carrying a poloidal field at the surface, and thus, they have a higher surface magnetic field than thick shell dynamos. This is also supported by a tendency towards increased $\Lambda$ with increasing $\chi$. For all the simulations presented here, thick shells result in lower values of $\Lambda_{r_o}$. Only for the LAIC and $E = 10^{-3}$ we observe a decrease in the Elsasser number for a thin shell geometry, $\chi = 0.65$. Even though we do not find the same effect for the other two data sets, we expect $\Lambda$, as well as $\Lambda_{r_o}$, to decrease for very thin shells. For high values of $\chi$, the magnetic field cannot be sustained by the flow outside the tangent cylinder. It should be necessary then, to increase the value of $R_a^{pl}$ to support flow inside the tangent cylinder and thus to be able to sustain a dynamo. The increase in $R_a$ to highly supercritical values results in kinetic energies that are greater than magnetic energies. Weak dynamos are then expected under these conditions. Simulations using higher values of $\chi$ need to be performed to find whether they result in weak dynamos. In addition to the geometrical distribution of the magnetic field at the outer boundary, our results show that the Elsasser number $\Lambda_{r_o}$ gives a constraint on the geometry of the underlying dynamo.

The study of these data sets provides constrains on the magnetic fields generated by dynamo action under thin, intermediate and thick shell geometries. Dynamos with low Elsasser number,

such as Mercury, Uranus and Neptune (Stevenson (2003)) are then expected then to have either thin or thick geometries, since intermediate values of $\chi$ produce a high values of $\Lambda_{r_o}$. The Earth's core (which supports a dynamo with $\chi \sim 0.35$) has a high value of $\Lambda_{r_o}$, consistent with our findings. The dynamos of the gas giants may also be restricted to intermediate shell geometries (due to the value of $\Lambda_{r_o}$). This is true for Saturn for which interior models suggest a geometry of $\chi \sim 0.5$, for the dynamo region (Stevenson (1982), Guillot (1999b)). In the case of Jupiter, the interior models suggest a rather small value of $\chi$ which is not consistent with the results presented in this chapter. Note that our analysis is based on simulations with low values of $R_a$ and relatively high values of $E$. Additionally the boundary conditions used (non-slip boundaries) are more relevant for terrestrial planets than they are for gas giants or ice giants.

# Chapter 3

# Numerical models of zonal flow dynamos : an application to the ice giants[1]

## Abstract

The weakly dipolar and strongly tilted magnetic fields of Uranus and Neptune are apparently generated by a dynamo process distinct from that which produces axial dipoles. We study a suite of numerical dynamos driven by convection in a rapidly rotating spherical shell and focus on cases with relatively high magnetic diffusivity. Models are presented with magnetic Prandtl number $P_m = 0.1 - 5.0$ and Rayleigh numbers between 10 and 80 times the critical Rayleigh number for convection. In the cases with high magnetic diffusivity, the fluid flow has a dominant effect over the magnetic fields, which are characteristically quadrupolar and octupolar and strongly variable in time. The dipolar component is typically weak, and strongly tilted from the axis of rotation. Most of the cases we present result in low Alfvén and Elsasser numbers, in agreement with previous studies of non-dipolar dynamos. Our results suggest that the peculiar magnetic fields of Uranus and Neptune result from dynamo action driven by convectively generated, strong zonal flow in the electrolytic fluid envelope.

## 3.1 Introduction

The spacecraft Voyager II measured the planetary magnetic fields of Uranus and Neptune in 1986 and 1989, respectively. A preliminary model of these fields was made based on measurements covering periods of about 11 and 18 hours, and latitudes from 52°N to 78°S and 24°S to 0°, respectively. The proposed model was an offset tilted magnetic dipole OTD, (see Ness et al.

---
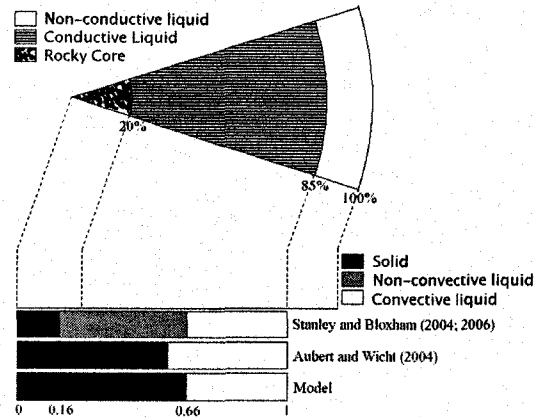
Figure 3.1: A model of Uranus' and Neptune's interiors. The figure compares the models of the interior with the geometry from previous numerical models. Based on gravity measurements, Hubbard et al. (1991) present different density profiles that we summarize in the wedge on the top part of the figure. The bars on the bottom represent the geometry used by numerical models of ice giants dynamos. These are Stanley & Bloxham (2004, 2006) and Aubert & Wicht (2004) On the bottom is the geometry used for our simulations, here marked as Model.

(1989, 1986)). The dipole component of each field is highly tilted (60° and 47° for Uranus and Neptune respectively) with respect to the rotation axis, and the dipole position is offset from the centre of each planet. Connerney et al. (1987, 1991a) and Connerney (1993) later presented a solution to the inverse problem based on all magnetic data obtained by Voyager spacecraft. This inversion was made in terms of the spherical harmonics (up to degree two for Uranus, and degree three for Neptune), and provides a better representation of the magnetic field at surface of the ice giants.

Based on gravity measurements taken by Voyager I and II, different models for the interior stratification of the ice giants have been proposed (Hubbard & Marley (1989), Hubbard et al. (1991), Podolak et al. (2000)). Figure 3.1 illustrates these models. The existence of a rocky core within each planet is possible, and would occupy less than 20% of the planetary radius. A liquid layer composed of water, methane and ammonia could extend out to 80% of the planetary radius. The outer deep atmospheric layer is composed of a mixture of molecular hydrogen and helium (Hubbard et al. (1991)).

The elevated temperatures of Uranus' and Neptune's interiors allow a mixture of ice forming components ($H_2O$, $CH_4$ and $NH_3$) to be in the liquid phase. Derived from the gravity models mentioned above, pressures and temperatures for which the liquid inside the ice giants becomes an electrolyte (with a non-negligible electrical conductivity) agree with the experimental results of Nellis et al. (1997). Shock experiments performed by this group also yielded values for the electrical conductivity of a "synthetic Uranus" mixture to be on the order of a few hundred (ohm m)$^{-1}$ to thousands of (ohm m)$^{-1}$. These values are small compared with the electrical conductivity of metals – liquid iron, for example, has an electrical conductivity at least 3 orders

of magnitude larger.

The density distributions proposed by the models of Hubbard & Marley (1989), Hubbard et al. (1991), and Podolak et al. (1991, 2000) result in a mostly homogeneous electrolyte layer. The most extreme variation represents roughly a factor of three increase of the fluid density near the rocky core boundary when compared with the density beneath the outer molecular H/He envelope. The region where dynamo action takes place is not likely to extend throughout the electrolyte liquid. It is plausible that convection occurs only in the top part of the electrolyte layer, from perhaps 50% of the planetary radius outwards, (Podolak et al. (1991)).

The Earth, Jupiter and Saturn all have highly dipolar magnetic fields more or less aligned with the rotation axis. Most numerical studies have focused on magnetic fields that are relatively stable in time and with a strong dipolar component (e.g. Christensen & Aubert (2006)). Some solutions also exhibit reversals in the direction of the magnetic dipole, analogous to polarity reversals of the magnetic field of the Earth (e.g. Kutzner & Christensen (2002), Glatzmaier et al. (1999)). Dynamo models in which the core geometry (i.e. the ratio of the inner to outer boundary of the convection region) is different from that of the Earth also are characteristically dipolar, even though the magnetic field geometry changes for different radius ratios (Heimpel et al. (2005a)). Weakly dipolar numerical dynamos have been shown to occur under conditions of vigorous convection, where inertia becomes strong relative to rotational (Coriolis) forces (Christensen & Aubert (2006); Olson & Christensen (2006)).

Using a spherical shell, single layer model near the onset of convection, Aubert & Wicht (2004) found equatorial dipole solutions. They obtained magnetic fields with the dipolar component being highly tilted with respect to the rotation axis, as observed for Uranus and Neptune. These equatorial dipoles were also characterized by a relatively weak magnetic field, as indicated by low Elsasser number. Such is the case for the ice giants where the Elsasser number, $\Lambda \sim 0.01$ (Stevenson (2003)).

One of the explanations for the non-dipolar field is derived from the internal structure of the planet. Based on the energy emission of the planets, Hubbard et al. (1995) proposed a stably stratified interior where the innermost part, as stated previously, from half the planetary radius inwards, cools via conduction. Based on this model, Stanley & Bloxham (2004) simulated a stratified liquid where they imposed different heat mechanisms for the two liquid layers. They used a small solid core, a non-convective fluid layer and a convective fluid layer. For the stratified models, the electrical conductivity was homogeneous throughout the simulated volume. That model resulted in a highly non-dipolar magnetic field such as those found for the ice giants.

A unique characteristic of the ice giants is the presence of a non-axisymmetric magnetic field. This characteristic, as well as the dominance of the quadrupolar and octupolar components, distinguishes the magnetic fields of the ice giants from those of other solar system dynamos. In this study, as in previous models applied to the ice giants (Aubert & Wicht (2004), Stanley & Bloxham (2004), Stanley & Bloxham (2006)), we assume that non-axisymmetric and non-dipolar magnetic fields are generated in the main dynamo region of the working fluid.

An alternative mechanism for producing both non-axisymmetric magnetic fields like those of the ice giants and strongly axisymmetric fields, like that of Saturn, is the presence of an

outer layer of conductive azimuthal flow that modifies the magnetic field produced by an internal dynamo, (Stevenson (1982)). Such an azimuthal flow would be expected to exist at the top of the liquid electrolytic envelope if the atmospheric zonal winds extend to great depths in the fluid envelope (Aurnou & Heimpel (2004), Aurnou et al. (2007), Heimpel et al. (2005b), Heimpel & Aurnou (2007)). Kinematic dynamos have been shown to generate non-axial and non-dipolar magnetic fields (under certain restrictions) on, for example, an axisymmetric imposed flow field, Holme (1997). The effect of azimuthal flow on magnetic field symmetry has been previously studied with multi-layer models, in which an internal dynamo is embedded in an outer layer that is subject to purely non-convective differential rotation. Schubert et al. (2004) studied a multi-layered kinematic dynamo, consisting of a solid inner core, a time-dependent convective layer where an $\alpha^2$ dynamo is generated, and an enveloping outer layer where a strong toroidal shear flow is imposed. They found that, independent of the symmetry of the internal dynamo model, axisymmetric outer flow models resulted in axisymmetric external magnetic fields and non-axisymmetric outer flow models resulted in non-axisymmetric external fields. Love (2000) presented steady two layer models with an internal kinematic dynamo and an outer differentially rotating azimuthal flow layer. That study found that both axisymmetric and non-axisymmetric magnetic fields can result from an axisymetric outer flow layer. Although the results of Love (2000) were primarily intended to apply to Saturn's highly axisymmetric magnetic field, the non-axisymmetric fields are interesting in relation to the models presented here – they show that non-axisymmetric magnetic fields, like those of the ice giants, may result from axisymmetric differential rotation.

In this paper we present single layer dynamical models (see figure 3.1) with vigourous convection and low electrical conductivities to simulate the dynamo region. We obtain non-dipolar dynamos sustained by dominantly zonal flows, characterized by strong radial and latitudinal shearing. For comparison, we also include some dynamos with higher electrical conductivity. The influence of varying Rayleigh number and magnetic Prandtl number is studied. In section 3.2 we present the model, the parameters and the boundary conditions used in our simulations. The results from the numerical models are presented in section 3.3. Lastly, in section 3.4, we discuss our results in the context of previous models. We find that models with strongly zonal flows result in non-dipolar dynamos. Thus, we propose that the idiosyncratic magnetic fields of the ice giants could arise from zonal flow dynamos.

## 3.2 Model and parameters

Dynamo action is driven by convection within a rotating spherical shell of thickness $D$, subject to a temperature difference, $\Delta T$, between the inner and outer boundaries. The boundaries are isothermal and the system rotates with an angular velocity $\Omega \hat{z}$, where we choose the z-axis to be in the direction of the angular velocity and $\hat{z}$ is the unit vector in the $z$ direction. The radius ratio of the outer $(r_o)$ and inner $(r_i)$ boundaries is chosen to be $\chi = r_o/r_i = 0.66$ (see figure 3.1). Gravity decreases linearly with depth.

The governing equations of magnetohydrodynamics with the Boussinesq approximation are

non-dimensionalised. Temperature is scaled by the temperature difference across the shell, $\Delta T$; distance by the shell gap width, $D = r_o - r_i$; time by the viscous diffusion time, $\tau_\nu = D^2 \nu^{-1}$, where $\nu$ is the kinematic viscosity; velocity by $\nu D^{-1}$; pressure by $\rho \nu \Omega$; and magnetic induction by $\sqrt{\rho \mu \lambda \Omega}$, where $\rho$ is the density, $\mu$ the magnetic permeability and $\lambda$ is the magnetic diffusivity of the fluid. The resulting set of non-dimensional equations are:

$$E\left(\frac{\partial \mathbf{u}}{\partial t} + \mathbf{u} \cdot \nabla \mathbf{u} - \nabla^2 \mathbf{u}\right) \quad + \quad 2\hat{\mathbf{z}} \times \mathbf{u} =$$

$$-\nabla P \quad + \quad \frac{R_a E}{P_r} \frac{g}{g_o} \hat{\mathbf{r}} T + \frac{1}{P_m} (\nabla \times \mathbf{B}) \times \mathbf{B}, \tag{3.1}$$

$$\nabla \cdot \mathbf{u} = 0, \qquad \nabla \cdot \mathbf{B} = 0, \tag{3.2}$$

$$\frac{\partial T}{\partial t} + \mathbf{u} \cdot \nabla T \quad = \quad \frac{1}{P_r} \nabla^2 T, \tag{3.3}$$

$$\frac{\partial \mathbf{B}}{\partial t} \quad = \quad \nabla \times (\mathbf{u} \times \mathbf{B}) + \frac{1}{P_m} \nabla^2 \mathbf{B}, \tag{3.4}$$

where $\mathbf{u}$ and $\mathbf{B}$ are the velocity and magnetic induction vectors, respectively; $T$ and $P$ are the temperature and pressure scalars, respectively; $g$ is the radially dependent gravity and $g_o$ is the gravity at the outer boundary; and $\hat{\mathbf{r}}$ is the radial unit vector.

Equations 3.1 to 3.4 are expressed in terms of the following non-dimensional parameters. The Rayleigh and Ekman numbers,

$$R_a = \frac{\alpha g_o \Delta T D^3}{\kappa \nu}, \tag{3.5} \qquad\qquad E = \frac{\nu}{\Omega D^2}, \tag{3.6}$$

where $\alpha$ is the thermal expansion coefficient and $\kappa$ is the thermal diffusivity; and the Prandtl and magnetic Prandtl numbers,

$$P_r = \frac{\nu}{\kappa}, \tag{3.7} \qquad\qquad P_m = \frac{\nu}{\lambda}. \tag{3.8}$$

We choose stress free boundary conditions for the velocity at the external boundary, and the internal velocity boundary condition is non-slip. The Prandtl number for all our simulations is $P_r = 1$. The electrical conductivity of the fluid is uniform throughout the volume, having the same value as for the rigid inner sphere. The electrical conductivity is defined by the magnetic Prandtl number $P_m$. In most cases the Ekman number is $E = 10^{-4}$, except for case 4 where $E = 3 \times 10^{-4}$. These numerical simulations required the use of weak hyperdiffusivities. The hyperdiffusion formulation used here is the same as that used in Kuang & Bloxham (1999) but the diffusion coefficient $\epsilon$ used here is smaller by a factor of roughly $1/500$. All models used the same grid resolution: 61, 256, and 512 levels for radial, latitudinal and azimuthal directions, respectively.

We study dynamos with a range of $P_m$ and $R_a$ (see table 3.1). Magnetic Prandtl numbers range from 0.1 to 5.0. Rayleigh numbers range from roughly 10 to 80 times the critical Rayleigh number for convection, $R_{a_c}$. The value of $R_{a_c}$ is based on Al-Shamali et al. (2004). We increase $R_a$ in cases 1 to 4 and to denote the increase in magnetic Prandtl numbers, $P_m$, we use letters A to C. The base cases with the intermediate value of $P_m = 0.3$ are not marked by any letter.

The numerical code used for these simulations implements a pseudo-spectral algorithm. We used a slightly modified version of MagIC 2.0 by Wicht (2002).

## 3.3  Results

Using the parameters stated in table 3.1 we find two failed dynamos (cases 1A and 2A), and seven self-sustained dynamos. We define failed dynamos to be those in which the magnetic field energy decreases exponentially three orders of magnitude or more from its initial value. If it has a consistent average energy for at least three magnetic diffusion times, it is a self-sustained dynamo.

The fluctuation of energy (magnetic and kinetic) as a function of time increases with $R_a$. The time series for two cases, with different $R_a$ (case 1 with $R_a \sim 11 R_{a_c}$ and case 4 with $R_a \sim 85 R_{a_c}$) but the same $P_m = 0.3$, are included in figure 3.2. Assuming the behaviour is quasi-stationary, we take the standard deviation of the time series as the fluctuation in the mean energy. Thus, table 3.1 shows how the variation in time (or the deviation in the energy average) for the kinetic and magnetic energy increases for increasing $R_a$. For example, the averaged toroidal kinetic energy in case 1 is $1.17 \pm 0.08 \times 10^6$, and the deviation is $\delta Kt = 7\%$ of the mean. For the most extreme example, the deviation in magnetic energy mean for case 4 is $\delta M_{Tot} \sim 70\%$, (figure 3.2).

A quasi-periodic oscillation in the energy time series is found in case 4 (figure 3.2). A similar oscillation is visible for cases 3 and 3A and also presents a 180° phase difference between the magnetic and the kinetic energies. The period of this oscillation is roughly 0.5 magnetic diffusion times for case 4, and 1 for both cases, 3 and 3A. In these latter two cases, the oscillation, which is more dominant for the initial part of the simulation, may be a transient state before reaching a quasi-stationary regime. For case 4 the oscillation is clearly dominant for the whole time series modelled. Another particularity of the time series of case 4 is a time interval where the magnetic field collapses (it decreases by almost two orders of magnitude) and the toroidal kinetic energy doubles, after this episode, which lasts roughly two magnetic diffusion times, the magnetic field recovers, and the toroidal kinetic energy decreases, returning to the oscillatory regime shown in figure 3.2. The higher $R_a$ models tend to have a stronger non-stationary character than low $R_a$ models. In our simulations this effect is stronger for the magnetic field energy when compared to the kinetic energy time series.

For most cases the flow is characterized by a strong azimuthal velocity component. For all cases except case 1C, the toroidal kinetic energy is greater than the magnetic and the kinetic poloidal energies. To show the relative importance of zonal flows, table 3.1 includes a row with the ratio of the time averaged toroidal kinetic energy, $\langle K_t \rangle$, and the time averaged poloidal kinetic energy, $\langle K_p \rangle$. We find that $\langle K_t \rangle / \langle K_p \rangle$ increases with decreasing $P_m$ and becomes quite

Table 3.1: Table with parameters and properties for the simulations studied in this paper. The non-dimensional parameters $R_a$, and the equivalent $R_a/R_{a_c}$, $P_m$, and $E$ are included. The Elsasser number $\Lambda$, the Alfvén number $A$ and the magnetic Reynolds nuber $R_m$, based on mean values of the root mean squared value of the time averaged $\mathbf{u}$ and $\mathbf{B}$. We also include the time averaged energy values, $\langle K_t \rangle$, $\langle K_p \rangle$ and $\langle M_{Tot} \rangle$ which are the kinetic toroidal, kinetic poloidal and total magnetic energies respectively (including also the standard deviation of the time series). We also present the energy of the time averaged magnetic field, $M_{ave}$; and the ratio of the toroidal and poloidal kinetic energies, $\frac{\langle K_t \rangle}{\langle K_p \rangle}$. We calculated a spatially averaged geostrophy index, $[\omega_z^*]$ and the same index for only the region outside, $[\omega_z^*]_{OTC}$, and inside, $[\omega_z^*]_{ITC}$, the tangent cylinder.

| | Case 1A | Case 1 | Case 1B | Case 1C | Case 2A | Case 2 | Case 3A | Case 3 | Case 4 |
|---|---|---|---|---|---|---|---|---|---|
| $R_a$ ($\times10^6$) | 5 | 5 | 5 | 5 | 15 | 15 | 30 | 30 | 11 |
| $R_a/R_{a_c}$ | 11 | 11 | 11 | 11 | 32 | 32 | 65 | 65 | 85 |
| $P_m$ | 0.1 | 0.3 | 1.0 | 5.0 | 0.1 | 0.3 | 0.1 | 0.3 | 0.3 |
| $E$ ($\times10^{-4}$) | 1 | 1 | 1 | 1 | 1 | 1 | 1 | 1 | 3 |
| $\Lambda$ | 0.00 | 0.07 | 0.09 | 1.30 | 0.00 | 0.43 | 0.03 | 0.18 | 0.10 |
| $A$ | 0.00 | 0.31 | 0.40 | 1.10 | 0.00 | 0.32 | 0.07 | 0.19 | 0.08 |
| $R_m$ | 60.46 | 75.20 | 227.96 | 866.55 | 179.61 | 157.08 | 131.53 | 259.93 | 242.71 |
| $\langle K_t \rangle$ ($\times10^6$) | $7.71 \pm 0.55$ | $1.17 \pm 0.08$ | $0.91 \pm 0.06$ | $0.44 \pm 0.04$ | $68.38 \pm 3.44$ | $4.89 \pm 0.69$ | $34.66 \pm 6.16$ | $13.41 \pm 2.10$ | $12.14 \pm 3.86$ |
| $\langle K_p \rangle$ ($\times10^6$) | $0.10 \pm 0.33$ | $0.17 \pm 0.01$ | $0.20 \pm 0.02$ | $0.20 \pm 0.02$ | $0.51 \pm 0.07$ | $0.97 \pm 0.13$ | $2.29 \pm 0.17$ | $2.62 \pm 0.22$ | $1.84 \pm 0.12$ |
| $\langle M_{Tot} \rangle$ ($\times10^6$) | $0.00 \pm 0.00$ | $0.24 \pm 0.03$ | $0.32 \pm 0.07$ | $0.53 \pm 0.03$ | $0.00 \pm 0.00$ | $1.13 \pm 0.18$ | $1.50 \pm 0.44$ | $2.20 \pm 0.35$ | $0.32 \pm 0.23$ |
| $M_{ave}$ ($\times10^6$) | 0.00 | 0.10 | 0.04 | 0.11 | 0.00 | 0.61 | 0.12 | 0.26 | 0.05 |
| $\frac{\langle K_t \rangle}{\langle K_p \rangle}$ | 80.08 | 6.81 | 4.53 | 2.16 | 134.84 | 5.04 | 15.14 | 5.12 | 6.59 |
| $[\omega_z^*]$ | 0.87 | 0.82 | 0.81 | 0.81 | 0.88 | 0.82 | 0.84 | 0.82 | 0.81 |
| $[\omega_z^*]_{OTC}$ | 0.89 | 0.75 | 0.73 | 0.72 | 0.90 | 0.76 | 0.80 | 0.77 | 0.74 |
| $[\omega_z^*]_{ITC}$ | 0.86 | 0.86 | 0.86 | 0.85 | 0.86 | 0.86 | 0.86 | 0.86 | 0.85 |
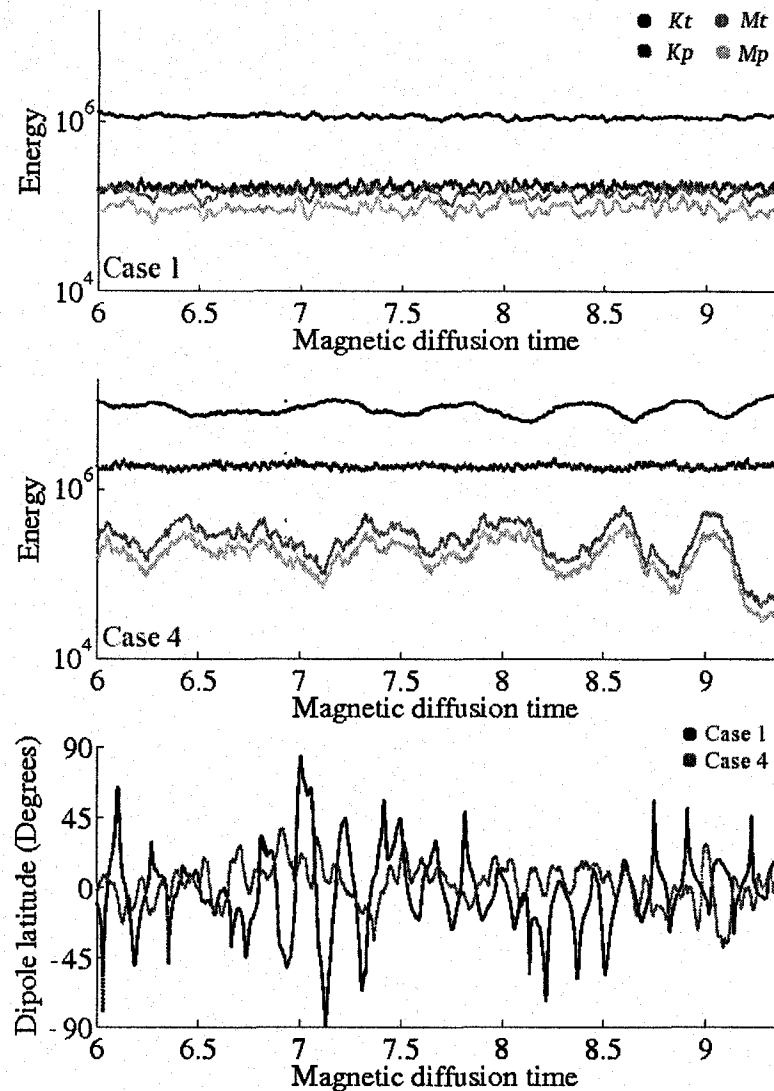
Figure 3.2: Time series of the energy for two values of $R_a$ and for an intermediate value of the magnetic Prandtl number, $P_m = 0.3$. Presented here are the poloidal and toroidal components of the kinetic and magnetic energies ($Kp$, $Kt$, $Mp$ and $Mt$ respectively) for case 1 ($R_a = 11R_{a_c} = 5 \times 10^6$) and case 4 ($R_a = 85R_{a_c} = 11 \times 10^6$). The bottom panel shows the time series of the dipole latitude for both cases.

large when no magnetic field is sustained (see cases 1A and 2A in table 3.1 ).

The strength of the flow is modified not only by $R_a$ (higher driving energy results in faster equatorial flows, e.g. Aubert (2005) ) but also by $P_m$, as shown in figure 3.3(b). The Rossby number is the ratio between inertia and Coriolis forces. For the scaled quantities of the model it can be written as:

$$R_o = \frac{u}{\Omega D} = R_e E,$$ (3.9)

where $R_e$ is the Reynolds number, $R_e = uD/\nu$.

We found the azimuthal flow for all the simulations to be highly axisymmetric. Episodic non-axisymmetric plumes do occur, but are transient, being swept into the strong axisymmetric zonal flow. Taking an azimuthal average of $u_\varphi$ at the outer boundary, the azimuthal Rossby number as a function of latitude is calculated, and shown in figure 3.3(b).

Flows under low $R_a$ and $E$ are strongly affected by rotation and tend to be geostrophic. A strictly geostrophic flow is defined by a balance between the Coriolis force and the pressure gradient. In the case of a rotating spherical shell, geostrophic flow is separated into two regions defined by the tangent cylinder, an imaginary cylinder that has its symmetry axis parallel to the rotation axis, $z$, and is tangent to the rigid inner sphere at the equator. Due to the Proudman-Taylor constraint, and the condition of impermeable boundaries, there is no velocity component parallel to the axis of rotation for geostrophic flow, and flow is inhibited across the tangent cylinder. We find our models to be quasi-geostrophic. Indeed, the azimuthal velocity is very well differentiated by the tangent cylinder surface and the velocity field, which is dominated by the azimuthal component, changes little in the direction of the $z$-axis (see figure 3.3(a)). Outside the tangent cylinder, the velocity field takes the approximate form of differentially rotating cylinders, while inside the tangent cylinder columnar, hot plumes rise from the inner boundary, mostly parallel to $z$ with a relatively small azimuthal velocity. The cylindrical geometry of the flow within the spherical shell gives rise to the characteristic zonal flows at the outer surface plotted in figure 3.3(b). All models result in a prograde zonal jet at the equator.

There are different mechanisms for field generation in dynamo theory. The omega effect, for example, refers to the generation of toroidal magnetic field lines from an existing poloidal magnetic field. The alpha effect refers to production of poloidal magnetic field lines from an existing toroidal field. Once a magnetic field is sustained in the convective region, and due to the non-negligible conductivity of the fluid, the flow tends to modify the magnetic field lines. This results in a Lorentz force opposing the change and modifying the flow, decreasing the velocity of the fluid (Guillot et al. (2004)). Since the strength of the Lorentz force is proportional to the fluid electrical conductivity, it is sensible to find that the Rossby number of the main equatorial jet at the outer boundary decreases with increasing $P_m$ (figure 3.3(b)).

In contrast to the relatively stable energy time series and flow geometry shown in figures 3.2 and 3.3, the symmetry of the resultant magnetic field varies greatly with time. In our calculations

(a)  (b)
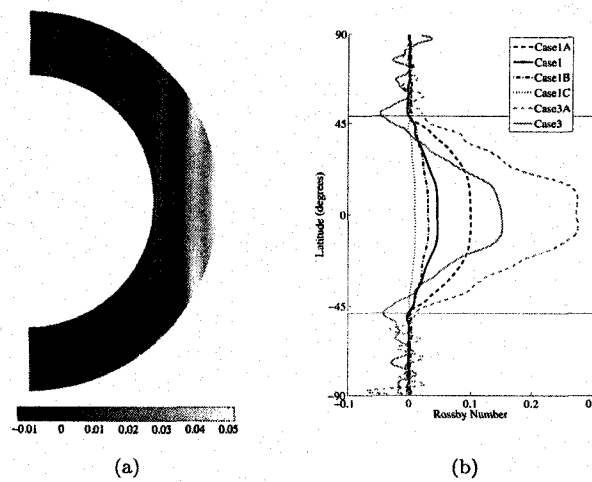
Figure 3.3: Plots of the toroidal Rossby number for a snapshot of the velocity field. On the left, the toroidal velocity $u_\varphi$ is plotted for a snapshot of case 1. On the right, latitude versus azimuthally averaged Rossby number at the outer boundary is plotted for various values of the magnetic Prandtl number and Rayleigh number. Included here models with $P_m = 0.1$ for cases 1A and 3A, $P_m = 0.3$ for cases 1 and 3, $P_m = 1.0$ for case 1B, and $P_m = 5.0$ for case 1C. They also involve two values of the Rayleigh number, $R_a = 11R_{a_c}$ (cases 1A, 1, 1B, and 1C) and $R_a = 65R_{a_c}$ (cases 3A and 3). The horizontal lines mark the projection of the tangent cylinder onto the surface $r = r_o$.

we express the magnetic field as the negative of the gradient of the potential $\phi$,

$$\phi(r,\theta,\varphi) = \sum_{\infty}^{\infty} \sum_{l}^{l} \left(\frac{r_o}{r}\right)^{l+1} P_l^m(\cos(\theta)) \left[g_l^m \cos(m\varphi) + h_l^m \sin(m\varphi)\right], \qquad (3.10)$$

where $r_o$ is the radius at the top of the dynamo region, $P_l^m(x)$ is the Legendre polynomial of degree $l$ and order $m$, and $g_l^m$ and $h_l^m$ are called the Gauss coefficients. The general geometric characteristics of the magnetic field can be determined by a spectral decomposition. The mean-squared field strength can be calculated for different degrees and orders for the resultant magnetic field at the outer boundary. We calculate the spectra by summing the mean-squared field strength for a common degree $l$, and common order $m$, that is (for $l > 0$),

$$a_l(r) = \sum_{m=0}^{l} (l+1) \left(\frac{r_o}{r}\right)^{2l+4} \left[(g_l^m)^2 + (h_l^m)^2\right] \qquad (3.11)$$

and

$$a_m(r) = \sum_{l=1}^{l_{max}} (l+1) \left(\frac{r_o}{r}\right)^{2l+4} \left[(g_l^m)^2 + (h_l^m)^2\right]. \qquad (3.12)$$

To compare our models to the magnetic field measured at the top of the cloud layer of the ice giants, we use upward continuation of the magnetic field in our simulations to a radius $r_e = 1.25\,r_o$. In this paper, we call the surface of the sphere of radius $r_e$ the *equivalent planetary surface*. We compare spectra of randomly picked snapshots with the spectra of the time-averaged fields of the radial magnetic field component, $B_r$, at the equivalent planetary surface. The time averaged field magnitude is weaker when compared with the magnitude at a given snapshot (see $M_{ave}$ and $\langle M_{Tot}\rangle$ table 3.1). The averaged magnetic field geometry is also distinctly different from a snapshot. The non-transient component of the field tends to be more dipolar for higher $R_a$, see figure 3.4(c). The spectra are averaged over approximately one magnetic diffusion time.

To show the time variability of the magnetic field we include the time series of the energy for different spherical harmonic degrees and orders of the magnetic field at the equivalent planetary surface. In figure 3.5 the time series of the energy for the dipolar $(M_{l=1})$, quadrupolar $(M_{l=2})$, and octupolar $(M_{l=3})$, components are shown. In order to describe the azimuthal symmetry as a function of time we separate the field into axisymmetric $(M_{m=0})$, and non-axisymmetric $(M_{m\neq0})$ parts. Using a subset of the total time of the simulation, we calculate the mean and standard deviation to determine the percentage of the variation about the mean, similar to our analysis for the time series in figure 3.2. We find that the ratio of the standard deviation to the mean yield values of $\delta M_{l=1} = 90\%$, $\delta M_{l=2} = 57\%$, and $\delta M_{l=3} = 58\%$ for the top panel time series, for the bottom panel, $\delta M_{m=0} = 97\%$ and $\delta M_{m\neq0} = 85\%$. For the same short period, and as a comparison, we find that the total magnetic energy in the fluid has $\delta M_{Tot} = 24\%$ deviation. For the toroidal kinetic energy $\delta K_t = 5\%$.

For a more direct comparison with the ice giants, we include a map of the radial magnetic field at the top of the clouds. Using the Gauss coefficients for Uranus and Neptune published in Holme & Bloxham (1996), we plot maps of the ice giants' magnetic fields truncated to a
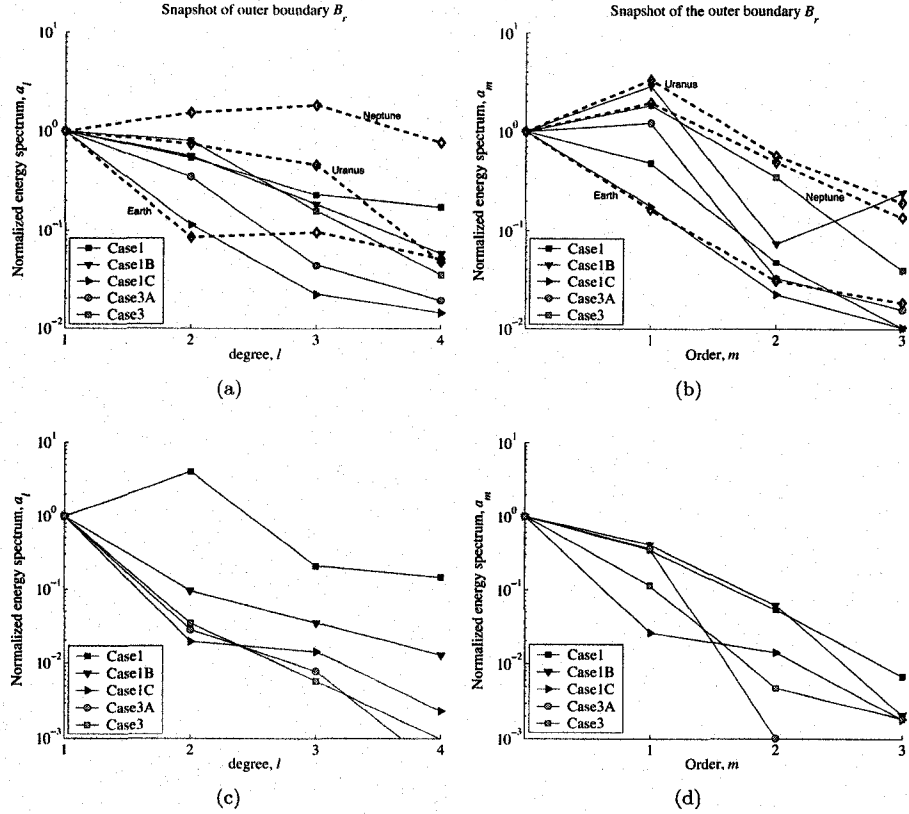
Figure 3.4:   Plots of the spectral power, $a_l$ and $a_m$ of the radial magnetic field, $B_r$, at the equivalent planetary surface ($r_e = 1.25\, r_o$); $r_o$ is the radius at the top of the dynamo. At the top, the spectra of model snapshots are plotted. On these frames, we include the spectra for the radial magnetic field of Earth (IGRF-10), as well as those for Uranus and Neptune at the top of the clouds (from models Umoh and Nmoh in Holme & Bloxham (1996)). At the bottom, the spectra of averaged model magnetic fields are plotted. The average is taken over one magnetic diffusion time. To compare the magnetic field spectra, we plot them all at $1.25\, r_o$. Thus $r_o$ represents the radius of the core-mantle boundary for Earth, the bottom of the deep atmospheres for Uranus and Neptune, and the top of the dynamo for our models.
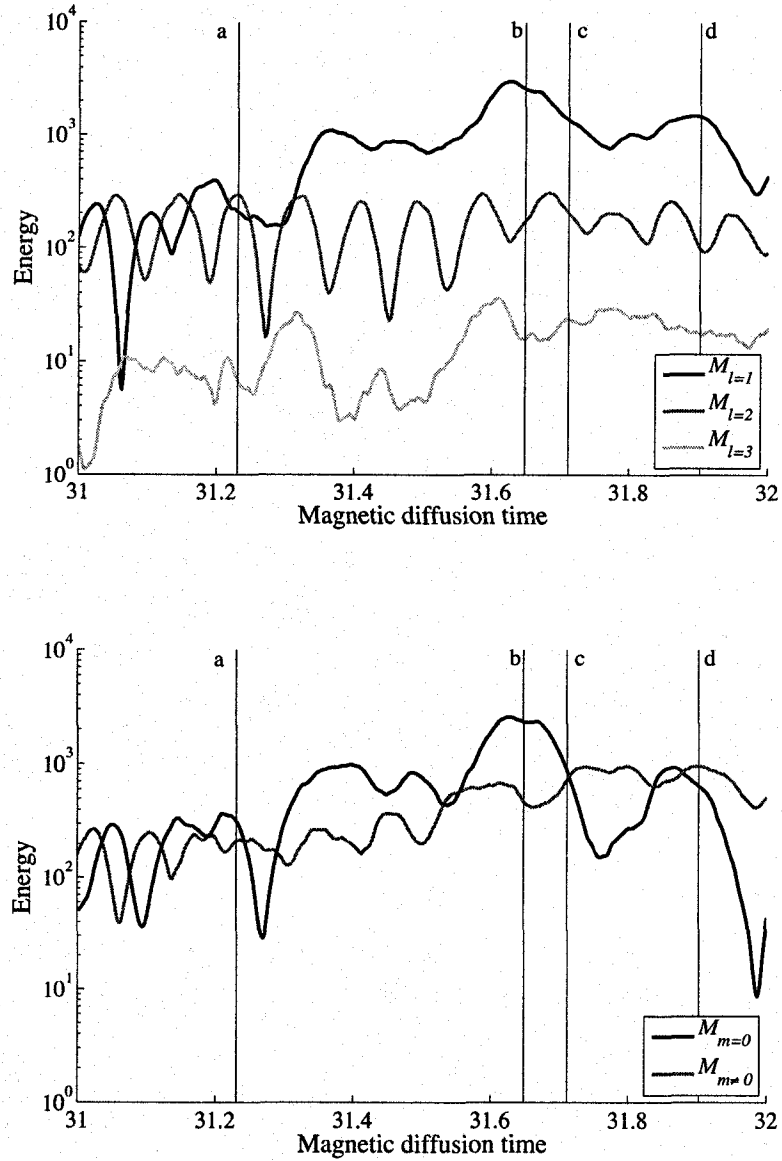
Figure 3.5: Time series of the magnetic energy for case 3A ($R_a = 3 \times 10^7 = 65 R_{a_c}$ and $P_m = 0.1$). The top panel shows the dipolar, quadrupolar, and octupolar components of the magnetic energies ($M_{l=1}$, $M_{l=2}$, and $M_{l=3}$ respectively) at the equivalent planetary surface, $r_e = 1.25\,r_o$. The bottom panel shows the time series of the axisymmetric ($M_{m=0}$), and non-axisymmetric ($M_{m\neq0}$) component of the magnetic field at the equivalent planetary surface.

(a)                                    (b)
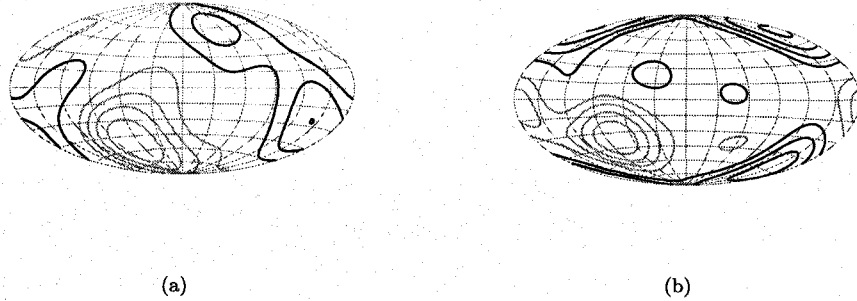
Figure 3.6: Maps of the radial magnetic field of (a) Uranus and (b) Neptune at the top of the clouds. The magnetic field plotted up to degree five based on the Gauss coefficients from Table 2 in Holme & Bloxham (1996).

maximum degree $l_{max} = 5$ (figure 3.6). The radial fields obtained for a numerical simulation (case 3A) projected to the equivalent planetary surface, for four different times (marked in the times series shown in figure 3.5) are included in figure 3.7. As can be seen in the time series (figure 3.5) of our numerical simulation, the relative dominance of dipolar, quadrupolar, and octupolar fields, as well as the relative dominance of axisymmetric and non-axisymmetric fields, varies with time. Thus, for some snapshots in time the model magnetic field resembles those of Uranus and Neptune while at other times they do not. Figure 3.7(a) shows a snapshot when the modelled field is quadrupolar and relatively axisymmetric; in figure 3.7(b) the field is dipolar and mostly axisymmetric; figure 3.7(c) presents a combination of non-axisymmetry and axisymmetric components that are comparable and a dipolar field; and figure 3.7(d) shows a non-axisymmetric field with slightly more dominant quadrupolar and octupolar components with respect to the dipole than in figure 3.7(c). The dipole colatitude found for each frame show a significant deviation from the axis of rotation. Dipole tilts of 61.3°, 19.6°, 40.3°, and 49.4° correspond to panels (a), (b), (c), and (d) of figure 3.7 respectively.

For most of the simulations, the magnetic force is weak compared with the Coriolis force, this is indicated by low values of the Elsasser number, $\Lambda = B^2(\mu\lambda\rho\Omega)^{-1}$, presented in table 3.1. The only case for which $\Lambda > 1$ is case 1C, which has the highest $P_m$. Furthermore, the magnetic field intensity increases with increasing convective vigour and decreases with increasing magnetic diffusivity.

We are interested in the relationship between the geometry and vigour of the flow field and the resultant magnetic field for our models. This relationship may be understood in terms of the ratio of the kinetic and magnetic energies, or in terms of the ratio of the Alfvén wave velocity and the fluid velocity. This ratio, called the Alfvén number, compares the influence of the magnetic field on the flow and vice versa. It can be expressed as:

$$A = \frac{B}{u\sqrt{\rho\mu}} = \sqrt{\frac{\Lambda}{ER_eR_m}}, \qquad (3.13)$$

(a)

(b)

(c)

(d)
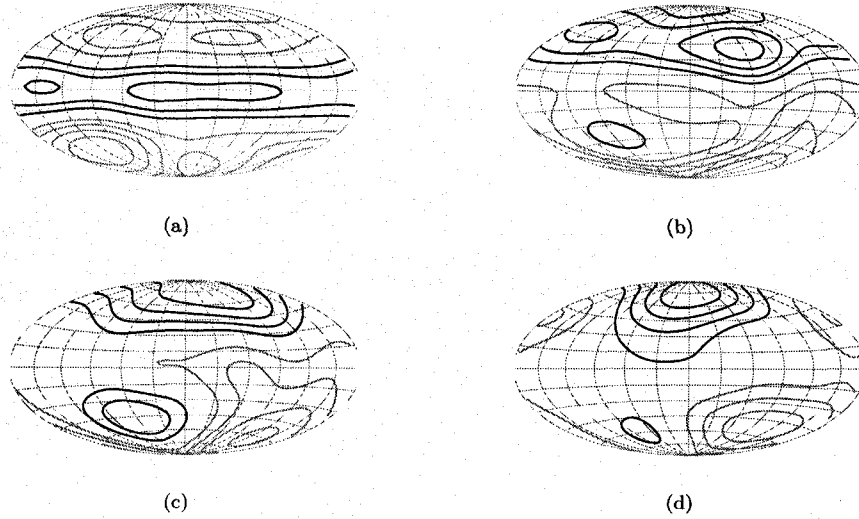
Figure 3.7: Maps of the radial component of the magnetic field for the numerical simulation case 3A, up to spherical harmonic degree five, at the equivalent planetary surface ($r_e = 1.25\,r_o$), for four different instants. The dipole tilt calculated for each frame is significantly far from the axis of rotation, i.e. 61.3°, 19.6°, 40.3°, and 49.4° for (a) (b), (c), and (d) respectively. The time to which the panels correspond are marked by black vertical lines on figure 3.5.

where $R_m = uL/\lambda$ is the magnetic Reynolds number. The Alfvén number in table 3.1 is included to estimate the effect that the magnetic field has on the fluid flow. If $A \ll 1$ the influence of the magnetic field on the fluid flow is small. The values for the magnetic cases range from $A = 0.07$ for $P_m$=0.1 (case 3A) to $A = 1.1$ for the dynamo with $P_m = 5$ (case 1C). With the exception of case 1C, the Alfvén number is less than one but never small enough to indicate that the magnetic field has a negligible effect on the flow field.

To analyse the geostrophic characteristics of our model quantitatively we calculate the $z$ component of the vorticity, $\frac{1}{2}(\nabla \times \mathbf{u})_z$, and normalize it with the magnitude of the total vorticity at that given point to obtain $\omega_z^* = |(\nabla \times \mathbf{u})_z||\nabla \times \mathbf{u}|^{-1}$, which will be called the geostrophy index. If the flow is completely geostrophic, then $\omega_z^* = 1$. Taking an azimuthal average, $[\omega_z^*]$ (where the brackets denote a spatial average), gives an indication of the dominance of the geostrophy as a function of radius and latitude.

Figure 3.8 shows, for the calculations with $E = 10^{-4}$, snapshots of the poloidal streamlines superposed on images of the geostrophy index $[\omega_z^*]$, and the poloidal magnetic field lines superposed on images of the magnitude of the toroidal component of the magnetic field. Increasing $R_a$ changes the distribution of $[\omega_z^*]$ over $(r, \theta)$ space (meridional planes). The fluid is highly geostrophic near the equatorial plane for low $R_a$. When $R_a$ is increased (bottom to top in figure 3.8) radial and poloidal flow is increased close to the internal boundary, due to the stronger convection. The geostrophic flow is then confined to the outer part of the shell, near the equa-
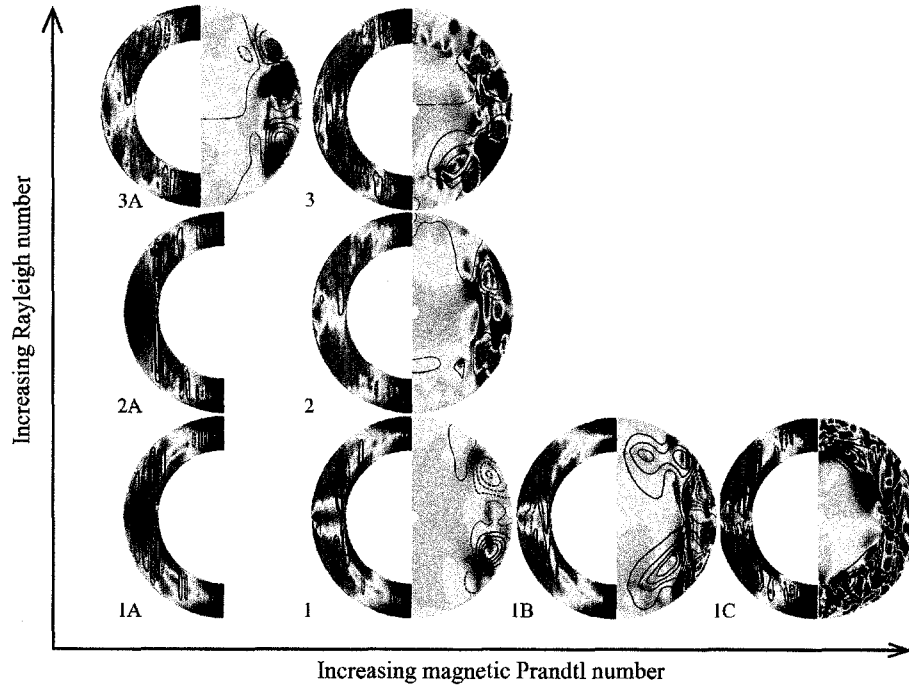
Figure 3.8: Images of the geostrophy index, poloidal streamlines, and poloidal and azimuthal magnetic field for all simulations with $E = 10^{-4}$. For each panel the contour lines on the left side correspond to the meridional streamlines superimposed on the normalized vorticity, $[\omega_z^*]$ (see text). On the right side, the contour lines correspond to the poloidal magnetic field lines superposed to an image of the azimuthal magnetic field $B_\varphi$. The panels are organized with increasing $P_m$ from left to right and and increasing $R_a$ from bottom to top. The colour map used for the geostrophy index varies from 0.5 (blue) to 1 (dark red). In the case of the toroidal magnetic field blue indicates retrograde direction and red prograde.

torial plane. The tangent cylinder is clearly defined by the geostrophy index for low $R_a$ and low $P_m$ (cases 1, 1A and 2A). When $R_a$ is increased the geostrophy index becomes more homogeneous and the tangent cylinder becomes less well defined. For increasing $P_m$ (left to right in figure 3.8), the distribution of the geostrophy index varies principally between the non-dynamo case to the magnetic solutions and does not change significantly between magnetic solutions with $R_a = 5 \times 10^6 = 11 R_{a_c}$. While still having a mostly geostrophic flow near the equatorial plane when increasing $P_m$, the poloidal vorticity becomes more significant with respect to the $z$-vorticity in regions outside the tangent cylinder, above and below the equatorial plane.

The magnetic field within the inner rigid sphere is stronger for higher $P_m$. This is easy to understand since the value for the electrical conductivity is the same for the fluid and the inner sphere, thus a higher $P_m$ means a higher electrical conductivity for the rigid inner sphere. The rigid sphere's magnetic field is more stable in time than the field within the convective fluid. The dipolar field generated inside the tangent cylinder is strengthened by presence of the inner sphere and, as in case 1C, creates a weak background dipolar field upon which the flow-generated transient field is superimposed. In consequence, the time averaged field is dipolar (see figure 3.4) and sustained by the inner sphere, while the instantaneous field varies rapidly over time due to strong fluctuations of the flow-generated magnetic field.

## 3.4 Discussion

Previous numerical models have also produced non-dipolar magnetic fields. Stanley & Bloxham (2006, 2004) presented models with a stratified interior, and compared them with single fluid layer models (like the ones presented here). They studied the effect of different radius ratios in the single-layer models, and found that non-dipolar dynamos are attainable, but only for a limited range of radius ratios. They also pointed out, for these single-layer models, the need for a rigid inner sphere of low electrical conductivity. They concluded that a stratified fluid is more suitable than a single fluid layer when modelling the planetary interior, in order to reproduce the magnetic field geometry of the ice giants. The flows developed in the stratified models of Stanley and Bloxham seem to have low Alfvén numbers, based on a comparison using magnetic and kinetic energy time series for the unstable layer. This would indicate that stratification in the fluid allows the flow within the unstable layer to have a more dominant effect over the magnetic field, and this results in a non-dipolar magnetic field.

The multipolar regime found in our models is consistent with Christensen & Aubert (2006) and Olson & Christensen (2006). They found that models with high Rossby numbers ($R_o \gtrsim 0.02$ for $E = 10^{-4}$) result in highly variable, non-dipolar and non-axisymmetric magnetic fields. Other groups have also found correlations between input parameters, such as $P_m$ and $R_a$, and field geometry. For example, our solutions for high $P_m$ (cases 1B and 1C) may be compared with results of Grote et al. (2000). Although Grote presented only simulations with $R_a$ less than ten times $R_{a_c}$ and had different radius ratio and boundary conditions than our simulations, a comparison is relevant since they analysed the effect of the magnetic diffusivity for various models. They found quadrupolar dynamos for $P_m$ of order 1 and Rayleigh numbers just above

onset of dynamo action. However, increasing in the magnetic Prandtl number led to dominantly dipolar dynamos, even for low $R_a$. For higher $P_m$ values, only dipolar field geometries were found. In agreement with their study, we find that the increase in the magnetic Prandtl number favours the dipolar component, relative to the higher multipoles, in the time averaged solution.

Our models differ from previous models in that we use low magnetic Prandtl numbers (i.e. high magnetic diffusivity), along with free slip outer boundary conditions, which allows strong differentially rotating zonal flows, driven by Reynolds stress, to develop before Lorentz forces set in to balance the torques. In our simulations, the quadrupole component is favoured by zonal flows. The quadrupolar character of the magnetic field may be determined by the strength of the azimuthal flow. We describe in section 3.3 how the distribution of the geostrophy index varies depending on $R_a$ and $P_m$. Notice that the $[\omega_z^*]$ distribution (image on the left side of each panel in figure 3.8) indicates that the high geostrophy index is associated with a lack of poloidal magnetic field lines. Near the equatorial plane, the omega effect is favoured due to the dominance of differential toroidal flow. When this dominance is diminished (for higher $P_m$ or $R_a$), the poloidal magnetic field lines are present and the field becomes less quadrupolar, and more dipolar. For our models dominated by strong zonal flow (which excludes the case with $P_m = 5$), the Alfvén number is always below 1 but increases with $P_m$. For lower values of $A$, the magnetic field has stronger quadrupolar and octupolar components, relative to the dipolar component. Thus, zonal flows are weakly affected by the magnetic field, resulting in low Elsasser numbers and non-dipolar fields, similar to the magnetic fields of the ice giants. In the models presented here, stronger magnetic fields inhibit the zonal flows (see figures 3.3(b) and 3.8). For the case with high electrical conductivity ($P_m = 5$, case 1C), the magnetic field interferes with the flow to a point where $A > 1$ and the dipolar field dominates.

It has been proposed that the force balance for planetary dynamos is primarily magnetostrophic, which is likely to hold for planets like the Earth, Jupiter and Saturn (e.g. Starchenko & Jones (2002)). For the ice giants, a deviation from this balance could be the reason for their uncommon magnetic field symmetry (Holme & Bloxham (1996)). For our models with high magnetic diffusivities, geostrophic flows generate relatively weak (low Elsasser number) non-dipolar and non-axisymmetric magnetic fields. Thus our models imply that the magnetic fields of the Uranus and Neptune can be sustained by dynamos in which relatively low electrical conductivity of the electrolytic fluid results in a geostrophic (rather than magnetostrophic) balance.

In summary, we have investigated dynamos for a range of magnetic diffusivities and convective forcing with a free slip outer boundary condition. We find that models with high magnetic diffusivity (low $P_m$) develop strong axisymmetric zonal flows resulting in time variable and typically non-dipolar and non-axisymmetric magnetic fields. These dynamos are characterized by strongly inertial flow (high $Ro$) and relatively weak magnetic fields (low $\Lambda$ and $A$). Thus we propose that zonal flow dynamos may explain the magnetic field generation in the ice giants. The electrolyte layers inside Uranus and Neptune are expected to have low electrical conductivity, resulting in $P_m$ values that are much lower than those in the liquid metal cores of the terrestrial planets and gas giants, and orders of magnitude lower than most simulations have undertaken. Since $P_m$ seems to have a strong influence on the geometry of both the flow field and the magnetic

field, we look to future models with even lower $P_m$ to obtain magnetic fields sustained by strong zonal flows with lower Alfvén numbers. One of the major problems in proving the validity of the numerical models is the limited amount of real measurements. We will look to data from future space missions to better understand the geometry and time dependence of magnetic fields in the ice giants.

## 3.5 Acknowledgements

# Chapter 4

# Radially variable electrical conductivity

## 4.1 Introduction

Equations of motion that describe dynamical systems in planetary interiors determine typical length scales for the variation of the velocity, magnetic and temperature fields. Numerical models are restricted to a range of parameters where the length scales between these three fields are comparable. The problem with low viscosity fluids is that the velocity field may present small scale dynamics, when compared with the magnetic field. To solve this problem, a small grid is required for resolving the velocity field. The grid must also extend over a great volume to resolve the large scale field. The dynamo problem, then, is intrinsically demanding due to the physical properties of the fluid itself. In order to overcome this fundamental difficulty, the physical equations used to model planetary interiors have been simplified, in order to write numerical solutions that contemporary technology can solve. Thanks to increasing computer capability, and the development of efficient numerical algorithms, fully three dimensional solutions of self-sustained dynamos have been attained (e.g. Glatzmaier (1984), Kuang & Bloxham (1999), Christensen et al. (1998)). For example, when modelling the geodynamo, a common assumption is to use a spatially and temporally constant density. At Earth's core pressure and temperature, liquid iron is not expected to change density significantly. Thus, a constant density assumption is sensible for terrestrial planets where the dynamo region is expected to be homogeneous in density with only a sharp phase change at the interface between inner and outer cores (Dziewonski & Anderson (1981)). Arguments against the homogeneity of the fluid core have been discussed in the literature (see Braginsky (1999) and references therein). The solidification of the inner core differentiate lighter elements. The crystallization has a preference for the heavier elements (i.e. iron and nickel), leaving lighter-element-enriched fluid that, by buoyancy, reach the core-mantle boundary. It is possible that this lighter-element fluid creates a stably stratified envelope surrounding the core near the CMB. The density variation within the fluid core, even with the

light element layer, would be too small to be visible using seismology. Despite the possibility of a multi-component fluid core, in early studies, numerical simulations of the Earth's core neglect the density variation using the Boussinesq approximation (e.g. Glatzmaier & Roberts (1995), Wicht (2002), Kuang & Bloxham (1999), Christensen et al. (1998)). Compositional convection has been included in Boussinesq models (e.g. Kutzner & Christensen (2004)), with the introduction of a 'co-density' that depends on the chemical density contrast and the temperature. These models still neglect the change in density viscous force (see appendix A). More recently, the change in density has been taken into account using the anelastic approximation, where various models have been proposed, and of which some have been tested ( Glatzmaier & Roberts (1996), Evonuk & Glatzmaier (2004), Jones (2007)).

While homogeneity is a relatively good assumption for iron cores in terrestrial planets, the interiors of the giant planets are not homogeneous in density. The phase transitions occurring within the giant planets are poorly understood. Various theories for the behaviour of liquids at high pressures and temperatures have been studied, and simplified models (with great uncertainties) have been found (Guillot (1999b), Nellis (2000), Stevenson (1982), Podolak et al. (2000)).

In the case of Uranus and Neptune, as has been discussed in chapter 3, the dynamo region is restricted to a zone where water, methane, and ammonia form an electrolyte solution. It is expected that this solution has a relatively homogeneous density; hence, the Boussinesq approximation is valid (Gómez-Pérez & Heimpel (2007)).

For the gas giants, the helium differentiation with depth, and the gradual change from atomic to metallic hydrogen (as suggested by Nellis (2006)) indicate that gas giants interiors undergo a slow density change from the non-conductive atmosphere, to an electrically conductive interior. For Jupiter and Saturn, a homogeneous density for the dynamo region is likely to be a poor approximation.

### 4.1.1   Boussinesq and anelastic approximations

In this section, we include a brief discussion on the most common approximations used for the conservation of mass equation. For a reference on the relevance of the mass conservation equation on the dynamo problem, and where the approximation may be included, please refer to appendix A. The equation of conservation of mass for a fluid is defined by

$$\frac{\partial \rho}{\partial t} = \nabla \cdot (\rho \mathbf{u}), \tag{4.1}$$

where $\rho$ is the density of the fluid, $t$ is time, and $\mathbf{u}$ is the velocity of the fluid. In the case where the velocity of the fluid is much smaller than the speed of sound in the fluid, one can assume that $\partial \rho / \partial t \sim 0$, thus finding what is called the *anelastic approximation*,

$$\nabla \cdot (\rho \mathbf{u}) = 0. \tag{4.2}$$

Further, for a special case where the fluid is well mixed (and the density is homogeneous), $\nabla \rho \sim 0$. This is the *Boussinesq approximation*,

$$\nabla \cdot \mathbf{u} = 0. \tag{4.3}$$

The differences between these last two approximations become relevant for compressible fluids. Consider a system that is heated at its base, and where gravity is aligned with the negative vertical direction. Under a gradient of density (for which the anelastic approximation is necessary), rising plumes will expand with height as the pressure diminishes towards the surface. In the same way, sinking cold plumes will contract with increasing depth. Thus, hot plumes have a greater effect at mixing the fluid than sinking cold plumes. Numerical simulations show how this intuitive understanding may be qualitatively described. Rogers et al. (2003) presented two-dimensional computer simulations of turbulent convection comparing both, the Boussinesq and the anelastic, approximations. Plots of the entropy profile for two of their simulations with exactly the same parameters except for their density profile are presented in figure 4.1, showing the two different solutions due to the density stratification.
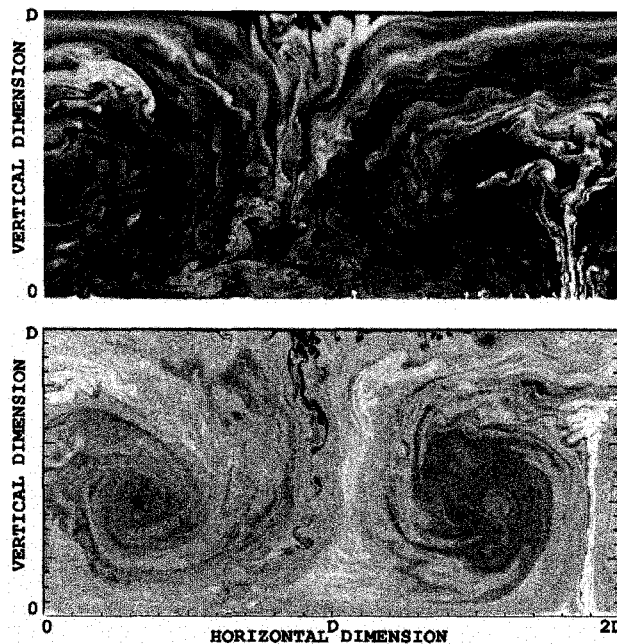


Figure 4.1: Figures taken from Rogers et al. (2003). A fluid heated from the bottom with gravity pointing downwards, $R_a = 10^{11}$, and $P_m = 1$. On top, a snapshot of the entropy perturbation for an anelastic model with decreasing density from bottom to top (the density changes by a factor of 12). On the bottom, the same model parameters as on top, but for a Boussinesq model.

In the top panel of figure 4.1, the density changes from the base to the top by a factor of approximately 12. The changes in the small scale features are clear. The hot plume on the right side (at approximately $x = 1.9D$, where $D$ is the total height of the simulated volume) reaches

a greater height for the Boussinesq case when compared to the anelastic case. The expansion of the fluid in the anelastic approximation diffuses the hot plume by the time it reaches a height of approximately $D/2$, while the plume reaches $0.75D$ for the Boussinesq case. The large scale dynamics for both approximations are similar, i.e. the length scale of the convection cells for both is the same.

Magnetic rotating convective fluids may add further complications to anelastic systems. Evonuk & Glatzmaier (2004) studied two-dimensional models, similar to those discussed above but for rotating convective systems under the additional influence of Lorentz forces. We include here: I) The density profile used for the anelastic models of Rogers et al. (2003) and Evonuk & Glatzmaier (2004) (figure 4.2(a)). II) The snapshot of an entropy profile from Rogers et al. (2003) anelastic models (figure 4.2(b)). Maps of the entropy profile from: III) a non-rotating non-magnetic anelastic solution (figure 4.2(c)) and IV) a magnetic, rotating, anelastic solutions (figure 4.2(d)) presented by Evonuk & Glatzmaier (2004).
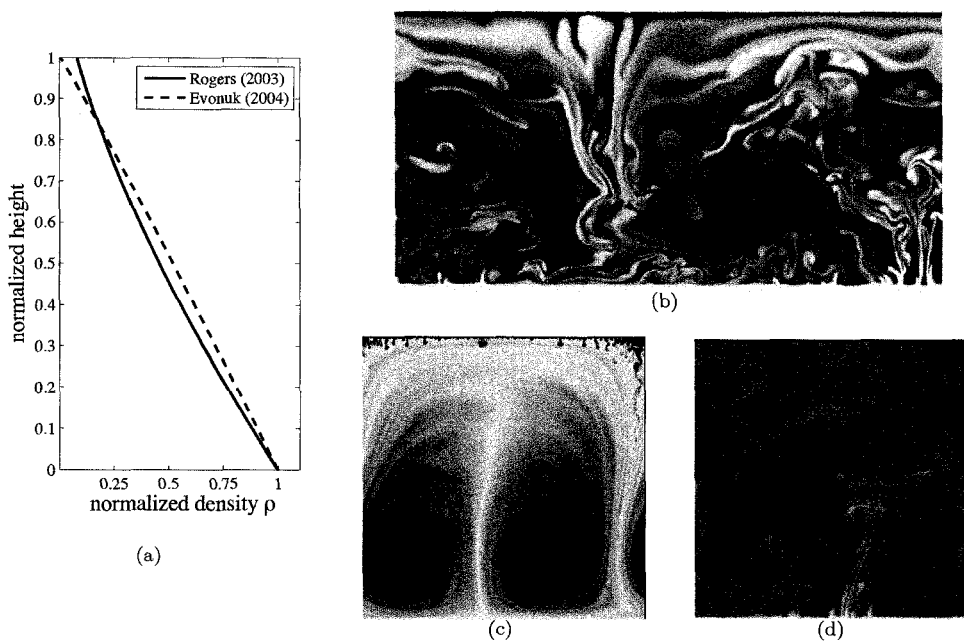


Figure 4.2: Figures taken from Rogers et al. (2003) (b), and Evonuk & Glatzmaier (2004) (c) and (d). The models presented here used the same Rayleigh ($R_a = 10^{10}$) and Prandtl ($P_r = 1$) numbers. Density profiles for the simulations are plotted in (a). In (b), same as the top on figure 4.1 but for a lower $R_a$. On the bottom, (c) and (d), a slightly different anelastic model with a more dramatic density stratification for: (c) a non-magnetic, non-rotating, anelastic simulation; and (d), a rapidly rotating ($E = 10^{-5}$), magnetic ($P_m = 1$), anelastic model.

A direct comparison between Boussinesq and anelastic solutions presented in Evonuk's paper highlights the differences between the two approximations. One of the drawbacks for applying

their results directly to planetary interiors is that the effects of the geometry of the boundary conditions are neglected. They have been proven to have a significant effect on the flow (e.g. Heimpel et al. (2005b)), and are not considered by Evonuk & Glatzmaier (2004). Busse (2002) presented a mathematical approach as well as numerical results on the effect of the geometric constrain on the flow in a cylinder and in spherical shells. He attributed the differential rotation on a rotating cylindrical annulus to a mean flow instability introduced by the geometry of the top and bottom geometrical boundaries. This results in a mean zonal shear due to the Reynolds stress $R_{r\varphi}$. To study the effects of density variation in planetary systems requires the inclusion of three-dimensional geometric constraints.

The anelastic approximation has been used in three dimensional systems in order to model stellar dynamos, e.g. Brun et al. (2005). Even though they do not present a direct comparison between anelastic and Boussinesq models, their results for stress free boundaries have similar features for the velocity field as the Boussinesq models presented in chapter 3. A direct comparison between these two approximations is still desirable.

It is expected that density inside the giant planets decreases gradually outward with radius, as does the electrical conductivity (Nellis (2006)). The molecular hydrogen envelope, although not electrically conductive, may also present significant variations in density. The compressibility of liquid hydrogen is significant, and it is relevant to take into account the density stratification and the electrical conductivity variation when modelling the gas giants' dynamos.

We propose to analyse the sole effect of a radially variable electrical conductivity. For this, we use as a base a numerical code (Magic 3.1 Wicht (2002)) that features the Boussinesq approximation, and does not include variable electrical conductivity. A mathematical description of the modified numerical approach is included in Section 4.2. In Section 4.3, we present two tests based on seven numerical simulations as a way of introducing and evaluating the modifications to the numerical code. Lastly, in Section 4.4 we discuss the results found based on the preliminary tests.

## 4.2 Radially variable conductivity equations

Using equation A.47, derived from Maxwell's equations, the time derivative of the magnetic induction vector is:

$$\frac{\partial \mathbf{B}}{\partial t} = -\nabla \times \lambda(\nabla \times \mathbf{B}) + \nabla \times (\mathbf{u} \times \mathbf{B}). \tag{4.4}$$

Since $\nabla \cdot \mathbf{B} = 0$, dynamo models solve equation 4.4 using the poloidal and toroidal potentials (Chandrasekhar (1961)). The magnetic induction vector can be written as a function of two scalar fields

$$\mathbf{B} = \nabla \times \nabla \times b\hat{\mathbf{r}} + \nabla \times j\hat{\mathbf{r}}, \tag{4.5}$$

where $b$ is the poloidal potential and $j$ the toroidal potential. We can find a relation between $b$ and $\mathbf{B}$:

$$\hat{\mathbf{r}} \cdot \mathbf{B} = \hat{\mathbf{r}} \cdot [\nabla \times \nabla \times \hat{\mathbf{r}}b + \nabla \times \hat{\mathbf{r}}j],$$

$$
\begin{aligned}
&= \hat{\mathbf{r}}[\nabla(\nabla \cdot \hat{\mathbf{r}})b - \nabla^2 b\hat{\mathbf{r}}], \\
&= \nabla_r^2 b - \nabla^2 b \\
\hat{\mathbf{r}} \cdot \mathbf{B} &= -\nabla_H^2 b,
\end{aligned}
\tag{4.6}
$$

where the Laplacian is written as $\nabla^2 = \nabla_r^2 + \nabla_H^2$ in terms of the radial, $\nabla_r^2$, and the horizontal, $\nabla_H^2$, components. For future reference, we introduce here the angular momentum operator $L_H = -r^2 \nabla_H$.

Similarly, the relation between $j$ and $\mathbf{B}$ can be found,

$$
\begin{aligned}
\hat{\mathbf{r}} \cdot (\nabla \times \mathbf{B}) &= \hat{\mathbf{r}} \cdot [\nabla \times \nabla \times \nabla \times \hat{\mathbf{r}}b + \nabla \times \nabla \times \hat{\mathbf{r}}j] \\
&= \hat{\mathbf{r}} \cdot (\nabla \times [\nabla(\nabla \cdot \hat{\mathbf{r}}) - \nabla^2 \hat{\mathbf{r}}])b - \nabla_H^2 j \\
&= \hat{\mathbf{r}} \cdot (\nabla \times [\nabla_r^2 \hat{\mathbf{r}} - \nabla^2 \hat{\mathbf{r}}])b - \nabla_H^2 j \\
&= \hat{\mathbf{r}} \cdot (\nabla \times [\nabla_H^2]\hat{\mathbf{r}})b - \nabla_H^2 j \\
\hat{\mathbf{r}} \cdot (\nabla \times \mathbf{B}) &= -\nabla_H^2 j.
\end{aligned}
\tag{4.7}
$$

To find the how the radial component of the magnetic induction vector changes with time, we can take the dot product of equation 4.4 with $\hat{\mathbf{r}}$

$$
\frac{\partial \mathbf{B}}{\partial t} \cdot \hat{\mathbf{r}} = [\nabla \times (\mathbf{u} \times \mathbf{B}) - \nabla \times \lambda(\nabla \times \mathbf{B})] \cdot \hat{\mathbf{r}}.
\tag{4.8}
$$

The second term on the right hand side of this equation may be simplified, since we assume an exclusively radial change in diffusivity and thus $\nabla \lambda$ has only the radial component,

$$
\begin{aligned}
[\nabla \times \lambda(\nabla \times \mathbf{B})] \cdot \hat{\mathbf{r}} &= (\nabla \lambda \times (\nabla \times \mathbf{B})) \cdot \hat{\mathbf{r}} - \lambda \nabla^2 \mathbf{B} \cdot \hat{\mathbf{r}} \\
&= -\lambda \hat{\mathbf{r}} \cdot (\nabla^2 \mathbf{B}).
\end{aligned}
\tag{4.9}
$$

thus,

$$
\frac{\partial \mathbf{B}}{\partial t} \cdot \hat{\mathbf{r}} = \nabla \times (\mathbf{u} \times \mathbf{B}) + \lambda \hat{\mathbf{r}} \cdot (\nabla^2 \mathbf{B}).
\tag{4.10}
$$

The second term on the right hand side of equation 4.10 may be developed further. For a vector $\mathbf{a}$ , the radial component of the vectorial Laplacian is:

$$
\begin{aligned}
[\nabla^2 \mathbf{a}] \cdot \hat{\mathbf{r}} &= \nabla^2 a_r - \frac{2a_r}{r^2} - \frac{2}{r^2 \sin\theta} \frac{\partial(a_\theta \sin\theta)}{\partial\theta} - \frac{2}{r^2 \sin\theta} \frac{\partial a_\phi}{\partial r} \\
&= \nabla^2 a_r - \frac{2a_r}{r^2} + \frac{2}{r}\left[\frac{-1}{r\sin\theta}\left(\frac{\partial(a_\theta \sin\theta)}{\partial\theta} + \frac{\partial a_\phi}{\partial r}\right)\right].
\end{aligned}
\tag{4.11}
$$

Since the divergence of the magnetic diffusion vector vanishes,

$$
\nabla \cdot \mathbf{B} = 0 = \frac{1}{r^2}\frac{\partial(r^2 B_r)}{\partial r} + \frac{1}{r\sin\theta}\left[\frac{\partial(\sin\theta B_r)}{\partial\theta} + \frac{\partial B_\varphi}{\partial\varphi}\right]
$$

$$\frac{-1}{r\sin\theta}\left[\frac{\partial(\sin\theta B_r)}{\partial\theta}+\frac{\partial B_\varphi}{\partial\varphi}\right] = \frac{2B_r}{r}+\frac{\partial B_r}{\partial r}.$$ (4.12)

The third term in equation 4.11, when written for $\mathbf{B}=\mathbf{a}$, can be replaced, in the case of the magnetic induction, using the right hand side of equation 4.12. Hence,

$$
\begin{aligned}
\mathbf{r}\cdot(\nabla^2\mathbf{B}) &= \nabla^2 B_r - \frac{2B_r}{r^2}+\frac{4B_r}{r^2}+\frac{2}{r}\frac{\partial B_r}{\partial r}\\
&= \nabla^2\frac{L_H}{r^2}b - \frac{2L_H}{r^4}b - \frac{2}{r}\nabla_H^2\frac{\partial b}{\partial r}\\
&= \left[\nabla_r^2\frac{L_H}{r^2}+\nabla_H^2\frac{L_H}{r^2}-\frac{2L_H}{r^4}+\frac{2L_H}{r^3}\frac{\partial}{\partial r}\right]b\\
&= \left[\frac{1}{r^2}\frac{\partial}{\partial r}\left(r^2\frac{\partial}{\partial r}\frac{L_H}{r^2}\right)+\nabla_H^2\frac{L_H}{r^2}-\frac{2L_H}{r^4}+\frac{2L_H}{r^3}\frac{\partial}{\partial r}\right]b\\
&= \frac{L_H}{r^2}\left[\frac{\partial^2}{\partial r^2}-\frac{L_H}{r^2}\right]b.
\end{aligned}
$$ (4.13)

Substituting equations 4.6 on the left hand side and 4.13 on the right hand side of equation 4.10, gives

$$\frac{L_H}{r^2}\frac{\partial b}{\partial t} = \nabla\times(\mathbf{u}\times\mathbf{B})\cdot\hat{\mathbf{r}}+\lambda\frac{L_H}{r^2}\left[\frac{\partial^2}{\partial r^2}-\frac{L_H}{r^2}\right]b.$$ (4.14)

To find an equation for the time variation of $j$, equation 4.4 may be multiplied by $\hat{\mathbf{r}}\cdot\nabla\times$ (see equation 4.7),

$$\hat{\mathbf{r}}\cdot\nabla\times\frac{\partial\mathbf{B}}{\partial t} = \hat{\mathbf{r}}\cdot\nabla\times\left[-\nabla\times\lambda(\nabla\times\mathbf{B})+\nabla\times(\mathbf{u}\times\mathbf{B})\right].$$ (4.15)

Developing the first term on the right hand side of equation 4.15:

$$
\begin{aligned}
\hat{\mathbf{r}}\cdot\nabla\times[-\nabla\times\lambda(\nabla\times\mathbf{B})] &= -\hat{\mathbf{r}}\cdot\nabla\times[\nabla\lambda\times(\nabla\times\mathbf{B})+\lambda\nabla\times(\nabla\times\mathbf{B})]\\
&= -\hat{\mathbf{r}}\cdot[\nabla\times\nabla\lambda\times(\nabla\times\mathbf{B})+\nabla\lambda\times\nabla\times(\nabla\times\mathbf{B})\\
&\quad +\lambda\nabla\times\nabla\times(\nabla\times\mathbf{B})]\\
&= -\hat{\mathbf{r}}\cdot[\nabla\times\nabla\lambda\times(\nabla\times\mathbf{B})+\lambda\nabla\times\nabla\times(\nabla\times\mathbf{B})].
\end{aligned}
$$ (4.16)

To solve separately both terms on the right hand side of equation 4.16, one can develop further the vectorial expressions. The first term:

$$
\begin{aligned}
\hat{\mathbf{r}}\cdot[\nabla\times[(\nabla\lambda)\times(\nabla\times\mathbf{B})]] &= \hat{\mathbf{r}}\cdot[((\nabla\times\mathbf{B})\cdot\nabla)\nabla\lambda-(\nabla\lambda\cdot\nabla)(\nabla\times\mathbf{B})\\
&\quad +\nabla\lambda(\nabla\cdot(\nabla\times\mathbf{B}))-(\nabla\times\mathbf{B})(\nabla\cdot\nabla\lambda)]\\
&= \hat{\mathbf{r}}\cdot[(\nabla\times\mathbf{B})_r\nabla_r\nabla_r\lambda\hat{\mathbf{r}}-(\nabla\lambda\cdot\nabla)(\nabla\times\mathbf{B})-(\nabla\times\mathbf{B})(\nabla^2\lambda)]\\
&= \hat{\mathbf{r}}\cdot[(-\nabla\times\mathbf{B})_H\nabla^2\lambda-(\nabla\lambda\cdot\nabla)(\nabla\times\mathbf{B})]\\
&= -\hat{\mathbf{r}}\cdot(\nabla\lambda\cdot\nabla)(\nabla\times\mathbf{B})_r.
\end{aligned}
$$ (4.17)

The new term can be written in terms of the potentials (note that $\nabla\lambda$ has only a radial component),

$$
\begin{aligned}
(\nabla\lambda \cdot \nabla)\hat{\mathbf{r}} \cdot (\nabla \times \mathbf{B})_r &= \nabla\lambda \cdot \nabla \frac{L_H}{r^2} j \\
&= \nabla_r \lambda L_H \frac{1}{r^2} \frac{\partial}{\partial r}\left(r^2 \frac{j}{r^2}\right) \\
&= \nabla_r \lambda \frac{L_H}{r^2} \frac{\partial j}{\partial r}.
\end{aligned}
\tag{4.18}
$$

Now, for the second term in equation 4.16,

$$
\begin{aligned}
\lambda\hat{\mathbf{r}} \cdot (\nabla \times \nabla \times (\nabla \times \mathbf{B})) &= \lambda\hat{\mathbf{r}} \cdot \left(\nabla(\nabla \cdot (\nabla \times \mathbf{B})) - \nabla^2(\nabla \times \mathbf{B})\right) \\
&= -\lambda\hat{\mathbf{r}} \cdot \nabla^2(\nabla \times \mathbf{B}),
\end{aligned}
\tag{4.19}
$$

which is the same expression found for equation 4.9, but for $(\nabla \times \mathbf{B})$ instead of $\mathbf{B}$. The radial component $(\nabla \times \mathbf{B})_r$ can be expressed in terms of the toroidal potential $j$,

$$
\lambda\hat{\mathbf{r}} \cdot (\nabla \times \nabla \times (\nabla \times \mathbf{B})) = -\lambda\frac{L_H}{r^2}\left[\frac{\partial^2}{\partial r^2} - \frac{L_H}{r^2}\right] j.
\tag{4.20}
$$

Thus, the diffusion term of the magnetic induction vector can be expressed in terms of the poloidal and toroidal potentials,

$$
\frac{L_H}{r^2}\frac{\partial b}{\partial t} = \hat{\mathbf{r}} \cdot (\nabla \times (\mathbf{u} \times \mathbf{B})) + \lambda\frac{L_H}{r^2}\left[\frac{\partial^2}{\partial r^2} - \frac{L_H}{r^2}\right] b
\tag{4.21}
$$

$$
\frac{L_H}{r^2}\frac{\partial j}{\partial t} = \hat{\mathbf{r}} \cdot \nabla \times (\nabla \times (\mathbf{u} \times \mathbf{B})) + \lambda\frac{L_H}{r^2}\left[\frac{\partial^2}{\partial r^2} - \frac{L_H}{r^2}\right] j + \nabla_r\lambda\frac{L_H}{r^2}\frac{\partial j}{\partial r}
\tag{4.22}
$$

As shown in equations 4.21 and 4.22, the only term that depends on the change of the magnetic diffusivity, $\lambda$, is the third term in equation 4.22. This one needs to be included in the numerical solution in order to allow for the variable conductivity to be accounted for consistently in the dynamics of the system.

## 4.3 Numerical test

### 4.3.1 Electrical conductivity function

To study the effects of variable conductivity in a Boussinesq fluid, we define the electrical conductivity function. For our simple model where the change in the electrical conductivity, $\sigma$, is only a function of radius, we choose a function of the radius based on three main parameters:

$r_m$, $\sigma^*$, and $\alpha$. $\sigma$ is chosen to be a piece-wise function defined by:

$$\sigma(r) = \begin{cases} 1 + (\sigma^* - 1)\left(\frac{r-r_i}{r_o-r_i}\right)^\alpha & , \quad r \le r_m \\ \alpha \exp\left(\frac{k}{\sigma^*}(r - r_o)\right) & , \quad r > r_m \end{cases} , \qquad (4.23)$$

where $k = \alpha(\sigma^* - 1)(r_o - r_i)^{-1}$. $r_m$ determines the volume (the radius of the sphere) were the electrical conductivity is non-negligible, $\alpha$ determines how fast the exponential function decreases outside the conductive volume, and $\sigma^*$ is chosen to be the value of the normalized conductivity where the functions match, $\sigma(r_m) = \sigma^*$. Determining the value of these three parameters defines the electrical conductivity as function of space in the simulated sphere.

## 4.3.2 Methodology

We use various simulations to find the effect of a low electrical conductivity layer surrounding a convective dynamo. As a comparison with previous models we choose non-dimensional parameters comparable to those presented in the literature (Heimpel et al. (2005a), Al-Shamali et al. (2004), see also chapter 2). The Ekman number used is $E = 3 \times 10^{-4}$, the Prandtl number $P_r = 1$, and the magnetic Prandtl number (used for normalizing) $P_m = 5$. The boundary conditions are non-slip for both, inner and outer boundaries, and the radius ratio is $\chi = 0.35$. The simulations do not use hyperdiffusivities. For the first test, we use a relatively low Rayleigh number $R_a = 6 \times 10^5 \approx 2.8R_{a_c}$ that is comparable with the simulation with $\chi = 0.35$ presented in Heimpel et al. (2005a). The second test uses a more vigorous convection, $R_a = 4.8 \times 10^6 \approx 22.9R_{a_c}$, to allow for the dynamo action to be sustained in a smaller electrically conductive volume.

### Constant versus variable electrical conductivity.

The first test presented here is a comparison between a constant conductivity model, called from now on: *control*, and a case with a low conductivity at a thin outer shell where $r_m = 0.9r_0$. We refer to $r_m = 0.9r_o$ as $\chi_m = r_m/r_o = 0.9$. Two similar simulations with a lower value of $r_m$ are found not to be able to sustain a dynamo, these are $\chi_m = 0.8$ and $\chi_m = 0.7$.

The function of variable conductivity is defined by $r_m = \chi_m r_o = 0.9r_o$, $\alpha = 10$ and $\sigma^* = 0.5$, see curves marked as control and $\chi_m = 0.9$ in figure 4.3

The simulations present stable total kinetic and magnetic energies time series shortly after they start. After two magnetic diffusion times the two simulations (control and $\chi_m = 0.9$) present clear differences as a result of the change in the electrical conductivity profile. The time averaged kinetic and magnetic energies are distinctly different for both cases, see the grey rows in table 4.1.

Even though the kinetic energy mean is similar for both time series, for the control case, the deviation from this mean, $\delta_{E_k} = 0.2\%$, is significantly higher than in the variable conductivity case, $\delta_{E_k} = 0.01\%$. The same is true, but less dramatic, for the deviation from the magnetic energy mean, $\delta_{E_m} = 0.9$ and $\delta_{E_m} = 0.1$ for control and $\chi_m = 0.9$ respectively. It is interesting to note that the total kinetic energy is higher than the magnetic energy for the control case while
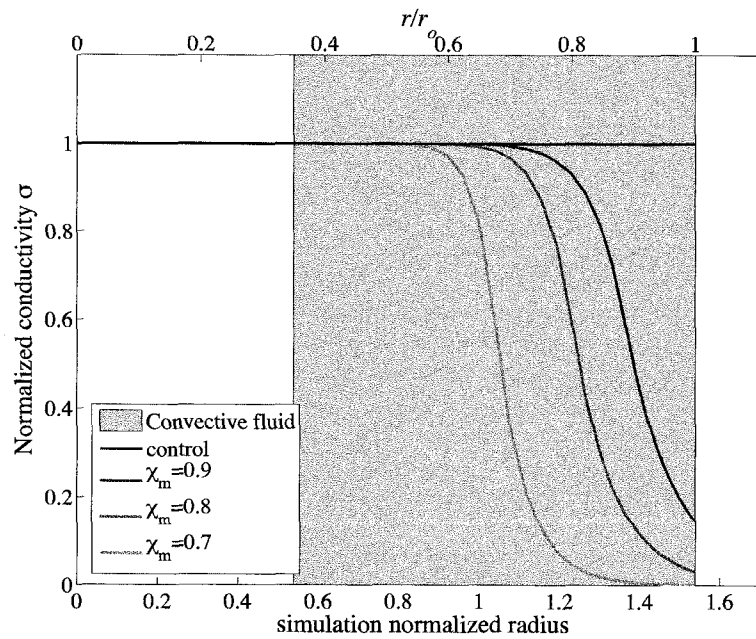
Figure 4.3: Comparison of different profiles of the normalized electrical conductivity. The simulated convective fluid is marked with a grey shade, the control case and three variable conductivity cases are shown in this figure.

Table 4.1: Mean and standard deviation of the time series for the kinetic and magnetic energies of the two tests presented in this chapter. Results for the first test, with $R_a = 2.8R_{a_c}$, are found in the grey cells. The results of the second test, with $R_a = 22.8R_{a_c}$ are presented in the white cells. We calculate mean energy for total, poloidal and toroidal for the kinetic ($E_k$, $E_{kp}$, and $E_{kt}$) and magnetic ($E_m$, $E_{mp}$, and $E_{mt}$) energies. We also include the poloidal energy at the outer boundary ($E_{r_o}$), and the axisymmetric poloidal energy ($E_{r_o ax}$) at the outer boundary. All models on this table use the same non-dimensional parameters: $E = 3 \times 10^{-4}$, $P_r = 1$, and $P_m = 5$.

| $\chi_m$ | $E_k$ ($\times 10^4$) | $E_m$ ($\times 10^4$) | $E_{r_o}$ ($\times 10^4$) | $E_{r_o ax}$ ($\times 10^4$) |
|---|---|---|---|---|
| control | 0.080 ± 0.013 | 0.254 ± 0.046 | 0.440 ± 0.660 | 0.836 ± 0.511 |
| 0.9 | 0.307 ± 0.003 | 0.251 ± 0.027 | 0.003 ± 0.001 | 0.003 ± 0.001 |
| 0.9 | 15.824 ± 1.918 | 3.860 ± 0.432 | 0.011 ± 0.005 | 0.002 ± 0.004 |
| 0.8 | 17.461 ± 3.260 | 2.346 ± 1.858 | 0.010 ± 0.061 | 0.007 ± 0.059 |
| 0.7 | 19.977 ± 3.125 | 0.450 ± 0.986 | 0.002 ± 0.026 | 0.002 ± 0.026 |

| $\chi_m$ | $E_{kp}$ ($\times 10^4$) | $E_{kt}$ ($\times 10^4$) | $E_{mp}$ ($\times 10^4$) | $E_{mt}$ ($\times 10^4$) |
|---|---|---|---|---|
| control | 0.080 ± 0.013 | 0.254 ± 0.046 | 0.440 ± 0.660 | 0.836 ± 0.511 |
| 0.9 | 0.064 ± 0.001 | 0.243 ± 0.003 | 0.061 ± 0.009 | 0.190 ± 0.019 |
| 0.9 | 5.852 ± 0.759 | 9.973 ± 1.269 | 1.934 ± 0.228 | 1.926 ± 0.225 |
| 0.8 | 6.332 ± 1.662 | 11.129 ± 1.756 | 1.225 ± 1.070 | 1.120 ± 0.820 |
| 0.7 | 6.989 ± 1.606 | 12.988 ± 1.698 | 0.230 ± 0.592 | 0.220 ± 0.406 |

the opposite is true for the variable conductivity case. The variable conductivity model allows us to access a weak field dynamo.

The toroidal component of the kinetic energy dominates over the poloidal component. Nevertheless, this dominance is not as strong as the one found for low electrical conductivity dynamos for example, Gómez-Pérez & Heimpel (2007). The magnetic energy is strong for the control case and relatively weak for $\chi_m = 0.9$. For the model where the Lorentz forces are geometrically constrained, the magnetic energy mean is about half, when compared to the control case for each, poloidal and toroidal components. The magnetic energy that is measurable on the planetary surface is the poloidal component at the outer boundary (see appendix B). Its time average and standard deviation are included in table 4.1. The contribution of axisymmetric energy at the outer boundary is greater for $\chi_m = 0.9$. In this case, the non-axisymmetric component is less than the standard deviation from the mean (i.e the axisymmetric component reaches, in average, 100% of the energy at the outer boundary), while in the control case only 80% of the total energy at the outer boundary is axisymmetric.

The temperature profile is changed due to the new fluid characteristics, and an equatorial cut is shown for a snapshot of both cases. On the variable conductivity model, the radius $r_m$ is marked by a white dashed line, see figure 4.4.

For the case of homogeneous electrical conductivity, the convection is non-stationary, hot plumes rise from the inner core boundary and distribute azimuthally with a symmetry of approximately order five (consistent with Heimpel et al. (2005a)). In the case of variable conductivity,
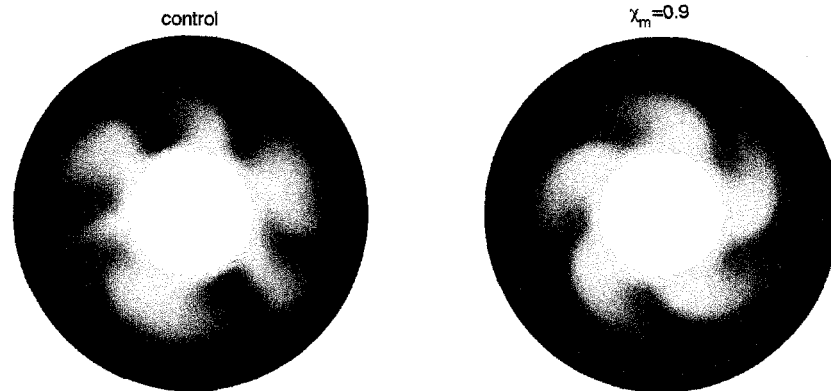
Figure 4.4: Equatorial cut of a snapshot of the temperature. For the control case and $\chi_m = 0.9$. Both figures here correspond to models with the $R_a = 2.8R_{a_c}$, $E = 3 \times 10^{-4}$, $P_r = 1$ and $P_m = 5$.

the plumes develop a quasi-stationary behaviour similar to that observed for a homogeneous fluid under a lower $R_a$.

To examine the behaviour of the velocity field, we include here an equatorial cut of the vorticity in the $z$ direction, $\omega_z = (\nabla \times \mathbf{u}) \cdot \hat{\mathbf{z}}$, see figure 4.5. Even though $R_a$ in both simulations is
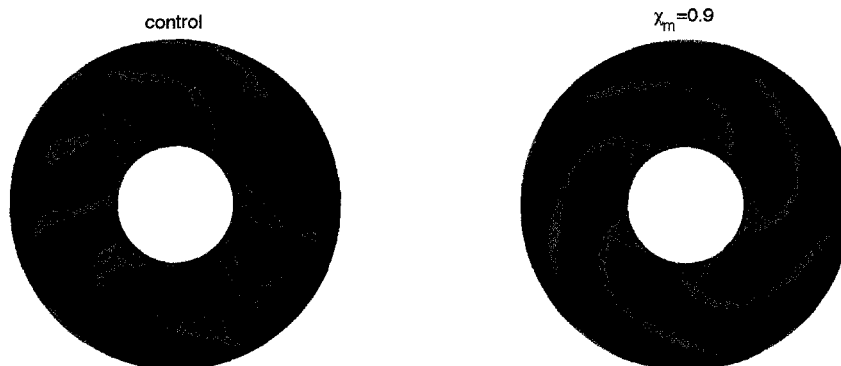


Figure 4.5: Equatorial cut of the $z$-vorticity for the control and $\chi_m = 0.9$ cases. For the variable conductivity case the sphere of radius $r_m$ is indicated with a black dashed line.

the same, the fluid seems to have a more vigorous and disorganized convection for the control case. For the variable conductivity fluid, the flow is organized with a regular azimuthal periodicity. In both cases the columns (defined by isosurfaces of $\omega_z$) are tilted in a prograde direction when increasing in radius. This is an effect of the geometrical constraint of the boundary conditions, see Busse (2002). For the variable conductivity case, the non-slip outer boundary does not increase the vorticity in the same fashion as the control case does. In both simulations there is

a detachment of the main vorticity column towards the outer boundary, and only for the control case, new strong vorticity maxima and minima are found at $r_o$.

The temperature and velocity fields are affected by the changing electrical conductivity, but the major effect is seen, as expected, on the magnetic field. The radial component of the magnetic field at the outer boundary, $r = r_o$, is presented here in figure 4.6. The resultant field at the outer
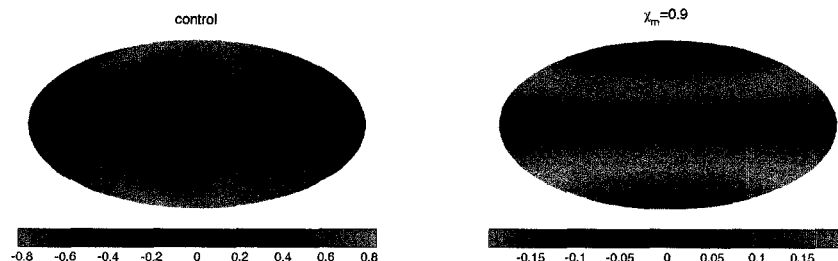


Figure 4.6: Maps of the outer boundary radial field in a Hammer projection.

boundary is significantly different for our two models. As expected, the magnitude of the field is lower for the variable conductivity model. In this case, the magnetic field is generated deeper and diffuses towards $r_o$ , thus when it reaches the outer boundary, its magnitude has decreased. In addition to the diffusion through the lower conductivity region, the physical volume that sustains the dynamo is lower, and this results in a lower total time averaged magnetic energy since we are averaging over the whole sphere, see table 4.1. Not only the magnitude but the symmetry of the resultant field is significantly different, as is seen in figure 4.6.

We include here the spectral decomposition of the radial component of the magnetic field at the outer boundary in figure 4.7. For this figure, we plot the energy stored on different harmonic orders and degrees (see equations 3.11 and 3.12). Figure 4.7(a) shows the dominance of the dipole for both models and also the strong octupolar component for the variable conductivity model. Figure 4.7(b) shows the axisymmetry of the control model with a weaker order component that can also be seen in figure 4.6. In contrast, the variable conductivity model is dominantly axisymmetric and the weak component of order five seen in the spectral decomposition is not easy to distinguish on the map of the external field (figure 4.6), since it is three orders of magnitude lower than the axisymmetric component.

### Electrically conductive volume

The second set of simulations presented here involves a change in $r_m$, the value of the radius defining the electrically conductive volume. For this purpose, and for finding sustained dynamos, it is necessary to increase the value of the Rayleigh number to $R_a \sim 23\,R_{a_c}$.

Three different values of $\chi_m$ are studied, $\chi_m = 0.9$, $\chi_m = 0.8$, and $\chi_m = 0.7$. The value of $R_a$ was chosen to be large enough to be able to sustain the dynamo with an electrical conductivity

(a)                                                          (b)
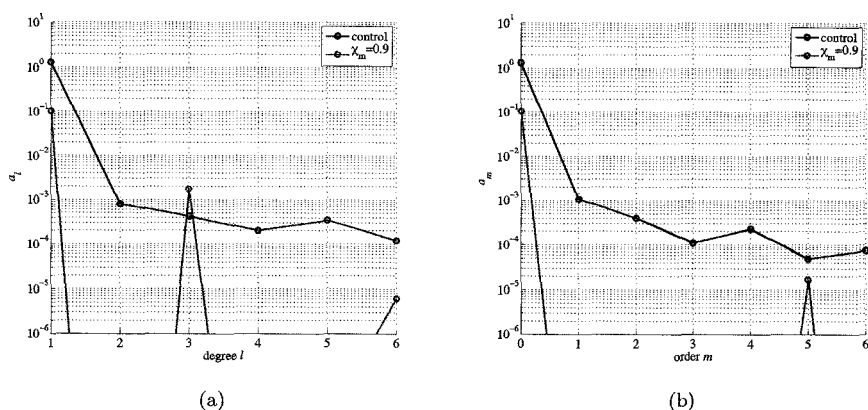
Figure 4.7: Energy stored per degree (a), and order (b). Both simulations result in a dominantly dipolar field, and the axisymmetric component is stronger for $\chi_m = 0.9$.

region restricted to 70% of the radius of the convective fluid. The profiles of the electrical conductivity as function of the radius are shown in figure 4.3.

As expected, the total averaged magnetic energy of the system decreases with decreasing $\chi_m$, see white cells in table 4.1. For this value of $R_a$, all dynamos are weak dynamos and the total energy (kinetic plus magnetic) remains approximately constant. Thus, the average kinetic energy increases by the same amount that the average magnetic energy decreases for lower values of $\chi_m$. For all cases the ratio of toroidal to poloidal components of the magnetic energy is close to one. In contrast, the kinetic energy is dominated by the toroidal component, being greater than the poloidal by roughly a factor of two. There is noticeable increase in the axisymmetric component for decreasing $\chi_m$ in the poloidal component of the magnetic field at the outer boundary. The axisymmetric component is 18% for $\chi_m = 0.9$, it is 70% for $\chi_m = 0.8$ and there is an insignificant (compared to the standard deviation from the mean) non-axisymmetric contribution for $\chi_m = 0.7$.

An equatorial cut of the temperature field for the three cases is presented in figure 4.8. There is no clear difference between the three models. The variation in electrical conductivity does not seem to affect the convection for this high $R_a$ simulations. The motion is driven by strong convection, and the magnetic force is not strong enough to modify the flow. The thermal plumes are more abundant than the ones present in the first test. This is due to the increase in $R_a$ (see Al-Shamali et al. (2004)).

The vorticity in the $z$ direction, $\omega_z$, does not seem to present a significant change between the various electrically conductive volumes either. For all cases, the high vorticity zones are localized by the outer boundary, centred around $r = 0.9 r_o$, in the equatorial plane. With respect to the kinetic energy and the fluid velocity, the three models seem not to present any difference of behaviour – besides the overall magnitude of the kinetic energy, which varies little between the three models. The general flow in the system is not affected by the magnetic field due to the
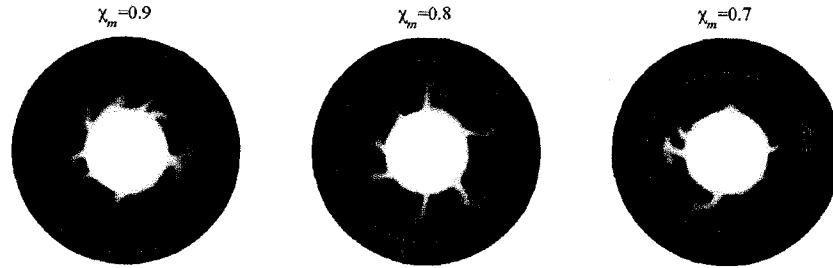
Figure 4.8: Equatorial cut of three snapshots of the temperature. For various values of $\chi_m$, from left to right 0.9, 0.8, and 0.7 All figures here correspond to models with the $R_a = 22.8 R_{a_c}$, $E = 3 \times 10^{-4}$, $P_r = 1$, $P_m = 5$ and $\chi = 0.35$.
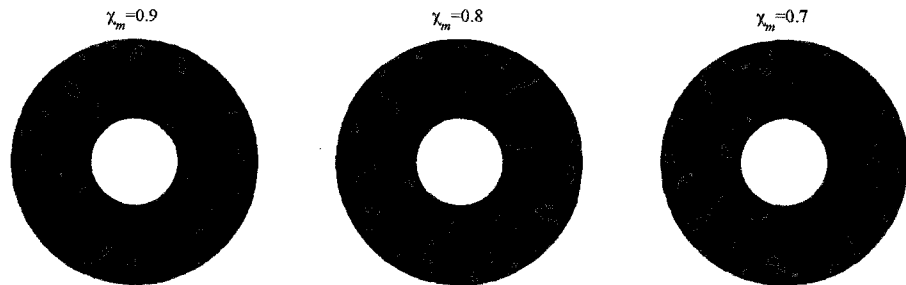


Figure 4.9: Equatorial cut of the vorticity in $z$ direction, $\omega_z$, for the three models. From left to right, $\chi_m = 0.9$, $\chi_m = 0.8$, and $\chi_m = 0.7$. The non-dimensional parameters used are the same used for figure 4.8.

very strong driving force.

In contrast, the magnetic field diffuses outward through the low conductivity fluid. The case with $\chi_m = 0.7$ has the lowest magnitude of the magnetic field at the outer boundary, followed by $\chi_m = 0.8$ with an intermediate magnitude, and $\chi_m = 0.9$ having the maximum magnitude shown in figure 4.10 but lower than the control case of the first test. The change in $\chi_m$ introduces a
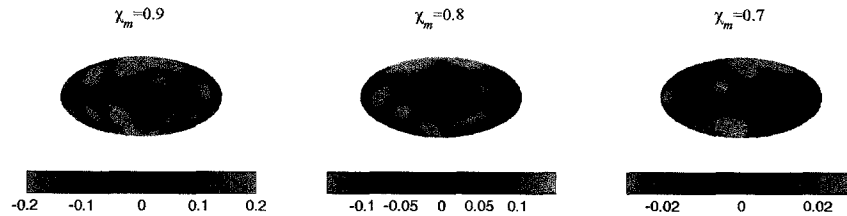


Figure 4.10: Radial magnetic field at the outer boundary. We include the colour map since the maxima and minima are different for each panel. The field is filtered up to degree 6.

noticeable change in magnitude due to the rapid diffusion through the low electrical conductivity fluid, see table 4.1.

The energy spectral decomposition of the poloidal magnetic field at the outer boundary is shown in figure 4.11. The change in $\chi_m$ influences the magnetic field outside and results in a



(a)                                      (b)
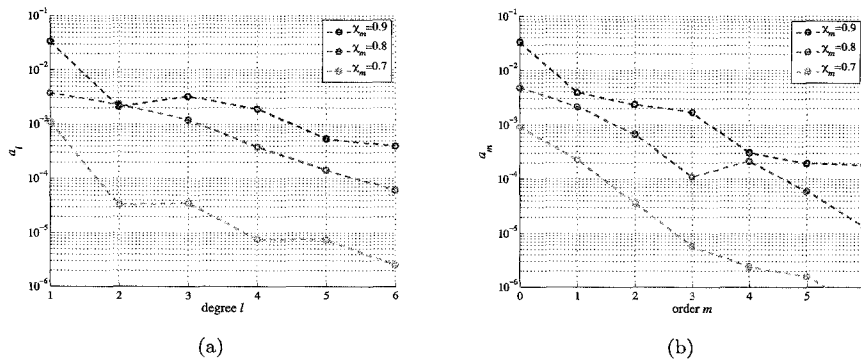
Figure 4.11: Spectral decomposition of the squared mean magnetic field for both degree (a) and order (b).

faster decrease of higher harmonics for a higher diffusive volume. For the lower $\chi_m$, the averaged poloidal magnetic field at the outer boundary ($r = r_o$) is more axisymmetric.

## 4.4 Discussion and Conclusions

In this chapter, the influence of different approximations (generally used in numerical simulations in fluid dynamics, and in particular dynamo action of planetary interiors) is studied. We introduce a modification in a numerical code in order to account for a radially variable electrical conductivity.

To neglect the change in density stratification in numerical simulations of dynamo action has been found to have a significant effect, Evonuk & Glatzmaier (2004). For systems where the change in density is small, which is the case for the iron cores of terrestrial planets, a homogeneous liquid using the Boussinesq approximation may be sufficient to describe the overall dynamics of the system. Unfortunately, a direct comparison for magnetic fluid under rotating convection with spherical boundaries for anelastic and Boussinesq approximations has not been studied, and to explore systematically the effects of non-dimensional parameters on both solutions would be interesting. The main drawback in carrying out such an experiment is the requirement of high cost in computational resources. A sound knowledge of the approximations used in the numerical simulations is necessary for the understanding of the reach of the simulations themselves. Characterizing the limitations of each approximation is important for finding strengths and weaknesses of our models, and in consequence, for having a better understanding of real physical systems.

Al-Shamali et al. (2004) present a comparison between $R_a = 1.1R_{a_c}$ and $R_a = 5R_{a_c}$ for three different values of the radius ratios studying exclusively thermal convection in rotating systems (no Lorentz forces). In the case of the highly supercritical $R_a$, they noted that there is a bifurcation in the $z$-vorticity columns at approximately the intermediate radius $r = r_i + D/2$. This effect is visible for our control model, see figure 4.5, and the results are consistent with magnetic convective models presented in chapter 2 (see also Heimpel et al. (2005a)). The control case, as expected, is sufficiently supercritical ($R_a \sim 2.8R_{a_c}$) to exhibit a non quasi-stationary solution, in contrast to those found for $R_a$ just above the onset of convection in Al-Shamali et al. (2004). On the other hand, for the same value of $R_a$ for the model with $\chi_m = 0.9$, the bifurcation of the $z$-vorticity columns is not visible. The convection cells form rolls that are homogeneously distributed in the azimuthal direction and extend parallel to the tangent cylinder, just as reported for the cases with low Rayleigh number ($R_a = 1.1R_{a_c}$) in Al-Shamali et al. (2004).

As a first approximation we may think that the effect of restraining the magnetic field generation to a smaller volume, has a similar effect to reducing $R_a$. Since the dynamo is restricted to a smaller volume the difference in temperature and the characteristic length scale that define $R_a$ is reduced, thus, there is an effect on lowering $R_a$ that drives the dynamo when the variable electrical conductivity model is used.

The non-magnetic and the homogeneous electrical conductivity cases both exhibit similar non-stationary flow behaviour that depends mostly on the super-criticality of $R_a$. In contrast, the solution for the variable conductivity case exhibits a quasi-stationary behaviour. In this test, the imposed change on the force balance at the top of the dynamo changes not only the magnetic force, but results in a change in the flow.

The magnetic field at the outer boundary, $r = r_o$, has a higher magnitude for the control case than the case with $\chi_m = 0.9$. In the later case, the magnetic field diffuses through the outer (low conductivity) shell of the simulated volume. The magnetic field at $r_o$, in both cases, is highly dipolar, more so for the control case than for $\chi_m = 0.9$. The high degree component is consistent with a higher radius ratio (thin shell dynamos). Since the magnetic field is restricted to a smaller volume, magnetic flux bundles that are correlated to the $z$-vorticity columns tend to have a lower latitude for higher values of $\chi$. This is consistent with the results reported in Heimpel et al. (2005a), where the radial magnetic field is concentrated outside the tangent cylinder, and this results in a magnetic field with low energy at the poles, and where high magnitude magnetic field zones are pushed to lower latitudes for higher $\chi$.

The axisymmetry of the radial component of the magnetic field at $r_o$ is significantly higher for the variable conductivity case. Since the effective $R_a$ driving the dynamo is lower, higher orders do not contribute significantly in the magnetic energy. This fact added to the diffusion of the field helps the axisymmetric component of the field to be dominant at $r_o$ for the case with $\chi_m = 0.9$.

The second test consists of a comparison between various volumes for confining the dynamo. We change $r_m$ keeping invariable all other parameters. For this experiment to be successful, a higher $R_a$ is required. $R_a$ is incremented by a factor of eight from the first test and as a consequence the kinetic energy in the system is high (we find exclusively weak dynamos), see table 4.1. For the three cases presented in this test, the flow follows the same general behaviour. The thermal plumes at the equator fill the whole simulated volume and the convection is not affected by the change in $\chi_m$. The $z$-vorticity exhibits also a similar behaviour for all three cases, changing character at mid-shell ($r = r_i + D/2$) comparable with the highly supercritical rotating convection simulations reported in Al-Shamali et al. (2004).

The magnetic field on the other hand, is different for different values of $\chi_m$. The dipolar and axisymmetric components of the field are relatively higher for lower $\chi_m$. The diffusion over the low electrical conductivity fluid filters rapidly high harmonic degrees and orders, thus it is reasonable to find lower contributions of high harmonic coefficients with the decrease of $r_m$. For the snapshots presented in this test, for the $\chi_m = 0.8$ model, both $a_{l=2}$ and $a_{m=1}$ energies are high compared with $a_{l=1}$ and $a_{m=0}$ energies respectively. This case has the most non-axisymmetric and non-dipolar field geometry. This characteristic depends on the randomly picked time. The time averaged magnetic field indicates the tendency for the axisymmetric component to increase with decreasing $\chi_m$.

We found that the flow may be changed by changing the electrical conductivity on the fluid. One of the consequences of the decrease in electrical conductivity towards the outer shell is an increase in the axisymmetry of the field at the outer boundary. If this is true for models with non-slip boundary conditions, the high axisymmetry of Saturn may be an effect of the electrical conductivity profile at the planet's interior. We found exclusively weak dynamos. Planetary bodies are likely to hold a magnetostrophic balance, and thus the dominance of the kinetic energy may be not desirable to model terrestrial or gas giants (note that this is not true for the ice giants, see chapter 3). We need to explore further a range of non-dimensional parameters and

possible initial conditions, since they may affect the energy balance in the resultant dynamos (see chapter 2).

# Chapter 5

# Radially variable electrical conductivity: An application to the gas giants

## 5.1 Introduction

In the XX century, prolific space exploration advances gave us information never before known. A brief summary of space missions that have visited Jupiter, follows here. Pioneer 10 was the first spacecraft to take in situ measurements of Jupiter's magnetosphere, flying by, in December of 1973, at about 130,000 km from the planet's cloud top ($2.8R_{Jupiter}$). Pioneer 10 was followed by Pioneer 11, in December 1974 (approaching the planet at $1.4R_{Jupiter}$). Even better mappings of the magnetic field and gravitational moments were possible after the fly by of Voyager I in March of 1979. Jupiter was then visited by Voyager II in July 1979. The Galileo orbiter observed the collision of a massive asteroid (Shoemaker-Levy 9) with Jupiter. This spacecraft also carried a probe to sample Jupiter's atmosphere. Deployed in December of 1995, Galileo's probe found a hydrogen/helium proportion close to solar but somewhat helium depleted. The probe was operational to a depth of roughly 200km and obtained temperature, pressure, and composition profiles as function of depth for Jupiter's atmosphere (Niemann et al. (1996)).

Saturn's spacecraft missions may be similarly summarized. Pioneer 11 flew by Saturn in September 1979 at about 22,000 km above Saturn's clouds ($1.3R_{Saturn}$). Voyagers I and II collected magnetic field data from Saturn briefly after flying by Jupiter. Cassini-Huygens was launched in October 1997 as a mission to study Saturn. After they reached Saturn the Huygens probe was released towards Titan in October 2004. Huygens reached Titan surface in January 2005. The Cassini spacecraft is currently orbiting Saturn. With these advances and increasingly accurate measurements, the gas giants of the solar system are becoming better understood than ever before.

The gas giants' stratification can be determined based on the planet's total mass, $M$, equato-

rial radius, $a$, and even number gravitational moments, $J_2, J_4$ and $J_6$ (Stevenson (1982), Guillot (1999b)). Based on apriori models of 3 layers and an equation of state (i.e. the density as function of temperature and pressure), the extent of these layers may be determined by finding a solution that matches mass and gravitational moments measured. The main problem in determining the interior stratification of the gas giants arises from the possibility of inhomogeneous regions; transition zones from atomic to metallic hydrogen. Such zones may be also associated with a change in helium concentration.
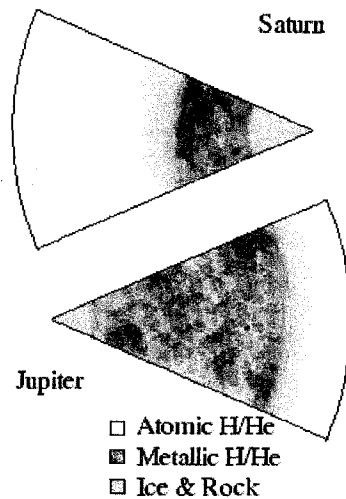


Figure 5.1: Schematic representation of Saturn's and Jupiter's interior. Boundary layers are not well defined due to uncertainties in the equation of state of H/He mixtures at high pressures.

Based on estimates by Guillot (1999a) and Stevenson (1982) the gas giants may have rocky cores with upper bound radii of $0.22R_{Saturn}$ and $0.15R_{Jupiter}$ for Saturn and Jupiter respectively, see figure 5.1. These estimates require Saturn to have a rocky core, but for Jupiter, interior models without a core are also possible. Despite the fact that solutions of internal models define density distributions, the state of the core is not known. A core that is not solid but rather dissolved in the metallic hydrogen/helium fluid is as likely as a solid rocky core. Using a simplified equation of state, transition phases as a function of pressure may be estimated. This results in transition zones from metallic to atomic hydrogen at $0.5R_{Saturn}$ and $0.8R_{Jupiter}$, for Saturn and Jupiter respectively.

Constraints given by gravitational moments, planetary mass, and radii will only determine quantities averaged over extended regions of the interior, and are of little help in determining slow changes in transitions zones. Before the interior of the gas giants can be sufficiently understood, efforts will need to focus on understanding equations of state for fluid under high pressures and temperatures.

Arguments in favour of slow density changes are suggested by experimental results. It has

not been possible experimentally to find a discontinuity for the atomic/metallic transition for hydrogen, and measurements showing continuous changes in the electrical conductivity (and hence density) as a function of pressure and temperature have been reported. Nellis (2000) proposed that electrical conductivities in the interior of Jupiter may be significant up to $0.95R_{Jupiter}$, and that the extent of the dynamo region may reach further in radius than what was proposed previously in Guillot (1999b).

Magnetic fields on the gas giants have been found to be dipolar and axisymmetric (Connerney et al. (1998)). In the case of Saturn the field is particularly axisymmetric, more so than any other dynamo in the solar system. A first possibility is that the field geometry is highly axisymmetric due to the intrinsic generation mechanism in Saturn. A second possibility may be that the field is modified outside the dynamo region. As we briefly mentioned in chapter 3, numerical studies have found that the axisymmetry of the magnetic field measured outside the dynamo region may be related to the symmetry of an external flow. Love (2000) uses kinematic dynamo simulations where the flow is defined in two regions. A combination of a toroidal and poloidal flow field is defined in an internal sphere. An outer, non-convecting envelope is included where two different velocity profiles are imposed (one with solid body rotation and one including radial shearing). As stated by Love (2000), results indicate that the envelope helps to modify the magnetic field geometry from a weakly non-axisymmetric underlying dynamo to an axisymmetric field at the outer boundary. This is true only when a dominant axial dipole is the underlying magnetic field symmetry. For cases where the underlying field is dominated by equatorial dipoles (highly non-axisymmetric), the non-axisymmetric component is increased by the presence of the overlying (axisymmetric) flow.

Zhang & Schubert (2006) also presented an analysis of kinematic dynamos and the influence of a shear flow overlying layer on magnetic field symmetries at the outer boundary. Using simplified equations of motion and a finite difference method, they solve for a magnetic field on a non linear dynamos. They defined three regions: a solid inner core, a turbulent convective fluid, and a shear flow layer that is not thermally affected by the underlying convection. The magnetic field is generated only in the convective zone and it diffuses to the other two layers, internal and external, by following boundary conditions (continuity of the radial component of the magnetic field induction vector). For the model of Zhang & Schubert (2006), the presence of the enveloping layer changes the symmetry of the outer field to match the symmetry of the overlying flow, independent of the underlying magnetic field. In that paper two dynamo models are presented, but the range of magnetic Reynolds numbers ($R_m$) explored is limited. Love (2000) found that for high enough $R_m$, equatorial dipoles are the solution of the underlying dynamo, and the consequences of the overlying symmetry may be significantly different to what was found by Zhang & Schubert (2006).

The variable conductivity model presented in chapter 4 will help us understand the role of decreasing conductivities at the top of the metallic hydrogen layer in the gas giants.

## 5.2 Methodology

In this chapter, we use the Boussinesq approximation to study the effect of a radially variable electrical conductivity. We present results for four numerical calculations of three-dimensional, self-sustained dynamos. For two of the runs, the electrical conductivity, $\sigma(r)$, decreases exponentially for $r > r_m$, as defined by equation 4.23 (see Fig. 5.2). The radial grid density of these
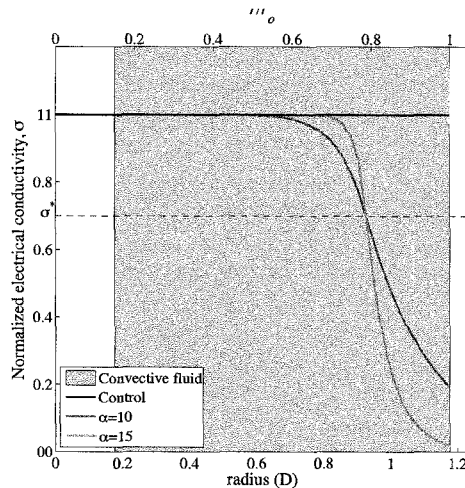


Figure 5.2: Electrical conductivity of the fluid as a function of radius for the models used in this chapter.

simulations is increased with respect to the criteria used and explained in previous chapters (see section 2.2) to obtain a good resolution at the interface between the electrically conductive and non-conductive liquids. The decay in the polynomial for $\sigma(r) < r_m$ (see equation 4.23) is chosen to have at least four grid points where $0.99 < \sigma(r)\sigma^*$.

A comparison between three different electrical conductivity profiles is presented in this chapter. As a control, we use two models with constant electrical conductivity and two values of $R_a$, i.e. $R_a = 4.8R_{a_c}$ (control 1) and $R_a = 8R_{a_c}$ (control 2), see table 5.1. Simulations with

Table 5.1: Parameters of the simulations in this chapter. The simulations share common parameters $\chi = 0.15$, $E = 10^{-4}$, $P_r = 1$, and $P_m = 5$.

|  | control 1 | control 2 | $\alpha = 10$ | $\alpha = 15$ |
|---|---|---|---|---|
| $R_a$ | $6 \times 10^6$ | $10^7$ | $10^7$ | $10^7$ |
| $R_a/R_{a_c}$ | 4.8 | 8 | 8 | 8 |
| $\alpha$ | - | - | 10 | 15 |
| $\sigma^*$ | - | - | 0.7 | 0.7 |
| $\chi_m$ | - | - | 0.8 | 0.8 |

$R_a = 4.8R_{a_c}$ and variable electrical conductivity resulted in failed dynamos and are not presented in this chapter ($\alpha = 10$ and $\chi_m = 0.8$). We choose a thick shell dynamo, $\chi = 0.15$, in order to

simulate the interior of the gas giants. Both velocity boundary conditions, top and bottom, are chosen to be stress free. We use an electrically conductive inner core (see figure 5.2). The conductivity of the inner core is used to define the value of $P_m = 5$. We use $P_r = 1$ and $E = 10^{-4}$. For both variable conductivity calculations $\chi_m = 0.8$, $\sigma^* = 0.7$, see equation 4.23. We will refer to them as $\alpha = 10$ and $\alpha = 15$ in this chapter. In three of these simulations (control 1, $\alpha = 10$, and $\alpha = 15$) we use mild hyperdiffusivities, the same as in chapter 3, and a high grid resolution (61 radial levels and 512 azimuthal grid points). For control 2, we used hyperdiffusivities ten times stronger than those of chapter 3, and a lower resolution grid (41 radial levels and 384 azimuthal grid points).

We find control 2 not to be developed completely in time. The stationary state for the velocity field has not been not reached by the time this dissertation is written. It has, nevertheless developed stable energy time series.

## 5.3 Results

We present results for the four sustained dynamos found in this study. The resolution of these models is relatively high and the simulations are computationally expensive. The quasi-stationary state in the energy time series is reached for all runs. The time averaged energies, i.e. kinetic and magnetic, along with their respective poloidal and toroidal components are presented in table 5.2. Energy scale is the same as for all previous chapters. Kinetic energy is calculated based on the Reynolds number and the magnetic energy is related to the Elsasser number as presented in page 25. The total time averaged kinetic energy ($E_k$) is greater for the variable

Table 5.2: Mean and standard deviation of the time series for the kinetic and magnetic energies of the four cases presented in this chapter. The mean of the total magnetic and kinetic energies, $E_m$ and $E_k$ respectively, along with their toroidal and poloidal components, $E_{mt}$, $E_{mp}$, $E_{kt}$, and $E_{kp}$, are calculated for one viscous time, $\tau_\nu$. We also include the mean of the poloidal energy at the outer boundary, $E_{r_o}$, and the axisymmetric component of the poloidal energy at the outer boundary $E_{r_oax}$. All runs presented have $\chi = 0.15$, $E = 10^{-4}$, $P_r = 1$, and $P_m = 5$.

| | $E_k$ ($\times 10^3$) | $E_m$ ($\times 10^3$) | $E_{r_o}$ ($\times 10^3$) | $E_{r_oax}$ ($\times 10^3$) |
|---|---|---|---|---|
| control 1 | 7.469±1.446 | 18.587±10.650 | 0.120±0.087 | 0.087±0.037 |
| control 2 | 15.593±2.494 | 46.102±8.874 | 0.769±0.207 | 0.662±0.187 |
| $\alpha = 10$ | 18.531±3.356 | 5.629±2.469 | 0.005±0.002 | 0.003±0.002 |
| $\alpha = 15$ | 19.788±3.296 | 6.284±2.061 | 0.005±0.003 | 0.003±0.002 |

| | $E_{kp}$ ($\times 10^3$) | $E_{kt}$ ($\times 10^3$) | $E_{mp}$ ($\times 10^3$) | $E_{mt}$ ($\times 10^3$) |
|---|---|---|---|---|
| control 1 | 1.250±0.386 | 6.219±1.337 | 3.974±4.346 | 14.613±6.763 |
| control 2 | 3.254±0.603 | 12.340±2.011 | 14.891±3.258 | 31.211±6.520 |
| $\alpha = 10$ | 1.964±0.650 | 16.567±3.003 | 1.484±0.767 | 4.145±1.732 |
| $\alpha = 15$ | 1.998±0.621 | 17.790±2.902 | 1.819±0.677 | 4.465±1.428 |

conductivity cases when compared to control cases. It is sensible to find a significant increase of

the total kinetic energy with higher $R_a$, thus, it is expected for the variable conductivity models to have a greater kinetic energy than control 1. Control 2 has also a lower kinetic energy than the variable conductivity cases. This indicates that the existence of zones where the Lorentz forces are not significant allows stronger kinetic energies to develop. From table 5.2, it is clear that the decrease in magnetic forces favours increased toroidal kinetic energies.

The ratio between toroidal and poloidal kinetic energies is $\sim 5$ for control 1, $\sim 4$ for control 2, 8.4 for $\alpha = 10$, and 8.9 for $\alpha = 15$. Since $P_m = 5$, we do not expect dominant zonal flows as those discussed in chapter 3. Since the electrical conductivity for most of the volume is high, the zonal flow is slowed down by the magnetic forces. Nevertheless, the values obtained for the ratio of toroidal to poloidal kinetic energies for the variable conductivity cases are comparable to the toroidal to poloidal ratios from $P_m = 0.3$ simulations in chapter 3. It is important to note that, since magnetic energies are negligible for $r > r_m$, total volume energy averages do not refer directly to force balances in the fluid as they did in the cases presented in chapter 3.

The total magnetic energy for control 2 is significantly greater than for all other runs. Since the driving energy is greater and the volume sustaining the dynamo maximum, a larger magnetic energy for control 2 is to be expected. The total time averaged magnetic energy of the control cases is significantly higher (by over a factor of three) than the variable conductivity cases. The difference in electrically conductive volume for $\chi_m$ and $\chi = 0.15$ between the homogeneous and the variable conductivity liquids is about a factor of two. The decrease in the magnetic energy for the variable conductivity cases is evident, and it is not caused by averaging over the whole fluid alone. We find that both variable conductivity cases are weak dynamos, i.e. the total magnetic energy is lower than the total kinetic energy.

We can study the effect of the variable conductivity on the overall flow. An equatorial cut of the temperature profile for the control models is shown in figure 5.3. On the top left panel, control 1 results in a single plume reaching approximately $r = (r_o + r_i)/2$. On the top right hand side, control 2 results in two hot plumes rising to the outer boundary; the temperature profile is heterogeneous through out the whole fluid core. The equatorial temperature profile shows significant changes when comparing the two control models. The increase in the dominant order $m$ of the temperature profile with $R_a$ is consistent with previous studies reported in the literature (see section 3.4 in Al-Shamali et al. (2004) on supercritical convection).

For the variable conductivity models, $\alpha = 10$ and $\alpha = 15$, the differences between the equatorial profiles are less significant, see bottom row in figure 5.3. In both cases, hot plumes rise to approximately $r = 0.8r_o$ (as opposed to control 2 for which the plumes approach $r = r_o$). The number of plumes rising from the inner core are consistent with higher $R_a$ when compared to control 1. The variable conductivity simulations present four plumes for the snapshots graphed. It is interesting to note that control 2 has only two main convective plumes; the increase in the convective wavenumber, $m$, is a direct result of the variable conductivity. The snapshots in figure 5.3 present radially stratified temperatures for $r > r_m$. This is more evident for $\alpha = 15$.

We include azimuthal components of the velocity field for all cases at the outer boundary in figure 5.4. We marked the projection of the tangent cylinder (see page 6) with two white lines. A tangent cylinder defined by the surface $r = r_m$ may also be defined, we call this surface
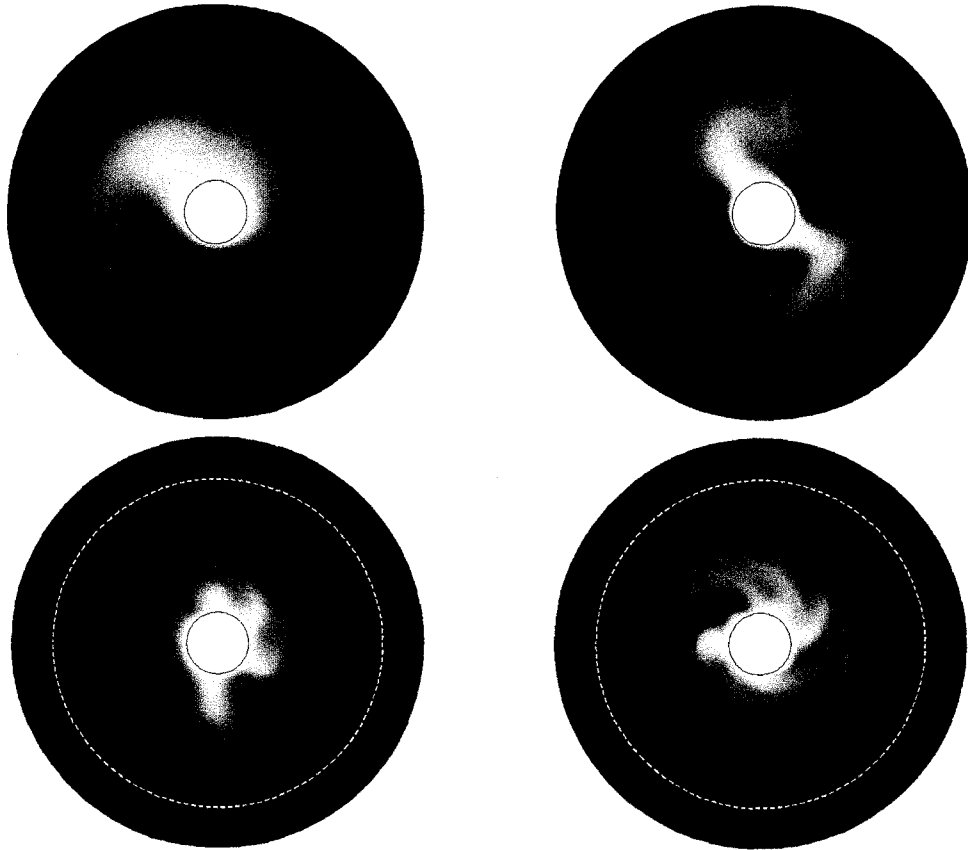
Figure 5.3: Equatorial cut of the temperature profile for cases control 1, control 2, $\alpha = 10$ and $\alpha = 15$. On the left panel of the top row, control 1 with $R_a = 4.9 R_{a_c}$. On the right panel of the top row, control 2 with $R_a = 8 R_{a_c}$. On the bottom row, $\alpha = 10$ on the left and $\alpha = 15$ on the right, both with $R_a = 8 R_{a_c}$. The white dashed line corresponds to $r = r_m$
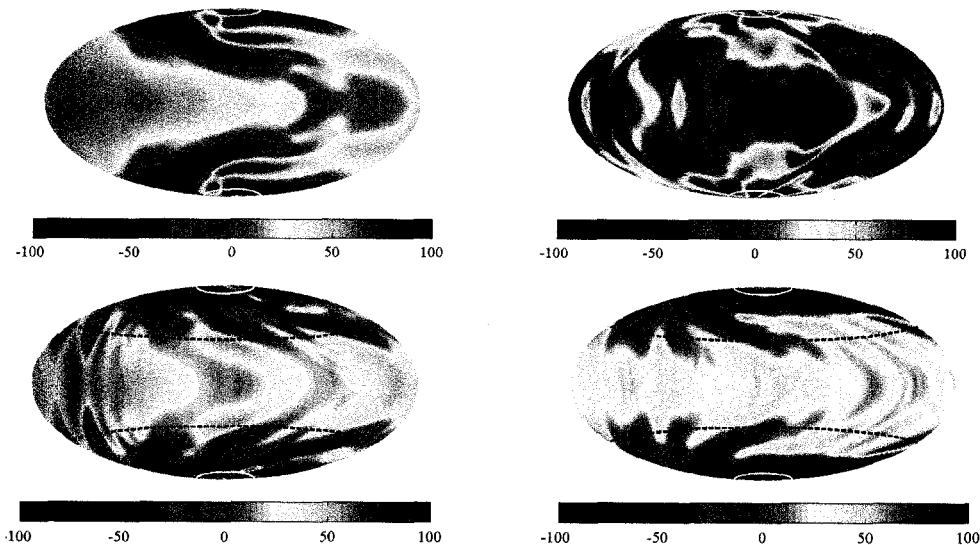
Figure 5.4: Azimuthal velocity, $u_\varphi$, at the outer boundary $(r = r_o)$. On the top row, control 1 on the left, and control 2 on the right. On the bottom row, $\alpha = 10$ on the left, and $\alpha = 15$ on the right. The projection of the tangent cylinder (see text) onto the the outer boundary, is marked with white lines. On the bottom, we include as well the projection of the tangent cylinder defined by $r_m$, i.e. the variable conductivity tangent cylinder, in black dashed lines.

the *variable conductivity tangent cylinder*. The projection of the variable conductivity tangent cylinder is marked with black dashed lines in figure 5.4.

The three cases with higher $R_a$ have smaller scale flow features at the outer boundary when compared with case control 1. The azimuthal velocity, $u_\varphi$, is high close to the tangent cylinder; the magnitude maxima for the control cases are located close to the tangent cylinder lines. The variable conductivity cases exhibit high azimuthal velocity at the tangent cylinder as well, but the maxima have lower latitudes, and are found closer to the variable conductivity tangent cylinder. The quasi-stationary state expected for a stress free outer boundary, under geostrophic conditions (for definition see page 22), yields strong zonal flows with a prograde equatorial jet (e.g. Aurnou & Heimpel (2004)). It is clear that an equatorial jet has been formed for all cases except control 2. It is very important to note that, possibly due to insufficient run time, the control 2 $(R_a = 8R_{a_c})$ case did not reach a state where the velocity flow is quasi-stationary. This will have a significant effect on the velocity, as it may be seen in figure 5.4.

For the same simulations and snapshots, we include a meridional slice (constant $\varphi$) of the azimuthal velocity (figure 5.5). For all four runs, the azimuthal flow is organized into columns parallel to the axis of rotation. The flow is dominated by the toroidal component (see table 5.2), and we find that the flow is quasigeostrophic (see page 22). Nevertheless, non-geostrophic zones are evident. Close to the tangent cylinder, we find non-geostrophic features close to the outer boundary, where $u_r$ and $u_\theta$ are significant when compared to $u_\varphi$. Vertical columns in the azimuthal
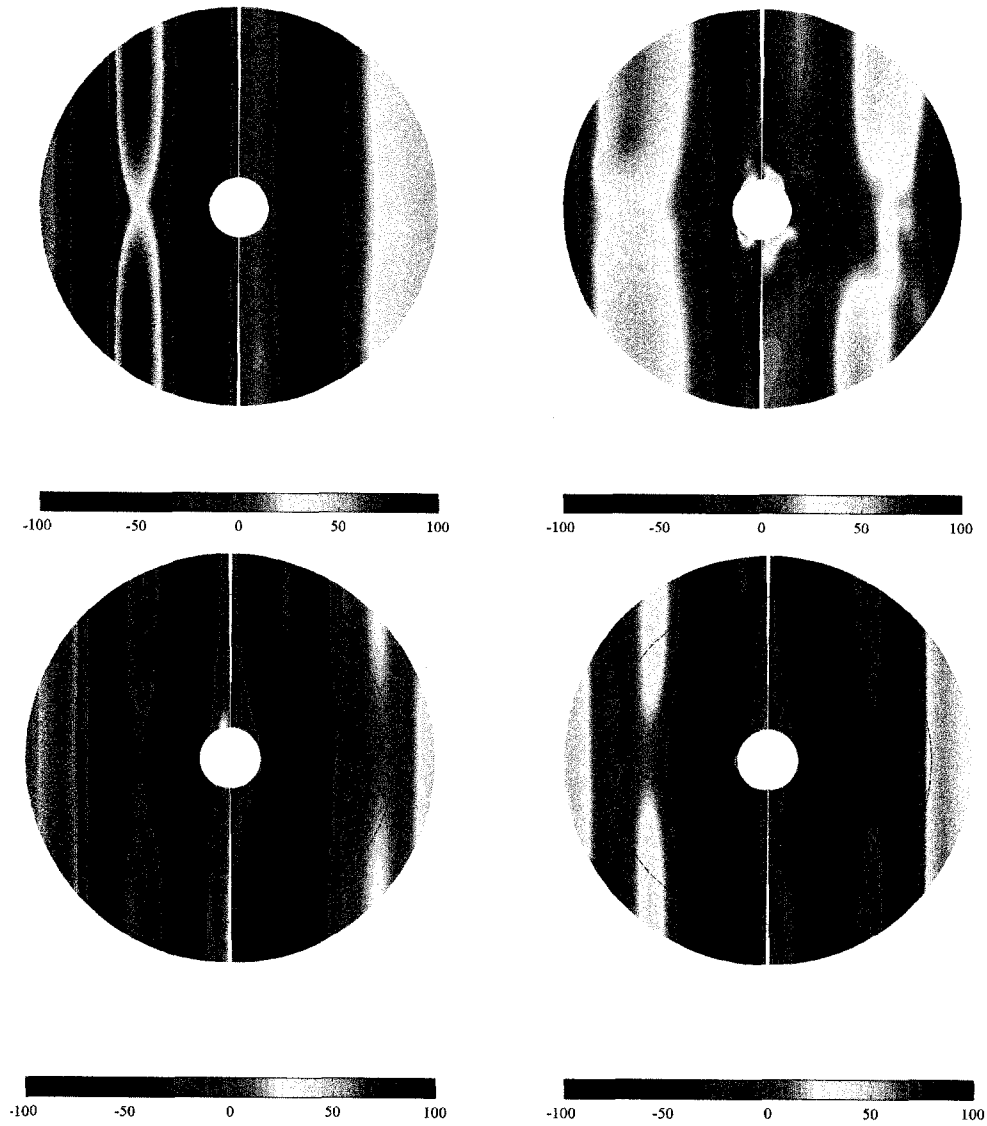
Figure 5.5: For all four cases, the azimuthal velocity, $u_\varphi$, for a meridional slice ($\varphi = 0$). In this plot, the axis of rotation is vertical. The colour-map is the same as for figure 5.4

velocity profile tend to be broken for higher $R_a$. The two variable conductivity simulations show disturbances from a geostrophic balance near the tangent cylinder. Control 2, shows disturbances though out the whole fluid core.

Quasigeostrophic flows with strong toroidal components yield banded structures at the surface (e.g. Busse (1994)). We present in figure 5.6 (as we did in chapter 3) the azimuthally averaged, azimuthal Rossby number, $R_o = E R_e$; where $R_e = u_\varphi D / \nu$ is the Reynolds number associated with the $\varphi$ component of the velocity $\mathbf{u}$. The resultant surface flows for both variable conductivity
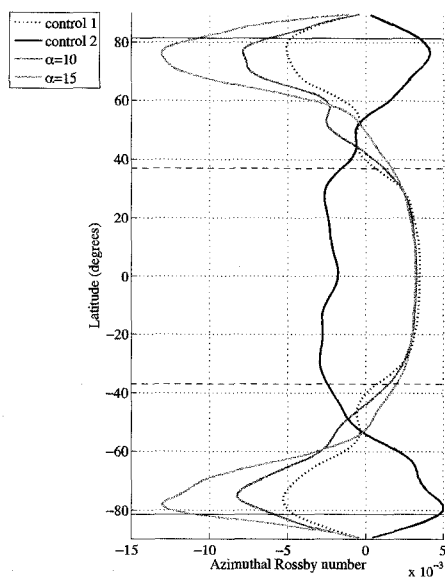


Figure 5.6: Latitude, versus averaged azimuthal Rossby number $R_o = E R_{e_\varphi}$, where $R_e$ is the Reynolds number. The azimuthal velocity at the outer boundary $u_\varphi(r = r_o, \theta, \varphi)$ is averaged in the azimuthal direction. We include all cases: control 1, control 2, $\alpha = 10$, and $\alpha = 15$. The dotted line, control 1 results from $R_a = 4.8 R_{a_c}$. All simulations plotted with solid curves correspond to $R_a = 8 R_{a_c}$. Latitudes of the projection of the tangent cylinder on the outer boundary are marked with horizontal solid black lines, and those of the variable conductivity tangent cylinder are marked with dashed black lines.

cases are almost indistinguishable for both values of $\alpha$ chosen, see bottom row of figure 5.4. Even though control 2 reached a quasi-stationary state in the energy time series, an equatorial prograde jet is not found. The development of this jet may require longer run times. For the time developed simulations, two strong reverse jets are found approximately at the tangent cylinder (marked with horizontal solid lines in figure 5.6). The strength of these retrograde jets is higher for higher values of $\alpha$, i.e. higher electrical conductivity decay rate. There is a latitude where the fluid deviates from being geostrophic, where there is a plateau for $R_o$ as a function of latitude, see figure 5.6. The latitude of this plateau is independent of the variable conductivity or value of $\alpha$ for the cases studied. The plateau is likely a consequence of the change in direction of the

flow; early stages of the simulations presented weak retrograde equatorial jets and, they reverse direction with time.

To analyse the magnetic field geometry, it is useful to separate the energy contribution by harmonic degrees and orders. The normalized spectral decomposition of the poloidal component of the magnetic field at the outer boundary, $r = r_o$, is shown in figure 5.7. All models are
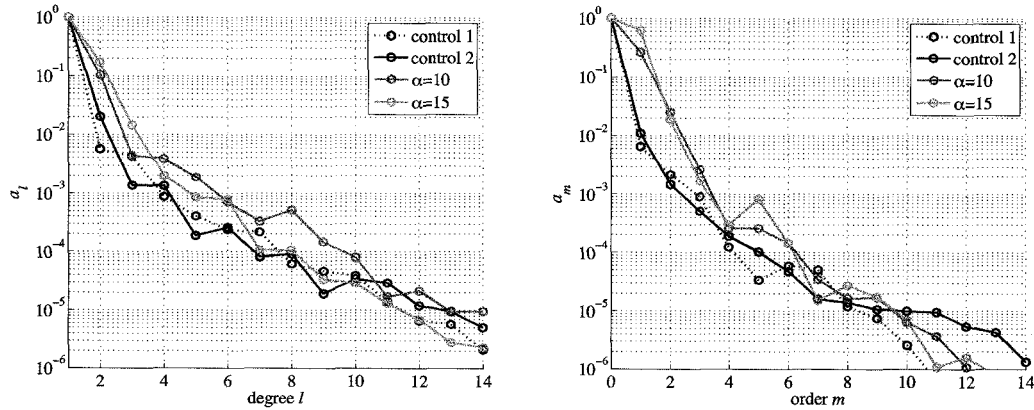


Figure 5.7: Spectral decomposition of the magnetic energy at the outer boundary per degree, $a_l$, and per order $a_m$. We present here both control cases, (with a homogeneous electrical conductivity) control 1, $4.8R_{a_c}$, and control 2, $8R_{a_c}$. Also shown are variable conductivity cases with $\alpha = 10$, and $\alpha = 15$ with $R_a = 8R_{a_c}$.

dominantly dipolar. The quadrupolar energy for the variable conductivity cases is about one order of magnitude lower than the dipolar. In contrast, for both control cases the quadrupolar energy is about two orders of magnitude lower than the dipolar. The case with $\alpha = 15$ presents a stronger non-axisymmetry closely followed by $\alpha = 10$ both far from the axisymmetric control cases. This is shown by the relative magnitude of $a_m$ with respect to $a_{m=0}$. For values of $\alpha$ and $R_a$ chosen, the snapshots show no preference for the axisymmetric or dipolar fields by the variable conductivity models.

In addition to the spectral decomposition, maps of the radial component of the magnetic field at the outer boundary are shown in figure 5.8. The control cases present smaller scale features when compared to the variable conductivity cases. In particular higher order components. There is not a clear tendency for high harmonic degree to decrease faster in the variable conductivity cases (they do not show particularly strong dipolar fields).

As expected, the magnitude of the field at the outer boundary is lower (by about one order of magnitude) for the variable conductivity cases when compared to control 2. The typical length scale of the features and the magnitude of the magnetic fields, both at the outer boundary, are a consequence of the diffusion over the low electrical conductivity volume.

The magnetic field magnitude is variable in time. Magnetic fields for $\alpha = 10$ snapshot seem slightly higher than that for $\alpha = 15$, but as seen in table 5.2 this is only due to the time chosen for graphing. The time averaged energies at the outer boundary, $E_{r_o}$, are indistinguishable for
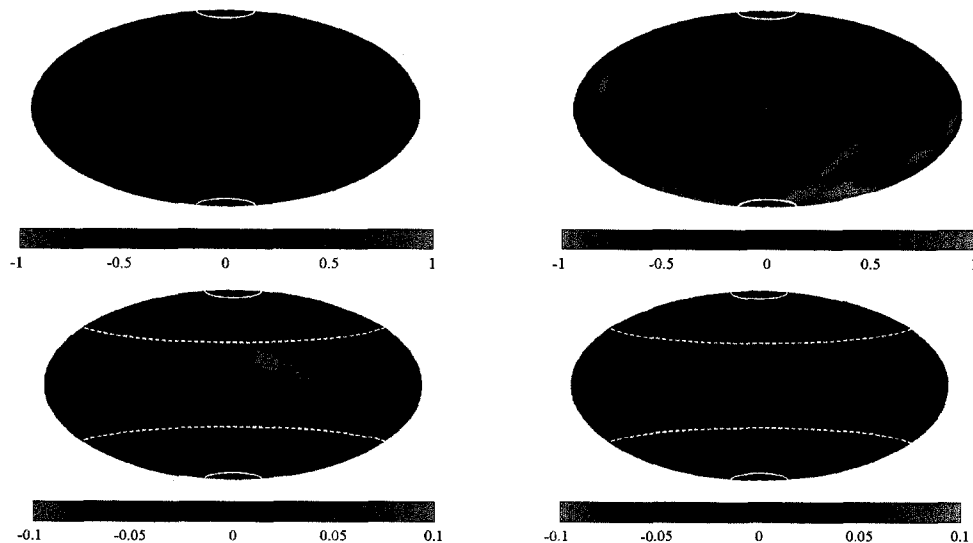
Figure 5.8: Radial component of the magnetic field at the outer boundary, $r = r_o$. On the left top panel: control 1 with homogeneous electrical conductivity and $R_a = 4.8R_{a_c}$. On the right top panel: control 2, also with a constant electrical conductivity but with $R_a = 8R_{a_c}$. On the left bottom panel: $\alpha = 10$ with variable electrical conductivity and $R_a = 8R_{a_c}$. On the right bottom panel: $\alpha = 15$, also with variable electrical conductivity and with $R_a = 8R_{a_c}$.

both variable conductivity cases.

The poloidal field lines and the radial magnetic field, for longitudinal cuts of $\varphi = 0$, are shown in figures 5.9 and 5.10. Both control cases (figure 5.9) present a mostly dipolar magnetic field all though the fluid. In contrast, the variable conductivity cases (figure 5.10) present a more complicated internal field geometry. As expected, for the low electrical conductivity envelope, the field line density (i.e. magnetic field intensity) is lower and $B_r$ is much weaker, when compared to the field in the internal volume, $r < r_m$.

In figure 5.10, $B_r$ maxima for the variable conductivity cases are comparable to those of the case control 2. However, they extend through a confined volume roughly inside the tangent cylinder. Smaller scale fields are found for the variable conductivity cases, where a typical length scale is of the order of $r_i$ in the horizontal direction, as opposed to $D = r_o - r_i$, in the control cases.

The velocity fields present length scales comparable to those of the magnetic fields. To illustrate this, we present two figures analogous to figures 5.9 and 5.10. In figures 5.11 and 5.12, we show the poloidal stream-lines and the radial component of the velocity field, $u_r$ for an azimuthal cut of $\varphi = 0$. There is a noticeable difference in the length scale of the stream-lines just outside the tangent cylinder between control and variable conductivity cases (particularly control 1). For the variable conductivity cases, $u_r$ maxima are found inside and at the boundary of the tangent cylinder, the same zones where $B_r$ maxima are located, however not a noticeable
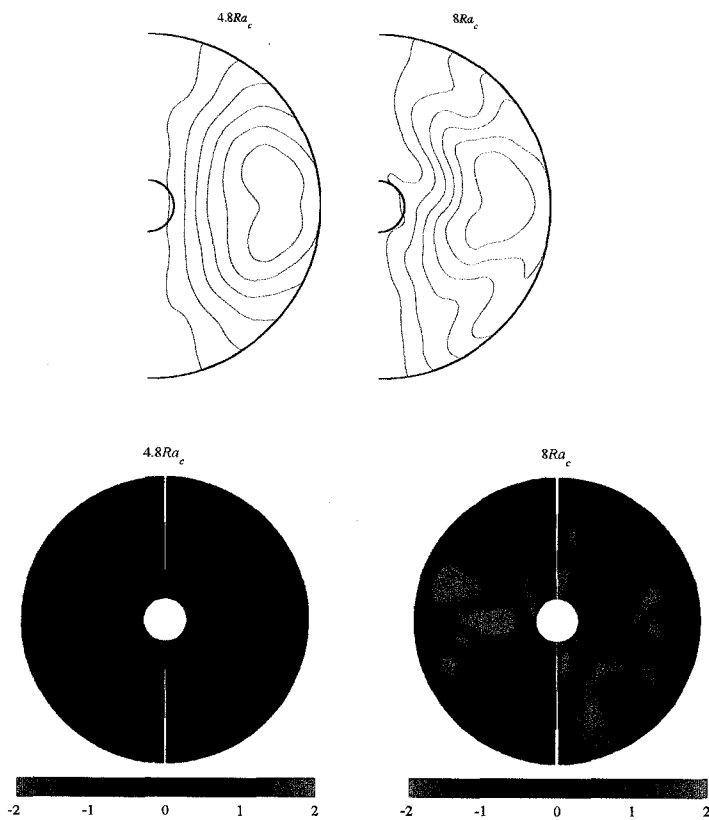
Figure 5.9: On the top row, longitudinal cut of the magnetic poloidal field-lines. Red lines indicate counter-clock wise direction. On the bottom row, radial component of the magnetic field, $B_r$. For both rows, the left panels present results for control 1 and the right hand side panel results for control 2.
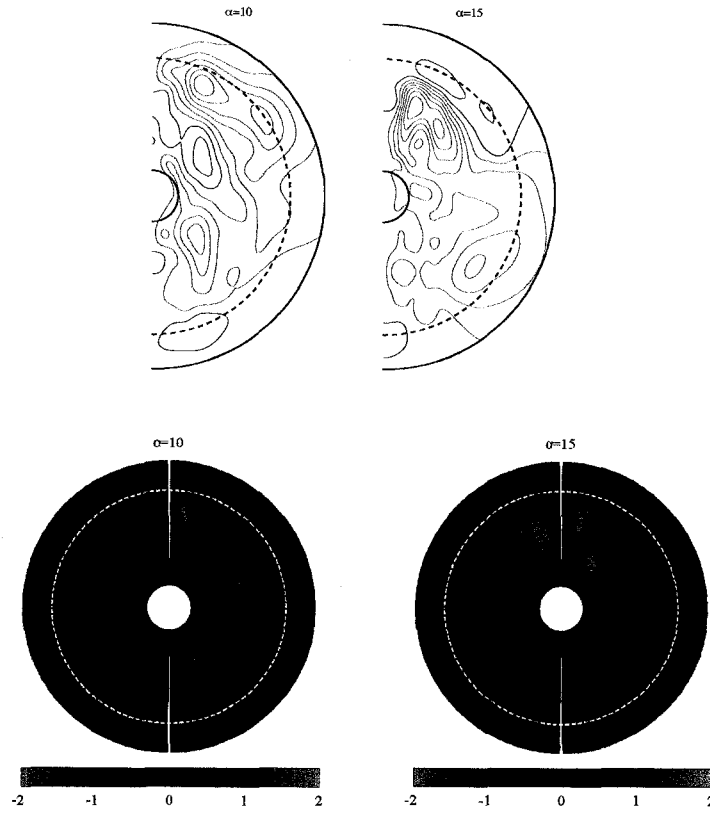
Figure 5.10: Similar to figure 5.9 but for variable conductivity cases. On top: longitudinal cut of the magnetic poloidal field-lines. Red lines indicate counter-clock wise direction and blue clock-wise directions. The sphere of radius $r = r_m$ is marked here with a black dashed line. On the bottom: radial component of the magnetic field $B_r$. On the left $\alpha = 10$, on the right $\alpha = 15$.
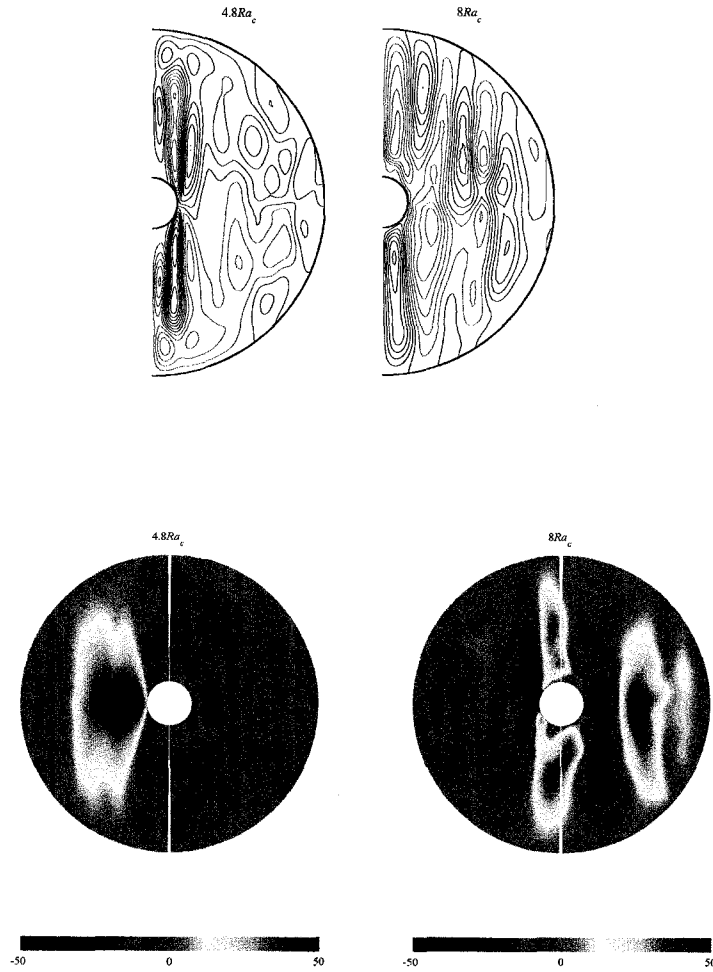
Figure 5.11: Left and right panels present results for controls 1 and 2. Top, longitudinal cut of the poloidal stream-lines. Red lines indicate counter-clock wise, blue clock wise directions. Bottom, radial component of the radial velocity, $u_r$.
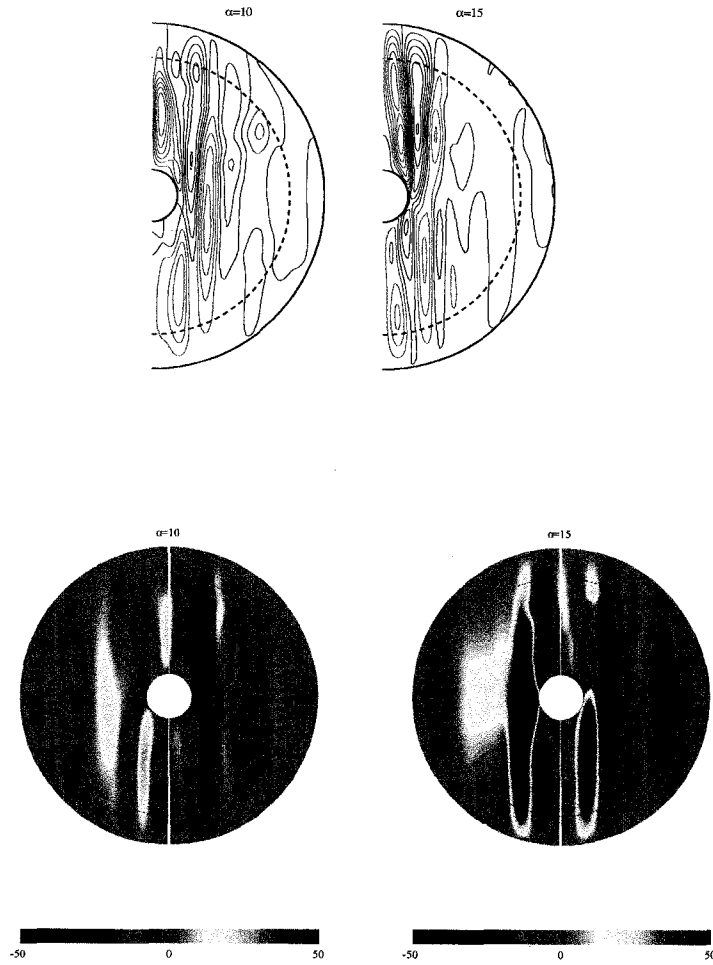
Figure 5.12: (Similar to figure 5.11). Top: longitudinal cut of the poloidal stream-lines. Red lines indicate counter-clock wise and blue clock-wise directions. The sphere of radius $r = r_m$ is marked here with a black dashed line. Bottom: radial component of the velocity field $u_r$. $\alpha = 10$ (left), $\alpha = 15$ (right).

correlation of this fields is seen.

## 5.4 Discussion and conclusions

In this chapter we study the effects of radially variable conductivity model on low Ekman number runs. Using fluid parameters and geometries resembling expectations for planetary interiors, we compare four simulations: two homogeneous electrically conductive liquids with two variable conductivity cases. From preliminary tests using high $E$ (presented in chapter 4), we inferred that, to first order, our variable conductivity models are comparable to low $R_a$ models. In this chapter, we find that for runs with lower $E$, this is not the case.

In chapter 4, relatively low $R_a$ runs suggested that the effect of the variable conductivity may be similar to similar runs using lower $R_a$. We observed great differences between our variable conductivity models and the low $R_a$ control. For rotating convection, the characteristic wave number, $m$, of the temperature field depends on $R_a$, $E$ and $\chi$ (Al-Shamali et al. (2004)). We find $m$ increases from control 1 to control 2. We interpret this increase in $m$ to be caused by the increase in $R_a$. For control 1, the equatorial thermal profile does not present significant convection in the outer part of the simulated fluid. For control 2, temperature is azimuthally heterogeneous over the whole fluid volume (this is possibly due to lack of development of zonal flows in control 2). Variable conductivity cases (see figure 5.3), present higher order $m$ when compared not only to control 1 but also to control 2 (with which they share common $R_a$, $E$, and $\chi$). For these lower Ekman number cases, the electrical conductivity profile does have an effect on the temperature field, and this effect is not directly comparable with effects of lowering $R_a$ which seems to be the case for higher Ekman number runs of chapter 4.

The geometry of the azimuthal velocity field is affected by the variable conductivity. All models develop stronger toroidal flows when compared to poloidal components. Three of the models exhibit equatorial prograde flows at the outer boundary. The averaged surface azimuthal field is similar for the time developed cases (control 1 and the variable conductivity cases), and it is likely that control 2 should reach a similar state. We found significant differences in the magnitude of retrograde jets at the tangent cylinder, being the sole characteristic separating the three models. The vorticity, even though not shown here, presents similar characteristics to those found for the runs of chapter 4 (see figure 4.5). For variable conductivity cases, the vorticity is small close to the outer boundary while for control cases a detachment from the main vorticity column is found.

In contrast to the azimuthal component of the velocity, the magnetic field is strongly affected by the conductivity profile. Even though all the fields are found to be dominantly dipolar, strong multipolar components are found in the variable electrical conductivity models. Geometrical constraints on Lorentz forces yield a complex internal field. The typical length scale of the magnetic field is smaller for both variable conductivity cases than for control 2.

Another interesting characteristic of the magnetic field, found in the variable conductivity models, is that high magnitude fields seem to be constrained to the interior of the tangent cylinder (see figure 5.10). We know from previous chapters, that high magnitude poloidal magnetic fields

avoid zones with azimuthal shear flow, (chapter 3). Since the toroidal kinetic energies found in the variable conductivity models are high, particularly when compared with the magnetic energy, the magnetic fieldlines are pushed toward the poles in order to avoid equatorial flows.

The diffusion of the field in a low conductivity volume results, as expected, in smaller scale features at $r = r_o$ than that at $r = r_m$. The time averaged axisymmetric field at the outer boundary does not distinguish between the two values of $\alpha$ (decay rate) chosen. Differences found between model runs with different $\alpha$ depend on the time the snapshots were taken, more than on a general behaviour of the overall field. In opposition to what we expected from Saturn– for which a highly axisymmetric dipolar field has been observed–the magnetic field is neither more dipolar nor more axisymmetric for the variable electrical conductivity models than for the control cases.

The change in the length scale of both: poloidal velocity and poloidal magnetic field may be understood as a change in the effective non-dimensional numbers. If we take the dynamo region as the volume where the electrical conductivity is significant, we obtain the radius ratio of the dynamo region as $\chi^* = r_i/r_m \sim 0.187$. We may redefine the typical length scale as:

$$D^* = r_m - r_i = \frac{\chi_m - \chi}{1 - \chi} D, \tag{5.1}$$

where $D = 1$. Redefining also the temperature difference across the boundaries as:

$$\Delta T^* = T(r_m) - T(r_i) = \chi_m^{-1} \frac{\chi_m - \chi}{1 - \chi} \Delta T, \tag{5.2}$$

where $\Delta T = 1$. We assume $T(r) - T(r_i) \propto r^{-1}$ for the weakly convective region near the outer boundary (see Kono & Roberts (2001)). For higher $R_a$ the convection is too strong (e.g. figure 4.8) and the azimuthal variations in temperature would not follow equation 5.2. If temperature decreases with radius for $r > r_m$, then using the new normalization, we find the modified non-dimensional parameters:

$$R_a^* = R_a \chi_m^{-1} \left( \frac{\chi_m - \chi}{1 - \chi} \right)^4 \tag{5.3}$$

and

$$E^* = E \left( \frac{1 - \chi}{\chi_m - \chi} \right)^2. \tag{5.4}$$

Calculating the modified non-dimensional parameters for the runs presented in this chapter, we find $\chi^* = 0.187$ and $E^* = 1.7 \times 10^{-4}$, the expected critical azimuthal wavenumber ranges between $2.22 < m_c < 3.14$ (see Al-Shamali et al. (2004)). In contrast, $\chi = 0.15$ and $E = 10^{-4}$ results in $m_c = 2.4$. The azimuthal wavenumber of the variable conductivity models may be partially explained by spatial confinement, i.e. change in a model's typical length scale. Nevertheless, the upper limit of $m_c$ is not sufficient to explain orders 4 and 5 in the thermal equatorial profiles of the variable conductivity models, see bottom row of figure 5.3.

Different initial conditions may result in either strong or weak dynamos, as shown in chapter 2. Under identical parameters low amplitude initial conditions resulted in weak dynamos whereas

high amplitude initial conditions resulted in strong dynamos. The differences in dynamo regimes between control and variable conductivity cases may also be attributed to differences in boundary and initial conditions.

We find then, that if models have weak convection towards the outer boundary (for $r > r_m$), we can treat variable conductivity dynamos approximately as the original homogenous dynamos with $\chi^*$ radius ratios, $E^*$ Ekman numbers and $R_a^*$ Rayleigh numbers. Difficulties in defining boundary and initial conditions, and dependencies on temperature profiles, set apart the variable conductivity from homogenous models.

With parameters studied in this dissertation, all variable electrical conductivity models result in weak dynamos with dipolar and axisymmetric geometries. However, these models are not comparable to the highly axisymmetric fields of Saturn. The lack of strong dynamos for variable electrical conductivity models requires further exploration; testing should explore a large range of non-dimensional parameters. Strong dynamos are expected for higher $P_m$ values, but such models require very long run times. To find dynamos with high magnetic energies it is necessary to increase the effect of the Lorentz force on the fluid. A magnetostrophic balance is likely to yield dipolar fields, as expected for the gas giants.

Even though the magnetic field found for the variable conductivity models is not highly axisymmetric, $m = 0$ orders are dominant. Numerical models of kinematic dynamos with shear layer envelopes result in more axisymmetric fields. By diffusing the magnetic field through axisymmetric shear layers when the underlying geometry is dominantly dipolar, even greater axisymmetry results (see Love (2000), Schubert et al. (2004)). We find that our models yield exclusively axisymmetric dipolar fields, and overlying axisymmetric shear layers are expected to yield more strongly axisymmetric magnetic fields.

In order to increase the contribution of the Lorentz force we could propose simulations with higher values of $P_m$. The main inconvenience with such runs is their high computational cost. This factor poses a major impediment without more numerical code efficiency and advancement in the computational resources.

To better simulate giant planets, we may change the temperature boundary conditions. For all simulations included in this dissertation we assumed constant temperature boundaries. Such boundary conditions yield hot plumes rising from the inner core and thus, the velocity field results in high kinetic energies close to the tangent cylinder (even for relatively low $R_a$). Heimpel et al. (2005a) explains how buoyancy can be produced at the outer boundary by means of secular cooling or internal heating. If cold plumes sink from the outer boundary, then the velocity field may be disturbed where the Lorentz force is intrinsically low. In this case it may be possible that magnetostrophic balances hold for $r < r_m$. If an internal dynamo surrounded by a shear flow results from this model, a highly axisymmetric field would be expected. Runs of this type will require a comparable amount of time to the runs presented in this chapter, and this is feasible with current computational resources.

# Chapter 6

# Conclusions

In this dissertation we have presented numerical models of planetary dynamos. Planetary environments in the solar system may present a variety of behaviours. As we have seen from spacecraft measurements, gas giants, ice giants and terrestrial planets have magnetic fields with very distinct characteristics.

For planetary interiors, the differences amongst length scales for the most significant forces are so great that numerical models are inherently difficult to manage (Jones (2007)). Low viscosity fluids require high resolution grids, and non-dimensional parameters used for numerical models currently cannot reach values expected for planetary interiors. Nevertheless, an asymptotic regime may be reached, where the viscosity is small compared with other forces, but numerical solution algorithms remain stable (Christensen & Aubert (2006)).

In this dissertation, we studied terrestrial planets; how initial conditions and geometry (i.e. inner core size) may affect planetary magnetic fields. We used relatively weakly convecting dynamos (i.e. dynamos with low $R_a$) with different dimensionless parameters to compare aging planets. Numerical simulations require a balance between computation time and resolution. In order to reach the low viscosity regime, higher resolutions, and consequentially longer processing times, are required. We compared data sets with two values of $E$, and found the behaviour to be dependent on the Ekman number.

For younger planets, the magnetic field is generated in a thick shell geometry; the inner core–when present–is small. Older cores present a thin shell geometry such that the flow is restricted to a smaller volume. We found curves for the onset of dynamo action for three different data sets. The Rayleigh number for onset of dynamo action, $R_{a_d}^{pl}$, is found to have a minimum value for intermediate size cores ($0.25 \leq \chi \leq 0.45$). For high values of $E$, thick shells are found to have relatively weakly supercritical $R_{a_d}^{pl}$ compared to low $E$, which resulted in a highly supercritical $R_{a_d}^{pl}$.

The effect of core size on external field geometries is in agreement with Heimpel et al. (2005a). We analysed the radial component of the magnetic field at the outer boundary. We found all our models to be dominantly dipolar; the difference introduced by the core geometry is related to the magnetic field near the poles. Magnetic flux patches change latitude as $\arccos(\chi)$, being

found just outside the tangent cylinder. For low values of $\chi$ (i.e. thick shells), the magnetic field intensity is high at high latitudes. In contrast, for high values of $\chi$, field intensity maxima are found at lower latitudes. If the resolution of the planetary magnetic field measured by spacecrafts is high enough, thin and thick shell geometries may be differentiated using the field geometry.

For aging cores, it is possible to determine the magnitude of the outer field based on the shell thickness. Thick shell models result in strong toroidal field in the fluid core, whereas the poloidal component (that can be measured from outside) is relatively weak by comparison. Thin shell models were found to have kinetic energies comparable with magnetic energies. The poloidal component at the outer shell is also stronger when compared to thick shell models. It is also possible that for extreme values of $\chi$ (probably higher values than those considered in this study), magnetic field intensity decreased due to the restricted volume accessible to support a dynamo (this is only found for one of the data sets, see table 2.1). We expect low Elsasser numbers for thick shells, and possibly for very thin shells as well. Intermediate shell thicknesses are expected to have strong dynamos, agreeing with our knowledge about terrestrial magnetic fields. The Earth sustains a relatively strong magnetic field with an intermediate shell geometry. We conclude that Mercury's weak magnetic field is expected to present either thick or thin shell geometry. Discriminating between these two options may be possible when we have more information about the external field geometry from current space missions (Kabin et al. (2007)).

We studied as well, the magnetic field resulting from weak dynamos (i.e. where magnetic energies are lower than kinetic energies). We used low electrical conductivity dynamos where magnetic field energies resulted about two orders of magnitude lower when compared to kinetic energies. Under the boundary conditions used (i.e. stress free outer boundary) strong toroidal flows were developed. The magnetic forces in the system were small enough to have lesser effects in the flow fields. We found that low Alfvén number dynamos resulted in non-dipolar and highly time variable magnetic fields. We proposed then, that magnetic fields under these conditions display an unusual symmetry due to the force balance. In agreement with Holme & Bloxham (1996), we find that in the ice giants' interiors, a geostrophic balance is more likely to be present rather than the widely accepted magnetostrophic balance in conventional planetary dynamos. Dominantly zonal flows are favoured in a fluid with low electrical conductivity. Such dynamos result in low Elsasser numbers and non-dipolar non-axisymmetric magnetic field geometries as observed for the ice giants.

We later studied the effects of the approximation of a homogeneously electrically conducting fluid, and compared it to a model with radially variable electrical conductivity. Neglecting the change in density (i.e. using the Boussinesq approximation) we introduced slowly radially varying electrical conductivity to numerical simulations. This required modification of the existent dynamo code to introduce consistently a variable electrical conductivity in the dynamics of the system. The main objective of the new implementation was to better model the gas giants. In Jupiter's and Saturn's interior continuous and strong changes in the electrical conductivity and density are expected (e.g. Nellis (2000)).

We found significant effects on the flow field due to the radially decaying electrical conductivity alone. As expected, magnitudes of the magnetic fields at the outer boundary were low due

partly to the diffusion of the magnetic field through the low electrical conductivity zone. The resultant field was more axisymmetric at the outer boundary exclusively as a result of the variable conductivity. Diffusion for higher degree components occurs faster than for the dipolar component ($l = 1$). Thus, dipole dominated fields are expected. Our results for non-slip boundary runs agree with the expectations. In general, when low electrical conductivity envelopes were used, fields appeared to be more dominantly dipolar when compared to the underlying field at $r = r_m$. The set of runs presented in chapter 4 helped us test modifications we made to the numerical code. We found that the new implementation gave reasonable results and provided evidence that the electrical conductivity profile has significant effects on the resultant external field.

In order to analyse further the behaviour of the variable electrical conductivity models, we performed tests with lower values of the Ekman number. The geometry and boundary conditions were chosen to match those expected for planetary interiors. We compared two control models with two variable conductivity models using high resolution grids. We found it difficult to attain dynamos holding a magnetostrophic balance and found that for both variable conductivity models kinetic energies dominated over magnetic energies. While all models were found to be dipolar and axisymmetric, the variable conductivity models had more significant high degree and order contributions than the homogeneous cases. The azimuthal wavenumber was found to be higher for the cases with variable conductivity. This may be a consequence of the variable conductivity defining a thinner shell dynamo with an outer shell of approximately $r_m$. The effective typical length scale, $D^* = r_m - r_i$, of the system is then changed and $R_a$ is modified by both a change in $D^*$ and a reduction in $\Delta T^* = T(r_m) - T(r_i)$. To assume that the sole effect of variable conductivity to simply redefine the radius ratio, the Ekman number and Rayleigh number of the models, is a crude simplification of the problem, but this helps us to understand the system. Nevertheless, we found that variable electrical conductivity models introduce modifications to the dynamics that are not comparable directly with other numerical models (e.g. axisymmetrization, overly increased wavenumbers, presence of significant degree components of magnetic fields), and thus, the modifications we implemented in the magnetic diffusion equation are important for modelling realistically the interior of the gas giants.

Since we do not find Saturn-like magnetic fields in our simulations, we proposed future work that may result in fields similar to those expected in the gas giants. The first option is to increase the electrical conductivity close to the inner core; higher $P_m$ values result in strong dynamos (e.g. Kutzner & Christensen (2002)). The run time of these simulations will increase with $P_m$, and thus become computationally expensive. In addition to increasing $P_m$ to obtain strong dynamos for our variable electrical conductivity models, we proposed as a second option, to change the thermal boundary conditions.

# Bibliography

Acuña, M. H. & Ness, N. F., 1975. Jupiter's magnetic field measured by Pioneer 11, *Nature*, **253**, 327–328.

Acuña, M. H. & Ness, N. F., 1980. Magnetic field of Saturn - pioneer 11 observations, *Science*, **207**, 444–446.

Acuña, M. H., Connerney, J. E. P., Wasilewski, P., Lin, R. P., Anderson, K. A., Carlson, C. W., McFadden, J., Curtis, D. W., Mitchell, D., Reme, H., Mazelle, C., Sauvaud, J. A., d'Uston, C., Cros, A., Medale, J. L., Bauer, S. J., Cloutier, P., Mayhew, M., Winterhalter, D., & Ness, N. F., 1998. Magnetic field and plasma observations at Mars: Initial results of the Mars Global Surveyor Mission, *Science*, **279**, 1676–1680.

Aharonson, O., Zuber, M. T., & Solomon, S. C., 2004. Crustal remanence in an internally magnetized non-uniform shell: a possible source for Mercury's magnetic field?, *Earth Planet. Sci. Lett.*, **281**, 261–268.

Al-Shamali, F., Heimpel, M. H., & Aurnou, J. M., 2004. Varying the spherical shell geometry in rotating thermal convection, *Geophys. Astrophys. Fluid Dyn.*, **98**, 153–169.

Aubert, J., 2005. Steady zonal flows in spherical shell dynamos, *J. Fluid Mech.*, **542**, 53–67.

Aubert, J. & Wicht, J., 2004. Axial vs. equatorial dipolar dynamo models with implications for planetary magnetic fields, *Earth and Planet. Sci. Lett.*, **221**(1-4), 409–419.

Aurnou, J. M. & Heimpel, M. H., 2004. Zonal jets in rotating convection with mixed mechanical boundary conditions, *Icarus*, **169**(2), 492–498.

Aurnou, J. M., Heimpel, M. H., & Wicht, J., 2007. The effects of vigorous mixing in a convective model of zonal flow on the ice giants, *Icarus*, In press.

Barrow, C. H., 1960. Magnetic field of Jupiter, *Nature*, **188**, 924–925.

Braginsky, S. I., 1999. Dynamics of the stably stratified ocean at the top of the core, *Phys. Earth Planet. Int.*, **111**(1-2), 21–34.

Brun, A. S., Browning, M. K., & Toomre, J., 2005. Simulations of core convection in rotating a-type stars: Magnetic dynamo action, *Astrophysical Journal*, **629**, 461 – 481.

Busse, F. H., 1994. Convection driven zonal flows and vortices in the major planets, *Chaos*, **4**(2), 123–134.

Busse, F. H., 2002. Convective flows in rapidly rotating spheres and their dynamo action, *Phys. Fluids*, **14**(4), 1301–1314.

Chandrasekhar, S., 1961. *Hydrodynamic and Hydromagnetic stability*, Dover, New York.

Christensen, U. R. & Aubert, J., 2006. Scaling properties of convection-driven dynamos in rotating spherical shells and aplication to planetary magnetic fields, *Geophys. J. Int.*, **166**, 97–114.

Christensen, U. R., Olson, P., & Glatzmaier, G. A., 1998. A dynamo model interpretation of geomagnetic field structures, *Geophys. Res. Lett.*, **25**, 1565–1568.

Christensen, U. R., Aubert, J., Cardin, P., Dormy, E., Gibbons, S., Glatzmaier, G. A., Grote, E., Honkura, Y., Jones, C., Kono, M., Matsushima, M., Sakuraba, A., Takahashi, F., Tilgner, A., Wicht, J., & Zhang, K., 2001. A numerical dynamo benchmark, *Phys. Earth Planet. Inter.*, **128**, 25–34.

Connerney, J. E. P., 1993. Magnetic-fields of the outer planets, *J. Geophys. Res. - Planets*, **98**(E10), 18659–18679.

Connerney, J. E. P., Acuña, M. H., & Ness, N. F., 1982. Voyager I assesment to Jupiter's planetary magnetic-field, *J. Geophys. Res. - Space Physics*, **87**, 3623–3627.

Connerney, J. E. P., Acuña, M. H., & Ness, N. F., 1987. The magnetic-field of uranus, *J. Geophys. Res. - Space Physics*, **92**(A13), 15329–15336.

Connerney, J. E. P., Acuña, M. H., & Ness, N. F., 1991. The magnetic-field of Neptune, *J. Geophys. Res. - Planets*, **96**, 19023–19042.

Connerney, J. E. P., Acuña, M. H., & Ness, N. F., 1991. The magnetic-field of neptune, *J. Geophys. Res. - Planets*, **96**, 19023–19042.

Connerney, J. E. P., Acuña, Ness, N. F., & Satoh, T., 1998. New models of Jupiter's magnetic field constrained by the Io flux tube footprint, *J. Geophys. Res.*, **103**(A6), 11929–11939.

de Wijs, G., Kresse, G., Vocadlo, L., Dobson, D., Alfe, D., Gillan, M., & Price, G., 1998. The viscosity of liquid iron at the physical conditions of the Earth's core, *Nature*, **392**, 805–807.

Dziewonski, A. M. & Anderson, D. L., 1981. Preliminary earth model, *Phys. Earth Planet. Int.*, **25**(4), 297–356.

Elsasser, W. M., 1956. Hydromagnetic dynamo theory, *Revs. Modern Phys.*, **28**(2), 135–163.

Evonuk, M. & Glatzmaier, G., 2004. 2D studies of various approximations used for modeling convection in giant planets, *Geophys. Astrophys. Fluid Dyn.*, **98**(3), 241–255.

Gibson, R. D., Roberts, P. H., & Scott, S., 1967. *The application of modern physics to the Earth and planetary interiors*, chap. The Bullard-Gellman dynamo, pp. 577–602, no. E II, Wiley–Intersciense, Glasgow, Great Britain.

Gilbert, W., 1600. *De Magnete*, Dover, New York.

Gilman, P. A. & Miller, J., 1981. Dynamically consistent nonlinear dynamos driven by convection in a rotating spherical shell, *Astrophysical Journal Supplement Series*, **46**, 211–238.

Glatzmaier, G., 1984. Numerical simulations of stellar convective dynamos. i. the model and method, *J. Comp. Phys.*, **55**, 461–484.

Glatzmaier, G. & Roberts, P. H., 1995. A three dimensional self-consistent computer simulation of a geomagnetic-field reversal, *Nature*, **377**, 203–209.

Glatzmaier, G., Coe, R., Hongre, L., & Roberts, P. H., 1999. The role of the earth's mantle in controlling the frequency of geomagnetic reversals, *Nature*, **401**, 885–890.

Glatzmaier, G. A., 1985. Numerical simulations of stellar convective dynamos. II. field propagation in the convection zone, *Astrophysical Journal*, **291**(1), 300–307.

Glatzmaier, G. A., 1985. Numerical simulations of stellar convective dynamos. III. at the base of the convection zone, *Geophys. Astrophys. Fluid Dyn.*, **31**(1-2), 137–150.

Glatzmaier, G. A. & Roberts, P. H., 1996. An anelastic evolutionary geodynamo simulation driven by compositional and thermal convection, *Physica D*, **97**(1-3), 81–94.

Gómez-Pérez, N. & Heimpel, M. H., 2007. Numerical models of zonal flow dynamos: An application to the ice giants, *Geophys. Astrophys. Fluid Dyn. - in press*.

Grosser, J., Glassmeier, K.-H., & A., S., 2004. Induced magnetic field effects at planet mercury, *Planet. Space Sci.*, **52**, 1251–1260.

Grote, E., Busse, F. H., & A., T., 2000. Regular and chaotic spherical dynamos, *Phys. Earth Planet. Int.*, **117**, 156–272.

Guillot, T., 1999. A comparison of the interiors of jupiter and saturn, *Planet. Space Sci.*, **47**, 1183–1200.

Guillot, T., 1999. Interiors of giant planets inside and outside the solar system, *Science*, **286**(5437), 72–77.

Guillot, T., 2005. The interiors of giant planets: Models and outstanding questions, *Ann. Rev. Earth Planet. Sci.*, **33**, 493–530.

Guillot, T., Stevenson, D., B., H. W., & Saumon, D., 2004. *Interior of Jupiter*, Cambridge University Press, Cambridge, U.K.

Heimpel, M. H. & Aurnou, J. M., 2007. Turbulent convection in rapidly rotating spherical shells: A model for equatorial and high latitude jets on Jupiter and Saturn, *Icarus*, **187**, 540–557.

Heimpel, M. H., Aurnou, J. M., Al-Shamali, F. M., & Gómez Pérez, N., 2005. A numerical study of dynamo action as a function of spherical shell geometry, *Earth Planet. Sci. Lett.*, **236**(1-2), 542–557.

Heimpel, M. H., Aurnou, J. M., & Wicht, J., 2005. Simulation of an equatorial and high-latitude jets on Jupiter in a deep convection model, *Nature*, **438**, 193–196.

Holme, R., 1997. Three-dimensional kinematic dynamos with equatorial symmetry: Application to the magnetic fields of Uranus and Neptune, *Phys. Earth Planet. Int.*, **102**(1-2), 105–122.

Holme, R. & Bloxham, J., 1996. The magnetic fields of uranus and neptune: Methods and models, *J. Geophys. Res. - Planets*, **101**(E1), 2177–2200.

Hubbard, H. B., Podolak, M., & Stevenson, D. J., 1995. *Neptune and Triton*, Univ. Arizona Press, Tucson, AZ, USA.

Hubbard, W. B. & Marley, M. S., 1989. Optimized Jupiter, Saturn, and Uranus interior models, *Icarus*, **78**(1), 102–118.

Hubbard, W. B., Nellis, W. J., Mitchell, A. C., Holmes, N. C., Limaye, S. S., & McCandless, P. C., 1991. Interior structure of Neptune - comparison with Uranus, *Science*, **253**(5020), 648–651.

Jones, C., 2007. *Encyclopedia of Geomagnetism and Paleomagnetism*, vol. 8, chap. Core Dynamics: Thermal and Compositional Convection in the Outer Core, Springer.

Jones, C., Soward, A., & Mussa, A. I., 2001. The onset of thermal convection in a rapidly rotating sphere, *J. Fluid Mech.*, **405**, 157–179.

Kabin, K., Heimpel, M. H., Rankin, R., Aurnou, J. M., Gómez-Pérez, N., Paral, J., Gombosi, T. I., Zurbuchen, T. H., L., K. P., & DeZeeuw, D. L., 2007. Global MHD modeling of Mercury's magnetosphere with applications to the MESSENGER mission and dynamo theory, Submitted for review to Icarus.

Kageyama, A. & Sato, T., 2004. "Yin-Yang grid": An overset grid in spherical geometry, *Geochemistry Geophysics Geosystems*, **5**(9).

Kageyama, A., Watanabe, K., & Sato, T., 1993. Simulation study of a magnetohydrodynamic dynamo: Convection in a spherical shell, *Phys. Fluids B*, **5**(8), 2793–2805.

Kageyama, A., Sato, T., Watanabe, K., Horiuchi, R., Hayashi, T., Todo, Y., Watanabe, T. H., & Takamaru, H., 1995. Computer simulation of a magnetohydrodynamic dynamo. II, *Phys. Plasmas*, **2**(5), 1421–1431.

Khurana, K. K., Kivelson, M. G., Stevenson, D. J., Schubert, G., Russell, C. T., Walker, R. J., & Polanskey, C., 1998. Induced magnetic fields as evidence for subsurface oceans in Europa and Callisto, *Nature*, **395**, 777–780.

Kono & Roberts, P. H., 2001. Definition of the Rayleigh number for geodynamo simulation, *Phys. Earth Planet. Int.*, **128**, 13–24.

Kuang, W. & Bloxham, J., 1997. An eath-like numerical dynamo model, *Nature*, **389**, 371–374.

Kuang, W. & Bloxham, J., 1999. Numerical modeling of magnetohydrodynamic convection in a rapidly rotating spherical shell: weak and strong field dynamo action, *J. Comp. Phys.*, **153**, 51–81.

Kutzner, C. & Christensen, U. R., 2002. From stable dipolar towards reversing numerical dynamos, *Phys. Earth Planet. Inter.*, **131**, 29–45.

Kutzner, C. & Christensen, U. R., 2004. Simulated geomagnetic reversals and preferred virtual geomagnetic pole paths, *Geophys. J. Int.*, **157**, 1105–1118.

Labrosse, S., Poirier, J., & Mouël, J. L. L., 2001. The age of the inner core, *Earth Planet. Sci. Lett.*, **190**, 111–123.

Lebreton, J. P., Witasse, O., Solazzo, C., Blancquaert, T., Schipper, A. M., Jones, J. B., Matson, D. L., Gurvits, L. I., Atkinson, D. H., Kazeminejad, B., & Pérez Ayucar, M., 2005. An overview of the descent and landing of the Huygens probe to Titan, *Nature*, **438**(8), 758–764.

Love, J. J., 2000. Dynamo action and the nearly axisymmetric magnetic field of saturn, *Geophys. Res. Lett.*, **27**(18), 2889–2892.

Margot, J. L., Peale, S. J., Jurgens, R. F., Slade, M. A., & Holin, I., 2007. Large longitude libration of Mercury reveals a molten core, *Science*, **316**, 710–714.

Matsui, H. & Buffett, B. A., 2005. Sub-grid scale model for convection-driven dynamos in a rotating plane layer, *Phys. Earth Planet. Int.*, **153**(1-3), 108–123.

Matsui, H. & Okuda, H., 2002. Thermal convection analysis in a rotating shell by a parallel finite-element method – development of a thermal-hydraulic subsystem of Geo-FEM, *Concurrency Computat. Pract. Exper.*, **14**, 465–481.

Merrill, R. T., McElhinny, M. W., & McFadden, P. H., 1998. *The Magnetic Field of the earth. Paleomagnetism, the core, and the deep mantle*, Academic Press, San Diego, CA. U.S.A.

Nellis, W. J., 2000. Metallization of fluid hydrogen at 140GPa (1.4Mbar): implications for Jupiter, *Planet. Space Sci.*, **48**, 671–677.

Nellis, W. J., 2006. Dynamic compression of materials: metallization of fluid hydrogen at high pressures, *Rep. Prog. Phys.*, **69**(5), 1479–1580.

Nellis, W. J., Holmes, N. C., Mitchell, A. C., Hamilton, D. C., & Nicol, M., 1997. Equation of state and electrical conductivity of "synthetic Uranus," a mixture of water, ammonia, and isopropanol, at shock pressure up to 200 GPa (2 Mbar), *Journal of Chemical Physics*, **107**(21), 9096–9100.

Ness, N. F., Behannon, W., & Lepping, R. P., 1976. Observations of Mercury's magnetic field, *Icarus*, **28**, 479–488.

Ness, N. F., Acuña, M. H., Lepping, R. P., Burgala, L. F., Behannon, K. W., & Neubauer, F. M., 1979. Magnetic-field studies at Jupiter by Voyager II - preliminary results, *Science*, **206**(4421), 966–972.

Ness, N. F., Acuña, M. H., Lepping, R. P., Connerney, J. E. P., Behannon, K. W., Burgala, L. F., & Neubauer, F. M., 1981. Magnetic field studies by Voyager I - preliminary results at Saturn, *Science*, **212**, 211–217.

Ness, N. F., Acuña, M. H., Behannon, K. W., Burgala, L. F., Connerney, J. E. P., Lepping, R. P., & Neubauer, F. M., 1982. Magnetic field studies by Voyager II - preliminary results at Saturn, *Science*, **215**, 558–562.

Ness, N. F., Acuña, M. H., Behannon, K. W., Burlaga, L. F., Connerney, J. E. P., Lepping, R. P., & Neubauer, F. M., 1986. Magnetic-fields at uranus, *Science*, **233**(4759), 85–89.

Ness, N. F., Acuña, M. H., Burlaga, L. F., Connerney, J. E. P., Lepping, R. P., & Neubauer, F. M., 1989. Magnetic-fields at neptune, *Science*, **246**(4736), 1473–1478.

Niemann, H. B., Atreya, S. K., Carignan, G. R., Donahue, T. M., Haberman, J. A., Harpold, D. N., Hartle, R. E., Hunten, D. M., Kasprzak, W. T., Mahaffy, P. R., Owen, T. C., Spencer, N. W., & Stanley, H. W., 1996. The Galileo, Probe Mass Spectrometer: Composition of Jupiter's atmosphere, *Science*, **272**, 846–849.

Olson, P. & Christensen, U. R., 2006. Dipole moment scaling for convection-driven planetary dynamos, *Earth Planet. Sci. Lett.*, **205**(3-4), 561–571.

Podolak, M., Hubbard, H. B., & Stevenson, D. J., 1991. *Uranus*, Univ. Arizona Press, Tucson, AZ, USA.

Podolak, M., Podolak, J. I., & Marley, M. S., 2000. Further investigations of random models of Uranus and Neptune, *Planet. Space Sci.*, **48**(2-3), 143–151.

Rogers, T., Glatzmaier, G., & Woosley, S. E., 2003. Simulations of two-dimensional turbulent convection in a density-stratified fluid, *Phys. Rev. E*, **67**(026315), 1–6.

Schubert, G., Chan, K. H., Liao, X., & Zhang, K., 2004. Planetary dynamos: effects of electrically conducting flows overlying turbulent regions of magnetic field generation, *Icarus*, **172**, 305–315.

Spohn, T., Sohl, F., Wieczerkowski, K., & Conzelmann, V., 2001. The interior structure of Mercury: what we know, what we expect from BepiColombo, *Planet. Space Sci.*, **49**, 1561–1570.

Stanley, S. & Bloxham, J., 2004. Convective-region geometry as the cause of Uranus' and Neptune's unusual magnetic field, *Nature*, **428**, 151–153.

Stanley, S. & Bloxham, J., 2006. Numerical dynamo models of Uranus' and Neptune' magnetic fields, *Icarus*, **184**, 556–572.

Starchenko, S. V. & Jones, C., 2002. Typical velocities and magnetic field strengths in planetary interiors, *Icarus*, **157**, 426–435.

Stevenson, D. J., 1982. Interior of the giant planets, *Ann. Rev. Earth Planet. Sci.*, **10**, 257–295.

Stevenson, D. J., 1987. Mercury's magnetic field: a thermoelectric dynamo?, *Earth Planet. Sci. Lett.*, **82**, 114–120.

Stevenson, D. J., 2003. Planetary magnetic fields, *Earth and Planetary Science Letters*, **208**(1-2), 1–11.

Wicht, J., 2002. Inner-core conductivity in numerical dynamo simulations, *Phys. Earth. Planet. Inter.*, **132**, 281–302.

Zhang, K. & Schubert, G., 2006. Comparison of terrestrial and solar dynamos, *Rep. Prog. Phys.*, **69**, 1581–1605.

# Appendix A

# Dynamo Problem

The dynamo theory explains the planetary magnetic field as generated by an electrically conductive, convective, and rotating fluid. The system consists of a fluid enclosed between two spherical shells rotating with an angular velocity $\Omega$. The fluid is electrically conductive and viscous. In order to determine the motion of the fluid and if a magnetic field may be sustained by this motion, we need to write equations of motion, conservation of energy, and conservation of momentum.

## A.1  Navier-Stokes equation

We can write the equation of motion of the system as $\mathbf{F} = m\mathbf{a}$. For a fluid, it is more convenient to express the forces as the force per unit volume, that is $\mathbf{f} = \frac{\mathbf{F}}{\Delta V} = \rho\mathbf{a}$, where $\rho$ is the density of the fluid. The dynamics of the system is determined by the forces acting on it. For the dynamo problem these are

$$\mathbf{f} = -\nabla p - \rho\nabla\phi_g - \mathbf{f}^{vis} - \mathbf{f}^b + \mathbf{f}^c + \mathbf{f}^m, \tag{A.1}$$

where the first and second term are the forces due to the pressure gradient and the force of gravity respectively. $\mathbf{f}^{vis}$ is the viscous force; this term is expected to be very small compared to all the other forces, but it is also very important for the stability of numerical solutions. $\mathbf{f}^b$ is the buoyancy force; it determines the convective force in the fluid. $\mathbf{f}^c$ is the Coriolis force; we choose the rotating frame of reference and thus this force needs to be included. And lastly, $\mathbf{f}^m$ is the Lorentz force; there is a magnetic force exerted on the a flow carrying currents. Since the fluid is electrically conductive if there are electrical currents in the system the flow should be also be affected by the Lorentz force. Given that each term in equation A.1 requires some explanation, we treat them separately.

### A.1.1  Viscous force

For convenience, the derivation of the viscous force will be developed on cartesian coordinates. We will use this derivation and apply the resultant vectorial expression to spherical coordinates. The stress tensor is defined as $\partial_j\pi_{ij} = f_i^{vis}$, where $f_i^{vis}$ is the $i$th component of $\mathbf{f}^{vis}$, and $\partial_j$ is

the covariant derivative in the direction $\hat{\mathbf{e}}_j$, which corresponds to the unitary vector that defines the coordinate system. The stress tensor may be expressed as,

$$\pi_{ij} = \eta\left(\partial_j u_i + \partial_i u_j\right) + \mu_b(\nabla \cdot \mathbf{u})\delta_{ij}, \tag{A.2}$$

where $\eta$ is the dynamic viscosity, and $\mu_b$ is the bulk viscosity. $\mathbf{u}$ is the velocity vector, and $u_i$ is the $i$th component of $\mathbf{u}$. Thus, $i$th component of the viscous force per unit volume,

$$
\begin{aligned}
f_i^{vis} &= \partial_j(\eta\left(\partial_j u_i + \partial_i u_j\right)) + \partial_j\left(\mu_b(\nabla \cdot \mathbf{u})\delta_{ij}\right) \\
&= (\partial_j\eta)(\partial_j u_i) + \eta(\partial_j\partial_j u_i) + (\partial_j\eta)(\partial_i u_j) + \eta(\partial_j\partial_i u_j) + \partial_j\left(\mu_b(\nabla \cdot \mathbf{u})\delta_{ij}\right),
\end{aligned}
$$

from where

$$
\begin{aligned}
\mathbf{f}^{vis} &= (\nabla\eta \cdot \nabla)\mathbf{u} + \eta\nabla^2\mathbf{u} + \nabla(\mathbf{u} \cdot \nabla\eta) + \eta\nabla(\nabla \cdot \mathbf{u}) + \nabla(\mu_b(\nabla \cdot \mathbf{u})) \tag{A.3} \\
&= \eta\nabla^2\mathbf{u} + (\eta + \mu_b)\nabla(\nabla \cdot \mathbf{u}). \tag{A.4}
\end{aligned}
$$

Where we assume the viscosities, $\eta$ and $\mu_b$, to be constant as function of space.

## A.1.2 Compositional convection

The buoyancy force per unit volume may be expressed as $\mathbf{f}^b = (\delta\rho)\,g$. Using thermodynamic equations one may find an expression for $\delta\rho$.

The thermal expansion coefficient, $\alpha$ is defined as

$$\alpha = \frac{-1}{\rho}\left.\frac{\partial\rho}{\partial T}\right|_P, \tag{A.5}$$

where $T$ is temperature and $P$ is pressure. Thus, we can, for a constant pressure, write

$$\int_{T_{ref}}^{T} -\alpha\rho\,dT' = \int_{T_{ref}}^{T} \frac{\partial\rho}{\partial T'}\,dT', \tag{A.6}$$

where $T_{ref}$ is the equilibrium state of temperature for which $\rho(T_{ref}) = \rho_o$. If the deviation of $T$ from the reference state $(T_{ref})$ is small,

$$-\alpha\rho\delta T = \rho(T) - \rho(T_{ref}) = \delta\rho. \tag{A.7}$$

It is convenient to write the temperature as the temperature difference from the equilibrium state, $T_{ref}$, and thus we write $\delta T$ as the temperature $T$. We find then

$$\mathbf{f}^b = -\alpha\rho\,T\,\mathbf{g}. \tag{A.8}$$

## A.1.3 Coriolis force

We have chosen the rotating frame of reference. For a system with an angular velocity $\Omega$, where we choose the $z$-axis to be aligned with the axis of rotation. The Coriolis force is expressed as $\mathbf{F}^c = -2m(\Omega \times \mathbf{u})$. The force per unit volume is then

$$\mathbf{f}^c = -2\rho(\Omega \times \mathbf{u}). \tag{A.9}$$

## A.1.4 Lorentz Force

The electrical conductivity of the fluid allows for the flow to be modified by magnetic fields. The force exerted by a magnetic field $\mathbf{B}$, on a body carrying a current $\mathbf{J}$ is $\mathbf{F}^m = \mathbf{J} \times \mathbf{B}$. Using the density current $\mathbf{j}$, the force per unit volume is

$$\mathbf{f}^m = \mathbf{j} \times \mathbf{B} = \mu^{-1}(\nabla \times \mathbf{B}) \times \mathbf{B}, \tag{A.10}$$

where $\mu$ is the magnetic permeability.

Once we have found all the forces for the equation of motion, we can express the acceleration of the system as

$$
\begin{aligned}
\rho\mathbf{a} \;=\; & -\nabla p - \rho\nabla\phi + \eta\nabla^2\mathbf{u} + (\eta + \mu_b)\nabla(\nabla \cdot \mathbf{u}) + \alpha\rho T\mathbf{g} \\
& -2\rho(\Omega \times \mathbf{u}) + \mu^{-1}(\nabla \times \mathbf{B}) \times \mathbf{B}.
\end{aligned} \tag{A.11}
$$

## A.1.5 Normalization

In order to use numerical solutions, it is convenient to use non-dimensional parameters. In addition, the adimensionalization of the equations allows for a easier analysis of the flow when one wants to compare with experimental results and with measurements from planetary environments. We choose the non-dimensional time as the viscous diffusion time, $\tau_\nu = D^2\nu^{-1}$, where $D$ is the thickness of the shell containing the fluid. $\nu = \eta/\rho$ is the kinematic viscosity. Given the external and internal radii of the shell, $r_i$ and $r_o$, we define the radius ratio as

$$\chi = r_i/r_o.$$

We choose to use $D$ as our normalized length thus $r_o - r_i = 1$. This yields a normalized $r_o = (1 - \chi)^{-1}$ and $r_i = \chi(1 - \chi)^{-1}$.

To make non-dimensional equation A.11, we start with the acceleration, the net force:

$$\rho\mathbf{a} \;=\; \rho\frac{D}{(D^2\nu^{-1})^2}\tilde{\mathbf{a}} \tag{A.12}$$

$$\;=\; \frac{\rho\nu^2}{D^3}\tilde{\mathbf{a}} \tag{A.13}$$

$$\;=\; \frac{\nu}{\Omega D^2}\frac{\rho\nu\Omega}{D}\tilde{\mathbf{a}} \tag{A.14}$$

$$= \frac{\rho\nu\Omega}{D} E\tilde{\mathbf{a}}, \tag{A.15}$$

where $E$ is the Ekman number. Now, we normalize every term in equation A.11 and multiply each term by $\frac{D}{\rho\nu\Omega}$. For the pressure gradient and the gravity we write an expression that includes all the terms that my be expressed as a potential (conservative forces).

$$\tilde{\nabla}\tilde{P} = (\nabla p + \rho\nabla\phi)\frac{D}{\rho\nu\Omega}. \tag{A.16}$$

The viscous force term,

$$\frac{D}{\rho\nu\Omega}(\eta\nabla^2\mathbf{u} + (\eta + \mu_b)\nabla(\nabla\cdot\mathbf{u})) \tag{A.17}$$

$$= \frac{D}{\rho\nu\Omega}\frac{\nu}{D^3}(\eta\tilde{\nabla}^2\tilde{\mathbf{u}} + (\eta + \mu_b)\tilde{\nabla}(\tilde{\nabla}\cdot\tilde{\mathbf{u}})) \tag{A.18}$$

$$= \frac{\eta}{\rho\Omega D^2}\tilde{\nabla}^2\tilde{\mathbf{u}} + \frac{\eta + \mu_b}{\rho\Omega D^2}\tilde{\nabla}(\tilde{\nabla}\cdot\tilde{\mathbf{u}}) \tag{A.19}$$

$$= E\tilde{\nabla}^2\tilde{\mathbf{u}} + \frac{\eta + \mu_b}{\rho\Omega D^2}\tilde{\nabla}(\tilde{\nabla}\cdot\tilde{\mathbf{u}}). \tag{A.20}$$

The buoyancy term,

$$(\alpha\rho T\,\mathbf{g})\frac{D}{\rho\nu\Omega} \tag{A.21}$$

$$= \frac{D\alpha\Delta T g_o}{\nu\Omega}\tilde{T}\tilde{g}\hat{\mathbf{r}} \tag{A.22}$$

$$= \frac{\alpha g_o\Delta T D}{\nu}\frac{1}{\Omega}\tilde{T}\tilde{g}\hat{\mathbf{r}} \tag{A.23}$$

$$= \frac{\alpha g_o\Delta T D^3}{\nu\kappa}\frac{\kappa}{D^2}\frac{1}{\Omega}\tilde{T}\tilde{g}\hat{\mathbf{r}} \tag{A.24}$$

$$= R_a\frac{\kappa}{\nu}\frac{\nu}{D^2\Omega}\tilde{T}\tilde{g}\hat{\mathbf{r}} \tag{A.25}$$

$$= R_a P_r^{-1} E\tilde{T}\tilde{g}\hat{\mathbf{r}}, \tag{A.26}$$

where the temperature has been normalized in terms of $\Delta T$, the temperature difference between the outer and inner shells; and gravity by $g_o$, the gravity at the outer shell. We have also introduced here the Rayleigh number $R_a = \alpha g_o\Delta T D^3/(\nu\kappa)$, and the Prandtl number $P_r = \nu\kappa^{-1}$.

The Coriolis term,

$$2\rho(\mathbf{\Omega}\times\mathbf{u})\frac{D}{\rho\nu\Omega} = 2(\hat{\mathbf{z}}\times\mathbf{u}\frac{D}{\nu}) = 2(\hat{\mathbf{z}}\times\tilde{\mathbf{u}}). \tag{A.27}$$

And lastly, the term for the Lorentz force.

$$\frac{D}{\rho\nu\Omega}\mu^{-1}(\nabla\times\mathbf{B})\times\mathbf{B} = \frac{1}{\rho\mu\lambda\Omega}\frac{\lambda}{\nu}(\tilde{\nabla}\times\mathbf{B})\times\mathbf{B} = P_m^{-1}(\tilde{\nabla}\times\tilde{\mathbf{B}})\times\tilde{\mathbf{B}}, \tag{A.28}$$

where $\lambda$ is the magnetic diffusivity, and the magnetic field is normalized using $\mathbf{B} = \sqrt{\rho\mu\lambda\Omega}\,\tilde{\mathbf{B}}$. $P_m = \frac{\nu}{\lambda}$ is the magnetic Prandtl number.

Thus, the non-dimensional Navier-Stokes equation is:

$$E(\tilde{\mathbf{a}} - \tilde{\nabla}^2\tilde{\mathbf{u}}) \quad - \quad \frac{\eta + \mu_b}{\rho\Omega D^2}\tilde{\nabla}(\tilde{\nabla}\cdot\tilde{\mathbf{u}}) + 2(\hat{\mathbf{z}}\times\tilde{\mathbf{u}})$$

$$= \quad -\tilde{\nabla}\tilde{P} + R_a P_r^{-1} E\tilde{T}\tilde{g}\hat{\mathbf{r}} + P_m^{-1}(\tilde{\nabla}\times\tilde{\mathbf{B}})\times\tilde{\mathbf{B}}. \tag{A.29}$$

## A.2 Heat equation

The equation of conservation of energy is the heat equation. As we did previously we take the temperature $T$ as the temperature difference from a reference state. The reference state in this case is the adiabat as a function of pressure (which changes with radius exclusively). Once this reference state is chosen, one may write the energy conservation equation

$$\frac{\partial T}{\partial t} = \kappa\nabla^2 T + (\nabla\kappa\cdot\nabla T) - \mathbf{u}\cdot\nabla T + \varepsilon, \tag{A.30}$$

where $\kappa$ is the thermal diffusivity; and $\varepsilon$ is an external heat source, such as heat from radioactive elements in the core. This equation may also become non-dimensional. Normalizing, as done previously, length, temperature and time ($\nabla = D^{-1}\tilde{\nabla}$, $T = (\Delta T)\tilde{T}$, and $t = D^2\nu^{-1}\tilde{t}$ respectively),

$$\frac{\partial\tilde{T}}{\partial\tilde{t}}D^{-2}\nu = \kappa D^{-2}\tilde{\nabla}^2\tilde{T} - D^{-2}\nu\tilde{\mathbf{u}}\cdot\tilde{\nabla}\tilde{T} + \frac{\varepsilon}{\Delta T}, \tag{A.31}$$

from where,

$$\frac{\partial\tilde{T}}{\partial\tilde{t}} = \frac{\kappa}{\nu}\tilde{\nabla}^2\tilde{T} - \tilde{\mathbf{u}}\cdot\tilde{\nabla}\tilde{T} + \frac{\varepsilon D^2}{\Delta T\nu} \tag{A.32}$$

$$= P_r^{-1}\tilde{\nabla}^2\tilde{T} - \tilde{\mathbf{u}}\cdot\tilde{\nabla}\tilde{T} + \tilde{\varepsilon} \tag{A.33}$$

defining $\tilde{\varepsilon} = \frac{\varepsilon D^2}{\Delta T\nu}$ as a normalized heat source.

## A.3 Maxwell's equations

Electric and magnetic field are governed by a set of four equations,

$$\nabla\times\mathbf{H} = \mathbf{J} + \frac{\partial\mathbf{D}}{\partial t}, \tag{A.34}$$

$$\nabla\times\mathbf{E} = -\frac{\partial\mathbf{B}}{\partial t}, \tag{A.35}$$

$$\nabla\cdot\mathbf{B} = 0, \tag{A.36}$$

$$\nabla\cdot\mathbf{E} = \rho_e. \tag{A.37}$$

where $\mathbf{H}$ is the magnetic field vector, $\mathbf{D}$ is the electric displacement vector, $\mathbf{B}$ is the magnetic induction vector, $\mathbf{E}$ is the electric field vector, and $\rho_e$ is the charge density.

## A.3.1 Electrical current

To understand the behaviour of the charged particles under an electric field some careful considerations need to be taken into account. The drift velocity for an electron with charge $q_e$ in presence of an electric field $|\mathbf{E}|$ follows:

$$m_e \left( \frac{\mathrm{d}u_d}{\mathrm{d}t} + k\,u_d \right) = q_e |\mathbf{E}|, \tag{A.38}$$

where $m_e$ is the mass of the electron, $u_d$ is the drift velocity, $t$ is time, and $k$ is a constant where $m_e k\,u_d$ is the friction force due to collisions with other electrons. The solution of this equation is

$$u_d(t) = u_o e^{-kt} + \frac{q_e |\mathbf{E}|}{k\,m_e}. \tag{A.39}$$

For the steady state ($kt \to \infty$) the current then becomes

$$\mathbf{J} = N q_e \mathbf{u}_d = \frac{N q_e^2 \mathbf{E}}{k\,m_e} = \sigma \mathbf{E}, \tag{A.40}$$

where $N$ is the number of electrons, and $\sigma$ is defined as the electrical conductivity. Equation A.40 is known as Ohm's law, and it is found for the steady state current. The steady state then requires $t \gg \tau$, where $\tau = k^{-1}$ is the relaxation time, and $k$ represents the collision frequency.

Given a time dependent electric field $\mathbf{E}(t)$, where the field changes with a frequency $\nu_E$, there are two extreme scenarios. First, if $\nu_E \gg k$ the steady state may not be attained and the electrons move with the electric field causing charge separation. Second, if $\nu_E \ll k$ the steady state may be attained and the electrons follow Ohm's law. For the latter case, $\frac{\partial \mathbf{E}}{\partial t} \approx 0$, and thus $\frac{\partial \mathbf{D}}{\partial t} \approx 0$. The second case mentioned here is denominated the MHD approximation. Merrill et al. (1998) suggest that the charge separation may occur at pressures greater than about $10^{12}$Pa, which is an order of magnitude higher than the pressure at the centre of the Earth (of the order of $10^{11}$Pa). In the case of Jupiter though, the estimated pressure close to the centre is on the order of $10^{12}$ (e.g. Guillot (2005)) and thus the MHD approximation may be invalid for the very deep interior of the Jovian planet.

To define the dynamo equations we use Ohm's law:

$$\begin{aligned} \mathbf{J} &= \sigma\left(\mathbf{E} + (\mathbf{u} \times \mathbf{B})\right) \\ \mu\lambda\mathbf{J} &= \mathbf{E} + (\mathbf{u} \times \mathbf{B}), \end{aligned} \tag{A.41}$$

Where $\mathbf{J}$ is the current, $\sigma$ is the electrical conductivity, $\mathbf{E}$, $\mathbf{u}$ and $\mathbf{B}$ are the electric field, velocity and magnetic induction vectors, $\mu$ is the magnetic permeability and $\lambda$ is the magnetic diffusivity which is related to the conductivity as $\lambda = \frac{1}{\mu\sigma}$.

Taking the curl of equation A.41, and using Faraday's Law, ($\nabla \times \mathbf{E} = -\partial_t \mathbf{B}$), an expression for the time derivative of the magnetic induction vector may be found:

$$\nabla \times \mu\lambda\mathbf{J} = \nabla \times (\mathbf{E} + (\mathbf{u} \times \mathbf{B}))$$

$$= -\frac{\partial \mathbf{B}}{\partial t} + \nabla \times (\mathbf{u} \times \mathbf{B}). \qquad (A.42)$$

Using Ampere's law, the curl of the current may be expressed as:

$$\mathbf{J}\mu = \left(\nabla \times \mathbf{B} - \frac{\partial \mathbf{D}}{\partial t}\right)$$

$$\nabla \times \mu\lambda\mathbf{J} = \nabla \times \lambda\left(\nabla \times \mathbf{B} - \frac{\partial \mathbf{D}}{\partial t}\right), \qquad (A.43)$$

Taking the right hand side of equations A.42 and A.43, the magnetic induction time derivative can be expressed as,

$$\frac{\partial \mathbf{B}}{\partial t} = -\nabla \times \lambda(\nabla \times \mathbf{B}) + \nabla \times \lambda\frac{\partial \mathbf{D}}{\partial t} + \nabla \times (\mathbf{u} \times \mathbf{B}). \qquad (A.44)$$

Using the MHD approximation,

$$\frac{\partial \mathbf{B}}{\partial t} = -\nabla \times \lambda(\nabla \times \mathbf{B}) + \nabla \times (\mathbf{u} \times \mathbf{B}). \qquad (A.45)$$

The previously proposed normalization yields

$$\frac{\partial \tilde{\mathbf{B}}}{\partial \tilde{t}} = -\nu^{-1}\tilde{\nabla} \times \lambda(\tilde{\nabla} \times \tilde{\mathbf{B}}) + \tilde{\nabla} \times (\tilde{\mathbf{u}} \times \tilde{\mathbf{B}}). \qquad (A.46)$$

If the magnetic diffusivity, $\lambda$ is constant in space, and using $\nabla \times (\nabla \times \mathbf{B}) = -\nabla^2\mathbf{B}$

$$\frac{\partial \tilde{\mathbf{B}}}{\partial \tilde{t}} = P_m^{-1}\tilde{\nabla}^2\tilde{\mathbf{B}} + \tilde{\nabla} \times (\tilde{\mathbf{u}} \times \tilde{\mathbf{B}}). \qquad (A.47)$$

## A.4 The dynamo equations

The equations of motion, energy conservation, as well as the equation for the time derivative of the magnetic induction vector have been derived in this appendix. We used the MHD approximation to obtain equation A.47.

In order to use the spectral solutions proposed in Glatzmaier (1984), vectors should be divergence free, $\nabla \cdot \mathbf{a} = 0$. If this is true,

$$\mathbf{a} = \nabla \times \nabla \times a_p\hat{\mathbf{r}} + \nabla \times a_t\hat{\mathbf{r}}, \qquad (A.48)$$

where $a_t$ is the toroidal potential, and $a_p$ is the poloidal potential (Chandrasekhar (1961)). For the case of the magnetic induction vector, this is true since the non-existence of magnetic monopoles yields directly to $\nabla \cdot \mathbf{B} = 0$. The magnetic field induction then, may be written as two,

toroidal and poloidal, potentials instead of three independent components. For the velocity field, this task becomes a little more complicated. The divergence of the velocity field is determined by the equation of conservation of mass,

$$\frac{\partial \rho}{\partial t} = \nabla \cdot (\rho \mathbf{u}). \tag{A.49}$$

For dynamo models where the density is believed not to change significantly with respect to time or space, the *Boussinesq* approximation is used (that is $\nabla \cdot \mathbf{u} = 0$). Since it is the approximation used for the modelling presented in this dissertation, we will only present the equations using this approximation. The relevance and a brief discussion on whether or not it is reasonable to use this approximation is included in section 4.1.1, where the discussion about the giant planets' interior requires a close examination of the equation of conservation of mass.

In summary, the complete set of normalized Boussinesq, MHD equations:

$$E(\tilde{\mathbf{a}} - \tilde{\nabla}^2 \tilde{\mathbf{u}}) + 2(\hat{\mathbf{z}} \times \tilde{\mathbf{u}})$$
$$= -\tilde{\nabla}\tilde{P} + R_a P_r^{-1} E \tilde{T} \tilde{g} \hat{\mathbf{r}} + P_m^{-1}(\tilde{\nabla} \times \tilde{\mathbf{B}}) \times \tilde{\mathbf{B}}, \tag{A.50}$$

$$\frac{\partial \tilde{T}}{\partial \tilde{t}} = P_r^{-1} \tilde{\nabla}^2 \tilde{T} - \tilde{\mathbf{u}} \cdot \tilde{\nabla}\tilde{T} + \tilde{\varepsilon}, \tag{A.51}$$

$$\frac{\partial \tilde{\mathbf{B}}}{\partial \tilde{t}} = P_m^{-1} \tilde{\nabla}^2 \tilde{\mathbf{B}} + \tilde{\nabla} \times (\tilde{\mathbf{u}} \times \tilde{\mathbf{B}}). \tag{A.52}$$

Note that $\tilde{\mathbf{a}} = \frac{d\tilde{\mathbf{u}}}{d\tilde{t}} = \frac{\partial \tilde{\mathbf{u}}}{\partial \tilde{t}} + (\tilde{\mathbf{u}} \cdot \nabla)\tilde{\mathbf{u}}$.

# Appendix B

# Magnetic field outside the dynamo region

The poloidal magnetic field at the outer boundary determines uniquely the magnetic field away from the dynamo region. In contrast, the toroidal component cannot be determined from outside, and does not affect the outside field. To determine the interaction with the solar wind or the magnetic field at the planetary surface, it is necessary to calculate the field far from the dynamo region. If we assume that the mantle and/or clouds are not electrically conductive and that there are no external fields, the magnetic field outside may be expressed as function of a potential. In this appendix, we present the expression of the magnetic field outside (assuming no magnetic or electric field sources outside the dynamo region) in terms of the poloidal magnetic potential $b$, defined in equation 4.5.

## B.1 Magnetic field vector outside the dynamo region

To define the field outside the dynamo region one needs to solve the Laplacian of a potential where

$$\nabla \phi = \mathbf{B}. \tag{B.1}$$

The potential may be expressed in terms of a sum of complete ortho-normal functions,

$$\phi(r, \theta, \varphi) = \sum_{l=0}^{\infty} \sum_{m=0}^{l} \left(\frac{R}{r}\right)^{l+1} P_l^m(\cos \theta) \left[\alpha_l^m e^{im\varphi} + \beta_l^m e^{-im\varphi}\right]. \tag{B.2}$$

From equation B.1 we find,

$$B_r = -\frac{\partial \phi}{\partial r}, \qquad \text{(B.3)} \qquad B_\theta = -\frac{1}{r}\frac{\partial \phi}{\partial \theta}, \qquad \text{(B.4)} \qquad B_\varphi = -\frac{1}{r \sin \theta}\frac{\partial \phi}{\partial \varphi}. \tag{B.5}$$

And thus, **B** may be expressed in terms of sums as well,

$$\frac{\partial \phi}{\partial r} = \sum_l \sum_m -(l+1)\frac{R^{l+1}}{r^{l+2}} P_l^m(\cos\theta) \left[\alpha_l^m e^{im\varphi} + \beta_l^m e^{-im\varphi}\right]. \tag{B.6}$$

$$\frac{1}{r}\frac{\partial \phi}{\partial \theta} = \sum_l \sum_m \frac{R^{l+1}}{r^{l+2}} \frac{\partial P_l^m(\cos\theta)}{\partial\theta} \left[\alpha_l^m e^{im\varphi} + \beta_l^m e^{-im\varphi}\right]. \tag{B.7}$$

$$\frac{1}{r\sin\theta}\frac{\partial \phi}{\partial \varphi} = \sum_l \sum_m \frac{R^{l+1}}{r^{l+2}} \frac{im}{\sin\theta} P_l^m(\cos\theta) \left[\alpha_l^m e^{im\varphi} - \beta_l^m e^{-im\varphi}\right]. \tag{B.8}$$

In order to use the Legendre and Fourier expansions in equation B.7, it is convenient to express the derivative of the Legendre polynomial in terms of the polynomial themselves. For the axisymmetric part ($m = 0$)

$$P_n'(x)(1 - x^2) = nP_{n-1}(x) - nxP_n(x). \tag{B.9}$$

Note that $P_n'(x) = \frac{\partial P_n(x)}{\partial x} = \frac{\partial P_n(x)}{\partial\theta}\frac{\partial\theta}{\partial x}$, where $x = \cos\theta$, thus $\frac{\partial\theta}{\partial x} = \frac{-1}{\sin\theta}$.

$$\frac{\partial P_l^0(\cos\theta)}{\partial\theta} = \frac{l}{\sin\theta} \left[\cos\theta P_l^0(\cos\theta) - P_{l-1}^0(\cos\theta)\right]. \tag{B.10}$$

In the case of the non-axisymmetric component of the field, $m > 0$, the derivative of the Legendre polynomial may be expressed as

$$\sqrt{1-x^2}P'^m_n(x) = \frac{1}{2}P_n^{m+1}(x) - \frac{1}{2}(n+m)(n-m+1)P_n^{m-1}(x), \tag{B.11}$$

$$\frac{\partial P_n^m(\cos\theta)}{\partial\theta} = \frac{-\sin\theta}{2\sin\theta} \left[P_l^{m+1}(\cos\theta) - (l+m)(l-m+1)P_l^{m-1}(\cos\theta)\right]. \tag{B.12}$$

In order to sum all the axisymmetric terms without calculating polynomial with $l > l_{max}$, we could use the identity

$$P_n^{m+1}(x) = \frac{2mx}{\sqrt{1-x^2}}P_n^m(x) - (n(n+1) - m(m-1))P_n^{m-1}(x), \tag{B.13}$$

thus,

$$P_l^{m+1}(\cos\theta) = 2m\cot\theta P_l^m(\cos\theta) - (l(l+1) - m(m-1))P_l^{m-1}(\cos\theta). \tag{B.14}$$

Using equation B.14 in equation B.12

$$\frac{\partial P_n^m(\cos\theta)}{\partial\theta} = - \left[m\cot\theta P_l^m(\cos\theta) + kP_l^{m-1}(\cos\theta)\right], \tag{B.15}$$

where $k = [-(l+m)(l-m+1) - l(l+1) + m(m-1)]/2$. The vector components then, may be expressed in terms of the spherical harmonic coefficients potential $\alpha$ and $\beta$ as:

$$B_r = \sum_l \sum_m (l+1)\frac{R^{l+1}}{r^{l+2}} P_l^m(\cos\theta) \left[\alpha_l^m e^{im\varphi} + \beta_l^m e^{-im\varphi}\right], \tag{B.16}$$

$$B_\theta = \sum_l \frac{R^{l+1}}{r^{l+2}} \frac{l}{2\sin\theta} \left[ P_{l-1}^0(\cos\theta) - \cos\theta P_l^0(\cos\theta) \right] \alpha_l^0 \tag{B.17}$$

$$+ \sum_m \frac{R^{l+1}}{r^{l+2}} \left[ m\cot\theta P_l^m(\cos\theta) + kP_l^{m-1}(\cos\theta) \right] \left[ \alpha_l^m e^{im\varphi} + \beta_l^m e^{-im\varphi} \right],$$

$$B_\phi = \sum_l \sum_m \frac{R^{l+1}}{r^{l+2}} P_l^m(\cos\theta) im \left[ \alpha_l^m e^{im\varphi} + \beta_l^m e^{-im\varphi} \right]. \tag{B.18}$$

## B.2 The poloidal potential and the electrostatic potential

Glatzmaier (1984) writes the radial component of the magnetic field at the outer boundary in terms of the poloidal potential, $b$ (from equation 4.5).

$$B_r(r,\theta,\phi) = \frac{1}{r^2} \sum_{l=0}^{\infty} \sum_{m=-l}^{m=l} l(l+1) b_l^m P_l^m(\cos\theta) e^{im\varphi}. \tag{B.19}$$

which may also be expressed in terms of $m > 0$ as

$$B_r(r,\theta,\phi) = \frac{1}{r^2} \sum_{l=0}^{\infty} \sum_{m=0}^{m=l} l(l+1) P_l^m(\cos\theta) \left[ b_l^m e^{im\varphi} + (-1)^m \frac{(l-m)!}{(l+m)!} b_l^m e^{-im\varphi} \right]. \tag{B.20}$$

One may define the coefficient on the right hand side as $b'^m_l = (-1)^m \frac{(l-m)!}{(l+m)!} b_l^m$.

Since the radial component of the magnetic field is continuous at $r = r_o$, $B_r|_{r_o^+} = B_r|_{r_o^-}$. This is equivalent to

$$\frac{1}{r_o^2} \sum_{l=0}^{\infty} \sum_{m'=-l}^{l} l(l+1) b_l^{m'} P_l^{m'}(\cos\theta) e^{im'\varphi} = \sum_{l=0}^{\infty} \sum_{m=0}^{l} (l+1) \frac{R^{l+1}}{r_o^{l+2}} P_l^m(\cos\theta) \left[ \alpha_l^m e^{im\varphi} + \beta_l^m e^{-im\varphi} \right], \tag{B.21}$$

So, for $R = r_o$, we can write the matching coefficients for $m \geq 0$,

$$\frac{1}{r_o^2} l(l+1) \left[ b_l^m e^{im\varphi} + b'^m_l e^{im\varphi} \right] = \frac{l+1}{r_o} \left[ \alpha_l^m e^{im\varphi} + \beta_l^m e^{-im\varphi} \right], \tag{B.22}$$

which can be true for all $m$ only if

$$\alpha_l^m = \frac{l}{r_o} b_l^m, \qquad (B.23) \qquad\qquad \beta_l^m = \frac{l}{r_o} b'^m_l. \qquad (B.24)$$

Thus, the poloidal potential, $b(r,\theta,\varphi)$, at the outer boundary, $r_o$, gives us an expression for the coefficients $\alpha$ and $\beta$ of the potential $\phi(r,\theta,\varphi)$.

# B.3  Numerical implementation

We have found an expression for the the potential $\phi$ and we can now calculate the field far from the dynamo region using equations B.16, B.17, and B.18. It is important to note that the fields have been expressed in terms of the non-normalized Legendre polynomial, and that in order to use the normalized polynomial one has to take care of terms with degree other than $l$ or order other than $m$. Since the sum in equation B.17 was found from $\frac{\partial P_l^m}{\partial \theta}$ when normalizing the polynomial $\wp_l^m = c_l^m P_l^m$, where

$$
c_l^m = \begin{cases} (-1)^m \sqrt{\frac{2l+1}{4\pi} \frac{(l-m)!}{(l+m)!}} & , \text{ Full normalization} \\ (-1)^m \sqrt{\frac{1}{\pi} \frac{(l-m)!}{(l+m)!}} & , \text{ Schmitt normalization} \end{cases}
\tag{B.25}
$$

The natural normalization of $\wp_l^{m-1}$ and $\wp_{l-1}^0$ will not be useful to express $\frac{\partial P_l^m}{\partial \theta}$, where $c_l^m$ is expected. For the axisymmetric terms then

$$
c_l^0 P_{l-1}^0 = \wp_{l-1}^0 \frac{c_l^m}{c_{l-1}^0} = \begin{cases} \wp_{l-1}^0 \sqrt{\frac{2l+1}{4\pi}} \sqrt{\frac{4\pi}{2l-1}} = \wp_{l-1}^0 \sqrt{\frac{2l+1}{2l-1}} & , \text{ Full} \\ \wp_{l-1}^0 \sqrt{\frac{1}{\pi}} \sqrt{\pi} = \wp_{l-1}^0 & , \text{ Schmitt} \end{cases}
\tag{B.26}
$$

For the non-axisymmetric part the multiplying factor is independent of the normalization used,

$$
\begin{aligned}
c_l^m P_l^{m-1} &= \wp_l^{m-1} \frac{c_l^m}{c_l^{m-1}} = \wp_{l-1}^0 (-1)^m \sqrt{\frac{(l-m)!}{(l+m)!}} (-1)^{m-1} \sqrt{\frac{(l+(m-1))!}{(l-(m-1))!}} \\
&= \frac{-\wp_l^{m-1}}{\sqrt{(l-m+1)(l+m)}}.
\end{aligned}
$$

Using the normalized coefficients we can express completely the three components in terms of the coefficients from the poloidal scalar potential for $r = r_o$. Rewriting equations B.16, B.17, and B.18,

$$
B_r = \sum_{l=0}^{l_{max}} \sum_{m=0}^{l} l(l+1) \frac{R^l}{r^{l+2}} \wp_l^m(\cos\theta) \left[ b_l^m e^{im\varphi} + b_l'^m e^{-im\varphi} \right],
\tag{B.27}
$$

$$
\begin{aligned}
B_\theta = \sum_{l=0}^{l_{max}} \Bigg\{ & \frac{R^l}{r^{l+2}} \frac{l^2}{2\sin\theta} \left[ k_1 \wp_{l-1}^0(\cos\theta) - \cos\theta \wp_l^0(\cos\theta) \right] b_l^0 \\
& + \sum_{m=1}^{l} l \frac{R^l}{r^{l+2}} \left[ m\cot\theta \wp_l^m(\cos\theta) + k_2 \wp_l^{m-1}(\cos\theta) \right] \left[ b_l^m e^{im\varphi} + b_l'^m e^{-im\varphi} \right] \Bigg\},
\end{aligned}
\tag{B.28}
$$

$$
B_\phi = \sum_{l=0}^{l_{max}} \sum_{m=0}^{l} \frac{R^l}{r^{l+2}} \wp_l^m(\cos\theta) iml \left[ b_l^m e^{im\varphi} + b_l'^m e^{-im\varphi} \right].
\tag{B.29}
$$

where $k_1 = \sqrt{\frac{2l+1}{2l-1}}$ in case of the Schmidt normalization or $k_1 = 1$ otherwise. $k_2 = \frac{(l+m)(l-m+1)+l(l+1)-m(m-1)}{2\sqrt{(1-l+1)(l+m)}}$ for both Schmidt and full normalization, $k_2 = k$ for non-normalized Legendre polynomial.

# Appendix C

# Symbols

Table C.1: In this table the symbols used throughout the document are listed. We include the meaning of the symbol, the units of the quantity they represent and the first page where the symbol was used in the document (in this page the reader may also find a description of the quantity). We used polar spherical coordinate system, $\{r, \theta, \varphi\}$, unless otherwise specified, and we denote the vector component with the direction as a subscript. We define the axis of rotation by $\hat{z}$ where $z = r \cos \theta$.

| Symbol | Meaning | Units | page |
|---|---|---|---|
| $A$ | Alfvén number | | 42 |
| $\alpha$ | Coefficient of thermal expansion | $K^{-1}$ | 4 |
| $\mathbf{B}$ | Magnetic induction vector | T | 7 |
| $b$ | Poloidal magnetic potential | T m$^2$ | 52 |
| $\chi$ | Radius ratio $r_i/r_o$ | | 6 |
| $D$ | $r_o - r_i$ | m | 6 |
| $\mathbf{D}$ | Electric displacement vector | C m$^{-2}$ | 100 |
| $\mathbf{E}$ | Electric field vector | V m$^{-1}$ | 100 |
| $E$ | Ekman number | | 7 |
| $E_t$ | Turbulent Ekman number | | 8 |
| $\varepsilon$ | External heat source | K s$^{-1}$ | 100 |
| $\eta$ | Dynamic viscosity | Pa s | 97 |
| $\mathbf{f}$ | Force per unit volume | N m$^{-3}$ | 96 |
| $\mathbf{f}^b$ | Buoyancy force per unit volume | N m$^{-3}$ | 96 |
| $\mathbf{f}^c$ | Coriolis force per unit volume | N m$^{-3}$ | 96 |
| $\mathbf{f}^m$ | Magnetic force per unit volume | N m$^{-3}$ | 96 |
| $\mathbf{f}^{vis}$ | Viscous force per unit volume | N m$^{-3}$ | 96 |
| $\phi$ | Electric potential | N m | 39 |
| $\phi_g$ | Gravitational potential | N m | 96 |

| Symbol | Meaning | Units | page |
|---|---|---|---|
| $g$ | Acceleration due to gravity | m s$^{-2}$ | 7 |
| $g_0$ | Acceleration due to gravity at the outer boundary | m s$^{-2}$ | 4 |
| **H** | Magnetic field vector | A m$^{-1}$ | 100 |
| **J** | Electrical current | A | 98 |
| **j** | Electrical current density | A m$^{-2}$ | 98 |
| $j$ | Toroidal magnetic potential | T m | 52 |
| $\kappa$ | Thermal diffusivity | m$^2$ s$^{-1}$ | 4 |
| $\kappa_t$ | Turbulent thermal diffusivity | m$^2$ s$^{-1}$ | 4 |
| $k$ | Electron collision frequency | s$^{-1}$ | 101 |
| $\lambda$ | Magnetic diffusivity | m$^2$ s$^{-1}$ | 4 |
| $l$ | Latitudinal degree | | 39 |
| $\Lambda$ | Elsasser number | | 25 |
| $m$ | Azimuthal wave number ($\exp(im\varphi)$) | | 39 |
| $m_e$ | Mass of the electron | Kg | 101 |
| $\mu$ | magnetic permeability | H m$^{-1}$ | 6 |
| $\mu_b$ | Bulk viscosity | Pa s | 97 |
| $\nu$ | Kinematic viscosity | m$^2$ s$^{-1}$ | 4 |
| $\nu_t$ | Turbulent kinematic viscosity | m$^2$ s$^{-1}$ | 4 |
| $\omega$ | Vorticity | s$^{-1}$ | 22 |
| $\Omega$ | Rotation rate of the mantle | s$^{-1}$ | 4 |
| $p$ | Pressure | Pa | 96 |
| $P$ | Fluctuating modified pressure | Pa | 7 |
| $P_l^m(x)$ | Legendre polynomial degree $l$ and order $m$ | | 39 |
| $\wp_l^m(x)$ | Normalized Legendre polynomial degree $l$ and order $m$ | | 107 |
| $P_m$ | Magnetic Prandtl number $\nu/\lambda$ | | 7 |
| $P_r$ | Prandtl number $\nu/\kappa$ | | 7 |
| $\partial_i$ | Partial covariant derivative $\frac{\partial}{\partial x_i}$ | $[i]^{-1}$ | 96 |
| $\pi_{ij}$ | $ij$ component of the stress tensor | Pa | 97 |
| $q_e$ | Electrical charge of the electron | C | 101 |
| $r_i$ | Radius of the internal boundary | m | 4 |
| $r_o$ | Radius of the external boundary | m | 4 |
| $R_a$ | Rayleigh number $g\alpha\Delta T D^3/\kappa\nu$ | | 7 |
| $R_{a_c}$ | Critical Rayleigh number for convection | | 12 |
| $R_{a_d}$ | Lowest Rayleigh number for dynamo action | | 12 |
| $R_a^{pl}$ | Planetary Rayleigh number $R_a/(1-\chi)^3$ | | 21 |
| $R_e$ | Reynolds number $uD/\nu$ | | 37 |
| $R_{earth}$ | Mean Earth's radius $6.3728 \times 10^6$ | m | 2 |
| $R_m$ | Magnetic Reynolds number $uD/\lambda$ | | 43 |
| $R_o$ | Rossby number $u/\Omega D$ | | 37 |
| $\rho$ | Mass ensity | Kg m$^{-3}$ | 4 |

| Symbol | Meaning | Units | page |
|---|---|---|---|
| $\rho_e$ | Charge density | $C\ m^{-3}$ | 100 |
| $\sigma$ | Electrical conductivity | $S\ m^{-1}$ | 56 |
| $t$ | Time | s | 7 |
| $T$ | Temperature | K | 7 |
| $T_{ref}$ | Reference temperature | K | 97 |
| $\Delta T$ | Temperature difference across the shell | K | 4 |
| $\tau_\lambda$ | Magnetic diffusion time | s | 7 |
| $\tau_\nu$ | Viscous diffusion time | s | 6 |
| $\mathbf{u}$ | Velocity vector | $m\ s^{-1}$ | 7 |